# Magnetic field effects on water and aqueous solutions

Dissertation submitted to the University of Dublin

for the degree of Doctor of Philosophy

By

**SRUTHY POULOSE**

**April 2022**

**SCHOOL OF PHYSICS**

**TRINITY COLLEGE DUBLIN**

**DUBLIN 2**

# Declaration

I hereby declare that this thesis is original and has not been submitted in whole or in part for consideration for any other degree or qualification in this, or any other University.

This thesis is the result of my own work and includes nothing which is the outcome of work done in collaboration, except where specifically indicated in the text.

I agree to deposit this thesis in the University's open access institutional repository or allow the library to do so on my behalf, subject to Irish Copyright Legislation and Trinity College Library conditions of use and acknowledgement.

Sruthy Poulose

April 2022

*Dedicated to my family*

# Acknowledgement

Firstly, I would like to acknowledge my supervisor Prof. Michael Coey for giving an opportunity to work with him. It is a great privilege to work with one of the leading scientists in the magnetism community and words cannot describe how he helped me in developing my scientific knowledge and skills. I would like to thank Dr. M. Venkatesan for his great support and help in my experiments. Words are not enough for his mental support and motivation during my PhD.

I would like to thank MAMI, the Marie Curie Horizon 2020 ITN network EU for funding my PhD; my PhD would not have been possible without that. It was an honour to be a part of a Marie Curie network and I had great experiences working with many other scientists. The MAMI network meetings gave me many wonderful opportunities to talk, interact and discuss with many scientists. I am extremely thankful to this funding which helped me in multitude of ways. I thank Prof. Fernando, Prof. Lourdes and Dr. Yara Alavres for their help and support during my secondment in Spain. I am thankful to my fellow PhD students in MAMI network for their help and support. Special thanks to Prof. Laurence Noirez for her support and inspiration for my research. I would like to express my sincere gratitude to Dr. Peter Dunne for helping my research with his scientific knowledge and expertise. I am grateful to him for believing in me and my scientific quest, which helped me stay encouraged and motivated. Besides the EU support, I am thankful to HEA College fund for granting me a five month extension related to the COVID pandemic that allowed me to finish my work.

I would like to thank the past and present members of the Magnetism and Spintronics group in Trinity College Dublin for all of their help and support throughout my PhD. They have transferred many valuable skills and knowledge to me and were always ready to offer help and advice when I needed it and working with them has been a privilege. Special thanks to Prof. P. Stamenov for his help in analysing the data and sharing his scientific knowledge.

My colleague and friend Dr. Anup Kumar, I do thank him for sharing his knowledge and life experiences with me. The coffee time with him and Venky has been a good memory. I thank

my colleague Ms Rui Zhang for being a good friend and supporter throughout my PhD. Our small talks in the labs were so stress-relieving and helpful. I am very grateful to Ms. Eavan Fitzgerald, a final year project student who worked with me in 2020 on the nanobubbles produced by sonication, work reported in chapter 5 of this thesis. Much of the experimental data there, she collected with my advice and supervision.

I am extremely thankful to my close friends, Ms. Josna Celi, Mr. Praveen MP, Ms. Chicku Mohan, Mr. Abhin Jose, Ms. Cinit Johny, Mr. Joju Thomas, Ms. Alka Thankachan for believing in me and giving me a great support and motivation during my PhD. Their mental support and motivation during my PhD are beyond words.

I'm very grateful to Dr. Aji Alex who has been a brother to me, and always supported me in the PhD process even before it started. I would like to thank my close friends Ms. Nidhi Arora, Mr. Arjun Ravikumar, Mr. Jinu Kurian, Mr. Sachu Raj and Mr. Bijin Ray for their constant support and inspiration throughout my PhD. I am thankful to Ms. Aishwarya Mathew for her help in peer-reviewing my chapters. I thank my best friends, Santhra, Sherin and Sneha for their prayers and love and who were a constant support in my PhD.

I would like to thank my world, my family, Pappa, Amma and my brother Christy. Without them and their mental support this PhD or thesis would not have been possible. They were with me every second of PhD life with abundant love and constant support.

Finally, I want to express my gratitude to Mrs. Wong May Coey for her care and concern during my PhD degree. I would like to thank everyone directly or indirectly related to this thesis for their help. Everyone’s presence in my life has been invaluable and their support helped me to overcome the difficulties I met in my life and study.

# Abstract

Claims of magnetic field effects on water and their potential use in a microfluidic channel are explored. The pendant drop method is used to measure the surface tension, which is calculated from the shape of the drop. The apparent increase or decrease in the surface tension value of diamagnetic water or paramagnetic solutions of magnetic ions is the sum of a small real effect and apparent change due to the magnetic field gradient body force produced by the compact arrays of permanent magnets used to create the field. A zero-susceptibility method has been developed which can distinguish the intrinsic magnetic field effect in water and paramagnetic solutions. Water showed a surface tension change of $0.19 \pm 0.21$ $mNm^{-1}$ in a uniform field. A real surface tension change of paramagnetic $DyCl_3$, $MnSO_4$, $CuSO_4$ solutions are -0.30 $mNm^{1}$, -0.48 $mNm^{-1}$ ,-0.50 $mNm^{-1}$ in a non-uniform vertical field and -0.50 $mNm^{-1}$, -0.51 $mNm^{-1}$, -0.11 $mNm^{-1}$ in the uniform horizontal field. Systematic and controlled evaporation-rate experiments showed an increase of $12 \pm 7$ % for water, and a decrease of $23 \pm 0.2$ % for NaCl and $21 \pm 6$ % for 6 M urea in a 500 mT uniform field. No significant magnetic memory effect was observed. A new model explains the enhanced evaporation rate of water based on the modification of the ortho: para isomeric ratio when a magnetic field is present. The evaporation of water in a microfluidic channel yielded an evaporation rate three times higher than in the beakers in a similar magnetic field. The magnetic field enhancement is also bigger, up to a 100%. The magnetic water treatment of hard and soft water resulted in the precipitation of crystalline polymorphs of $CaCO_3$ by heating and evaporation. Circulation of water through a magnetic treatment device modifies nanobubble generation characterized by zeta-potential measurement. Sonication of soft water produced nanobubbles and hard water precipitated as Calcite or Aragonite, depending on temperature. Magnetic water treatment and ultrasound-induced precipitation showed evidence for the existence of colloidal nanoscale pre-nucleation clusters (DOLLOPS). Finally, some initial set experiments were performed to fabricate magneto responsive cilia loaded with magnetite particles. A method of curing the polymer has to be optimized in future experiments.

# Table of Contents


**Chapter 1** ..... 1

**Introduction** ..... 1

**Bibliography** ..... 7

**Chapter 2** ..... 9

**Magnetic field response of liquid droplets** ..... 9

**2.1 Introduction** ..... 9

**2.2 Instrumentation** ..... 11

**2.3 Experimental setup** ..... 15

**2.4 Results and Discussion** ..... 21

**2.5 Conclusions** ..... 39

**Bibliography** ..... 41

**Chapter 3** ..... 42

**Magnetic field effects on evaporation of water and solutions of NaCl and Urea** ..... 42

**3.1 Introduction** ..... 42

**3.2 Experimental methods** ..... 45

**3.3 Characterization Methods** ..... 47

**3.4 Results and Discussion** ..... 53

**3.4.1 Evaporation** ..... 53

**3.4.2 FTIR and Raman spectroscopy** ..... 70

**3.4.3 NMR** ..... 73

**Bibliography** ..... 77

**Chapter 4** ..... 81

**Evaporation of water in a microfluidic channel** ..... 81

**4.1 Introduction** ..... 81

**4.2. Microfluidic systems** ..... 84

**4.2.1 PMMA/PSA/PMMA** ..... 84

**4.2.2 PDMS/Glass** ..... 85

**4.2.3 PMMA/PMMA** ..... 85
**4.3 Experimental methods** ..... 86
**4.4 Results** ..... 89
**4.5 Discussion** ..... 97
**4.6 Conclusion** ..... 99
**Bibliography** ..... 101
**Chapter 5** ..... 102
**Magnetic water treatment*** ..... 102
**5.1 Introduction** ..... 102
**5.2 Ultrasonic water treatment** ..... 104
**5.2.1 Nanobubble production: Acoustic cavitation** ..... 105
**5.2.2 Characterization of nanobubbles; zeta-potential** ..... 108
**5.2.2 Stability of nanobubbles** ..... 109
**5.3 Experimental methods** ..... 111
**5.3.1 Magnetic water treatment** ..... 113
**5.3.2 Ultrasound induced precipitation** ..... 114
**5.4 Characterization methods** ..... 117
**5.4.1 X- ray Diffraction (XRD)** ..... 117
**5.4.2 Scanning Electron Microscopy (SEM)** ..... 119
**5.4.3 Zetasizer** ..... 121
**5.4.3 Conductivity** ..... 122
**5.5 Results and Discussion** ..... 123
**5.5.1 Magnetic water treatment** ..... 123
**5.5.2 Ultrasonic Induced nanobubbles** ..... 132
**5.5.3 Ultrasonic induced precipitation** ..... 134
**5.6 Conclusions** ..... 146
**Bibliography** ..... 148
**Chapter 6** ..... 152
**Conclusion and Future Direction** ..... 152
**6.1 Conclusion** ..... 152
**6.2 Future direction** ..... 155
**6.2.1 Experimental methods** ..... 155
**6.2.1 First Results and Conclusion** ..... 157

**Appendix A** ..... 159
**Appendix B** ..... 162

# List of Figures

Figure 2. 1 Schematic setup of the OCA25 droplet analyer ..... 11
Figure 2. 2: a) Young Laplace fit on a pendant drop b) an example of the captured pendant drop. ... 12
Figure 2. 3:a) Illustration of a DC SQUID, a superconducting loop with two Josephson junctions in parallel. Total current ($I_{tot}$) enters the loop and splits into two paths. A voltage (V) is measured across the loop and Φ is the externally applied magnetic flux (red arrows) b) DC SQUID magnetometry setup ..... 14
Figure 2. 4: Permanent magnet arrays used to apply magnetic fields to the pendant drop. A) Uniform horizontal field, b) Vertical field with a vertical gradient $dB_z/dz$ c) Horizontal field with a vertical gradient $dB_x/dz$. ..... 15
Figure 2. 5: Magnetic field profile of the uniform magnetic field assembly and an image of the assembly. ..... 16
Figure 2. 6: Position of pendant drops at different heights from the surface of the 5-magnet magnetic assembly ..... 17
Figure 2. 7. The 5-magnet array with the values of a) $B_z$ and b) $dB_z/dz$ along the vertical axis. Black dots mark the positions of the centre of the droplet. ..... 17
Figure 2. 8: The 3-magnet array, with the values of a) $B_x$ and b) $dB_z/dz$ along the vertical axis. Black dot marks the position of the centre of the droplet. ..... 18
Figure 2. 9: The experimental steps for surface tension measurements ..... 18
Figure 2. 10: Schematic diagram representing Kelvin $B\nabla B$ force in vertical and horizontal fields and the Maxwell stress $\sigma_M$. Three schematic droplets showing the fields and forces. a) in a vertical field with a vertical gradient, b) in a horizontal field with a vertical gradient and c) in a uniform horizontal field (Maxwell stress) ..... 19
Figure 2. 11: Apparent surface tension changes $\Delta\gamma_{app}$ in a vertical magnetic field gradient a) Water, b) 0.1 M $DyCl_3$ at position 1. ..... 22
Figure 2. 12: Changes of apparent surface tension in a vertical magnetic field gradient a) 0.05 M $DyCl_3$, b) 0.01 M $DyCl_3$ at position 1 ..... 23
Figure 2. 13: Apparent changes in surface tension of a) 0.05 M $DyCl_3$ and b) 1M $DyCl_3$ in a vertical field gradient measured at different positions ..... 24

Figure 2. 14: Images of pendant droplet of a) water b) 0.1M $DyCl_3$ without and with a vertical field gradient magnetic field. Green drop contour is when there is no magnetic field and the dotted red contour shows the shape of the drop when a magnetic field is present. .....25
Figure 2. 15: Apparent surface tension changes in a vertical magnetic field gradient a) Water, b) 0.1 M $DyCl_3$.....26
Figure 2. 16: Apparent changes in surface tension of 1 M $DyCl_3$ in a horizontal field with a vertical field gradient at different positions.....27
Figure 2. 17: Images of pendant droplet of a) water b) 0.1M $DyCl_3$ without and with a horizontal magnetic field with a vertical field gradient. .....27
Figure 2. 18: Plots of $\Delta\rho_{eff}$ (%) calculated from Eq 5 versus measured change in apparent surface tension ($\Delta\gamma_{app}$ ) for water and b) plot of gravitational force versus field gradient force of water. .....29
Figure 2. 19: Figure a) and c) are plots of $\Delta\rho_{eff}$ (%) calculated from Eq 5 versus measured change in apparent surface tension ($\Delta\gamma_{app}$ (%)) for 1M $MnSO_4$ and 0.1 M and 1M $DyCl_3$ respectively and b), d) are plot of gravitational force versus field gradient force of 1M $MnSO_4$ and 0.1 and 1M $DyCl_3$. Black line connects the datapoints and the red line is the fit with a fixed slope of 1.....31
Figure 2. 20: a) SQUID measurements of the zero moment $CuSO_4$, $MnSO_4$ and $DyCl_3$ solutions. Zero susceptibility optimisation of different concentrations of b) $CuSO_4$, c) $MnSO_4$, d) $DyCl_3$. The blue dot in the figures marks the zero-susceptibility concentration in each case. .....33
Figure 2. 21: a) Zero susceptibility optimisation of different concentrations of $CuSO_4$, using SQUID data b) Variation of apparent surface tension as a function of the concentration of copper solutions..34
Figure 2. 22: An example of the fitting process for a 0.1 M $DyCl_3$ solution, using the vertical gradient 5-magnet array. (a) a representation of the border of the drop`s projection (b) the fitted data and fitting curve in polar coordinates (c) residual plot of the fit in polar coordinates.....37
Figure 2. 23: Prolate deformation of a spherical drop with a positive susceptibility due to Maxwell stress $\sigma_M$ due to the distribution of positive and negative magnetic charge induced by the magnetic field.....38

Figure 3. 1: Experimental evaporation setup. The water sample and the control are mounted on two identical balances in a Perspex box, and a 0.5 T magnetic field is applied to the sample using the Halbach ring magnet (blue) .....46
Figure 3. 2: The field profile inside the bore of the Halbach ring magnet a) across a central diameter and b) along the magnet axis .....46
Figure 3. 3: Schematic of FTIR spectroscopy instrumentation.....49

Figure 3. 4: a) Schematics of Raman spectroscopy instrumentation, b) Stokes and anti-stokes sidebands ..... 50
Figure 3. 5: (a) The two spin states $\alpha$ and $\beta$, of a nucleus with I = 1. (b) The energy levels of a nucleus with I = 1. (c) The total nuclear magnetization at thermal equilibrium ($M_0$) in a magnetic field $B_0$ ..... 51
Figure 3. 6: (a) The action of a magnetic field $B_1$ on the total nuclear magnetization $M_0$ and the precession around $B_0$. ($\theta$ is the flip angle and $\nu_0$ is the precessional frequency. (b) The time-based free induction decay (FID) resulting from detection of the precessing transverse component of the nuclear magnetization after a pulse, and its Fourier transform to give the frequency sweep spectrum ..... 52
Figure 3. 7: Instrumentation of *NMR* spectrometer ..... 53
Figure 3. 8: Relative weight loss by evaporation of water in a 500 mT magnetic field parallel to the surface (red lines) and a reference with no magnetic field (black lines). The initial masses are 10 g (a), 20 g (b) and 50 g (c). The fourth panel plots the weight the weight loss as a function of inverse sample mass showing the effect scales with surface area, and the weight loss is 8 % faster in the magnetic field. ..... 54
Figure 3. 9 : Relative weight loss by evaporation in runs where only minor fluctuations of temperature and humidity over 16 h a) 30 mL water, c) 50 mL 1M NaCl and e) 50 mL 6 M Urea. Black lines are for reference samples, red lines for samples exposed to a 500 mT magnetic field. Panels b), d) and f) shows the corresponding temperature and relative humidity during the runs. ..... 56
Figure 3. 10: Extended 60 h run of evaporation versus time for a 50 mL water sample in 500 mT(red) and the no-field reference (black). a) relative weight loss by evaporation b) evaporation rates versus time and c) histograms of the evaporation rates (reduced mass loss per hour), where the average values are marked ..... 57
Figure 3. 11: Difference of change of temperature in the course of 16 h runs between in-field and zero field water. The average over 6 runs in only 0.1 ℃. ..... 58

Figure 4. 1: Schematic diagram of a microfluidic channel. The $CO_2$ laser cut middle channel show small reference 86
Figure 4. 2: a) Experimental setup for evaporation experiment where temperature and humidity are controlled. b) schematic of the dimension of a microfluidic channel with a water drop at the centre 87
Figure 4. 3: a) Schematic diagram of a microfluidic channel in-plane magnetic field (water meniscus shown as blue) b) Magnetic field profile of the rectangular magnet. 88

Figure 4. 4: a) The experimental setup of water meniscus in a magnetic field where the field is parallel to the meniscus b) magnetic field profile of the magnet setup and the microfluidic channel is placed at the middle where the water drop in the channel is in a 220 mT field 88
Figure 4. 5: Schematic of a microfluidic channel and water meniscus 89
Figure 4. 6: Example A. Real-time evaporation of water samples in a microfluidic channel. Shrinking of the volume leads to a membrane across the channel, which breaks 30 seconds later. Note that the contact angle with the walls seen in the menisci is about 30°, but the contact angle with the flat upper and lower surfaces of the channel is close to 90°. In this experiment the initial volume was 0.12μL 90
Figure 4. 7: More examples of real-time evaporation of water samples in a microfluidic channel. Shrinking the volume leads to a membrane across the channel, which ruptures 5 hours, 3 hour 30 minutes and 1 hour 55 minutes later for examples B, C, D respectively. Note that recondensed water droplets accumulate on the flat PMMA surfaces on both sides of the drop in experiments 1 and 2. 91
Figure 4. 8: a), b) shows normalised plots of $L$ and $l$ versus time in experiment 1 and c), d) in experiment 2 (red is for meniscus in a $B_z$ magnetic field and black is for control water) 92
Figure 4. 9: Plot of reduced volume versus time for a 300 mT $B_z$ magnetic field and control water. The rate of evaporation is 49% greater in the field. 94
Figure 4. 10: Plots of two examples of reduced volume versus time with and without a 220 mT $B_y$ magnetic field . The evaporation in the field in 28% faster in a) and 23% faster in b) 94
Figure 4. 11: a) shows the evaporation of water in the same microfluidic channel for repeated experiments. There is small reduction in the evaporation when many experiments are repeated in the same channel 95
Figure 4. 12: (a) Plot of normalized volume of repeated experiments on the same day (same microfluidic channel) (b) Evaporation experiments of control water (in black) and water exposed to the magnetic field (in red) on different days. 96
Figure 4. 13: Pictorial representation of the temperature gradient due to non-uniform evaporation across the meniscus. There is a corresponding surface tension gradient, and the internal flow of liquid due to the evaporation-induced surface tension gradient. Black arrows show the flow of water from the centre of the meniscus towards the edge. 98

Figure 5. 1: Principle of ultrasound cavitation. The initiated bubbles grow due to evaporation and finally reach critical size (resonant) when it grows quickly and collapse violently[38].....106
Figure 5. 2: Schematic representation of Laplace pressure inside a nanobubble[39] .....107

Figure 5. 3: Diagram of the electric potential and ion distribution as a function of distance from the surface of a charged body in dispersion, with the slipping plane, clearly marked [45]..... 109
Figure 5. 4: Magnetic water treatment setup ..... 113
Figure 5. 5: Magnetic field calibration along the cross-section of the Ecocamel magnetic water conditioner..... 114
Figure 5. 6: a) Ultrasonic probe in sample solution; Experimental setup for the nanobubble production, b) Solution immersed in water bath c) without a water bath..... 115
Figure 5. 7: Schematic diagram of Bragg diffraction Law. X-ray radiation incident at an angle θ is reflected from parallel atomic planes with spacing d. ..... 118
Figure 5. 8: Basic XRD measurement geometry: X-ray source, detector, and the sample stage. ..... 118
Figure 5. 9: SEM instrumentation ..... 120
Figure 5. 10: XRD images of evian water a), b) control and treated water after 1 passes and c), d) control and treated water after 10 passes..... 124
Figure 5. 11: XRD images of Hillbrook water a), b) control and treated water after 10 passes and c), d) control and treated water after 10 passes ..... 125
Figure 5. 12: XRD images of tap water a), b) control and treated water after 10 passes and c), d) control and treated water after 10 passes..... 126
Figure 5. 13: XRD images of volvic water a) control b) treated water, after 1 pass ..... 127
Figure 5. 14: SEM images of precipitates of Evian and tapwater after 10 passes. a) Evian control water b) Evian through magnetic treatment device (scale bar of 20 μm), c) tap control soft water d) tap through the magnetic treatment device (scale bar of 20 μm). The needle-shaped crystallites are Aragonite and the equiaxed crystallites are calcite. ..... 128
Figure 5. 15: Zeta potential after 1, 10, 25 and 50 passes of a) Evian b) Hillbrook well water, c) Tap water, d) Volvic. Zero (black) is the value of the zeta potential before passing waters through the peristaltic pump ..... 129
Figure 5. 16: Conductivity after1, 10, 25 and 50 passes of a) Evian b) Hilbrook well water, c) Tap water, d) Volvic. Zero (black) is the value of the zeta potential before passing waters through the peristaltic pump ..... 130
Figure 5. 17: Mass of the precipitate after 1, 10, 25 and 50 passes of a) Hillbrook well water b) Tap water, c) Volvic. Zero (black) is the value of the zeta potential before passing waters through the peristaltic pump ..... 131
Figure 5. 18:a) zeta potential of nanobubbles with time, b) Temperature of the nanobubbles during the sonication and cooling process and it's corresponding zeta potential ..... 133

Figure 5. 19: The a) zeta potential and b) PH of various water before and after sonication. Orange line in a) shows the trend of zetapotential with hardness.....134
Figure 5. 20: Conductivity of various water samples in the order of increasing hardness .....135
Figure 5. 21: Conductivity and zetapotential dependence of Evian and Ballygowan on sonication time. .....137
Figure 5. 22: Interfacial tension of various waters before and after sonication.....138
Figure 5. 23: conductivity and zeta potential of primary samples of Evian, Ballygowen and their supernatant solutions.....139
Figure 5. 24: XRD patterns of precipitate samples collected from Evian. Characteristic Calcite 104 peak at 29°and Aragonite 221 at 46°labelled. Halite 002 peak is at 32°. Significant peaks denote Calcite, Aragonite and Halite as C, A, H, respectively.....142
Figure 5. 25: XRD patterns of precipitate samples collected from Ballygowan. Characteristic Calcite 104 peak at 29°and Aragonite 221 at 46°labelled. Halite 002 peak is at 32°. Significant peaks denote Calcite, Aragonite and Halite as C, A, H, respectively.....143
Figure 5. 26: SEM images of precipitate extracted from Evian after sonication. The needle-shaped crystallites in the figure show the presence of aragonite. The figure on the right panel is zoomed image with the scale bar 1μm .....144
Figure 5. 27: SEM images of precipitate extracted from Ballygowan after sonication. The needle-shaped crystallites are aragonite. .....145

Figure 6. 1: a) images of 2D printed micropillars b) Image of the fabricated magnetite loaded pillars

# List of papers submitted or in preparation

1. **S.Poulose**, J. Quirke, P.Stamenov, M. Mobius and J.M.D. Coey ‘ Deformation and necking of liquid droplets in magnetic field’ ( *submitted to Physics of fluids)*)
2. **S.Poulose**, M. Venkatesan, M.Mobius and J.M.D. Coey ‘Evaporation of water and urea in a magnetic field; role of nuclear isomers ’ (*submitted, Journal of colloids and interfaces*)
3. E. Fitsgerald, **S.Poulose** and J.M.D. Coey ‘ Interaction and stability of nanobubbles and prenucleation clusters during ultrasonic treatment of hard and soft water (*submitted, Lamgmuir*)
4. **S.Poulose**, Y.Alavres, L. Besabe, F.Benito and . J.M.D. Coey ‘Magnetic field effects on evaporation of water in a microfluidic channel’ (*in preparation*)
5. **S.Poulose**, M. Power, M. Venkatesa and J.M.D. Coey ‘ Polarity of metal oxide surfaces and wettability’ (*in preparation*)

# Chapter 1

# Introduction

Wettability and surface tension are unavoidable properties of liquids that we observe in nature. It could be the rolling of water droplets on lotus leaves and butterfly wings, spiders walking on water etc. These naturally occurring phenomena can be bio-mimicked to find solutions to daily-life problems since nature sets an example for us to follow. The rolling of water droplets on lotus structures is due to the rough microstructures on its surface that which results in a non-wetting surface [1]. Water falling on these structures rolls off in one particular direction depending on the direction of alignment of structures. The alignment of microstructures plays a big role in the directed transport of droplets.

Directed liquid transport of liquid droplets has a lot of applications such as liquid propulsion, droplet microfluidics, drop rebound and liquid flow [2]. The flow rate of liquid in a microfluidic channel is one important parameter when considering sensing applications such as lab on a chip [3]. Especially in sensing applications, a super hydrophobic channel wall is highly desirable to avoid biofouling [4]. Engineering a smart microfluidic channel for droplet or liquid flow could have potential applications in microfluidics [5]. For sensing applications in microfluidics, minimal usage of chemicals on the channel walls is a prerequisite. Using a remote magnetic field to transport liquid without bio-fouling would have a huge impact on increasing its efficiency.

Microfluidics is a branch of science that studies the behaviour of fluids in micro-channels, and the technology of manufacturing microminiaturized (μm-scale) devices containing chambers and tunnels through which fluids flow are confined. The first applications of microfluidic technologies have been in chemical and biological analysis, for

which they offer a number of useful capabilities including the ability to use very small quantities of samples and reagents, and to carry out separations and detections with high resolution and sensitivity; low cost; short times for analysis and small footprints for the analytical devices.

Microfluidics exploits both its most obvious characteristic ‘small size’ and less obvious characteristics of fluids in microchannels, such as laminar flow. It fundamentally offers new capabilities in the control of concentrations of molecules in space and time. It is crucial to make liquid transport more efficient by modifying the walls of the channel to make them superhydrophobic. The liquid transport in a microfluidic channel requires an external pump. Fabrication of an intelligent super hydrophobic channel that can self-direct liquid droplets in a microfluidic channel is an interesting research area.

The flow rate of water through carbon nanotubes (hydrophobic) is exceptionally high compared to boron nitride nanotubes (hydrophilic) even though their crystallographic properties are strikingly different. A consequence is the remarkable ability of water to flow with little pressure gradient through individual carbon nanotubes, in contradiction to the no-slip boundary condition that applies for structurally-similar boron nitride [6]. This shows the possibility of a potential connection between hydrodynamic flow and the electronic structure of the confining material.

The origin of this distinct contrast between the two systems could be from their atomic-scale differences at the solid-liquid interface. Termination bond, surface charge, and roughness have an influence on surface tension and wettability. This opens up a new avenue for research that could bridge the gap between hydrodynamics and hard, soft condensed matter physics where fluid mechanics meets the atomic nature of matter.

Inspired by natural examples, great efforts have been devoted to developing bioinspired smart materials for directional liquid transport. The key to driving droplets directionally is exerting unbalanced forces at opposite sides. Ideally, such gradients can also be created in

situ by external stimuli, such as light, temperature, mechanical vibration,[7] and magnetic field [8,9], which work individually or collaboratively to transport liquid droplets.

Furthermore, bioinspired micro ratchet-like surfaces with directional liquid transport properties provide an alternative solution to make microfluidic devices more energy-efficient [10]. The current work opened a pathway for designing two-dimensional surfaces for directional liquid transport in energy-favourable microfluidic devices. Non-destructive controlled motion of drops and liquids has promising applications in microfluidics, microreactors, biochemical assays, etc [11]. The control over the motion could be actuated by external stimuli, such as light [12], surface acoustic waves [13], electrical and magnetic fields [14].

Magnetic actuators are interest of in this study due to their powerful ability to control drop/liquid motion without direct external contact. The pioneer work in this field was based on the incorporation of magnetic particles into liquids so as to have strong control over its motion. Another powerful application of magnetic field in microfluidics is the magnetic cell separation which has considerable applications in sensing [15]. A surface wettability gradient could directionally transport liquid or control the motion of drop along the gradient direction [16].

The application of magnetic field offers additional advantages such as non-contact, real-time control, environment friendliness, zero chemical usage and fast response. There are three kinds of magneto-responsive structures - surfaces with bendable magneto-responsive microstructures (cilia), nanostructured magnetic surfaces with switchable topography and ferrofluid-infused surfaces. Fabrication of magnetic particle-infused microstructures undergoes bending deformation under the application of an external magnetic field [17]. The motion and roll-off angle depend on the bending direction of the micropillars [18]. Structures such as micro-needles with a perfluorinated coating are great for the rebound behaviour of the drop since the tilt angle could easily be controlled by an external magnetic field [14,19].

This PhD thesis is a part of Marie Curie Magnetics and Microhydrodynamics (MAMI) HORIZON 2020 ITN network funded by European Union. This multidisciplinary network entitled: “Magnetics and Microhydrodynamics - from guided transport to delivery” bridges the research fields of fluidics and magnetism, by taking advantage of magnetic forces to control local flows and cargo transport inspired by biomimetic systems. Using magnetic sources, as well as high magnetic susceptibility liquids or nanostructures, devices with unique anti-fouling properties and non-slip boundary conditions can be realized. The scientific aim of this project network is to take advantage of such unique wall-less properties to create new applications of microfluidic technology for life sciences. All early-stage researchers work towards a scientific problems to find novel solutions to the existing challenges in microfluidic flow and combine the results to make a full structured solution at the end of the project.

The ultimate aim of this thesis work was to engineer a smart microfluidic channel with walls that can self-direct the liquid flow with the aid of a non-contact magnetic field. The switchable topology of the channel walls should be the result of microstructures on the channel walls that responds to the direction of an applied magnetic field. Before we tackle the actual fabrication of microfluidic channel walls, the first part of the work was to establish whether or not there is any measurable influence of magnetic field on the properties of water itself. The sample volumes under consideration are nanoliters to microliters which points to the importance of understanding how an external field could manipulate the properties of the liquids.

This thesis will systematically investigate the potential use of magnetic field effects with the magnetic field as a control parameter in fluid flow, especially effects in water. The study of magnetic field effects on water is a controversial topic and it is necessary to carry out a careful investigation about claims of magnetic field effects on water.

The first part of this report (Chapter 2) describes work aimed at understanding how an external magnetic field changes the surface tension of water and other liquids. A commercial

tensiometer has used to monitor the surface tension changes. We have used a pendant drop method, which is an optical method to measure the surface tension of liquids based on the shape. The value of surface tension of liquids of different susceptibilities have measured in a uniform magnetic field and field gradient. A new method, zero-susceptibility method used in this study to understand the real magnetic field effects on the surface tension of the liquids when the magnetic body force is zero.

In chapter 3 discuss the magnetic field affects the evaporation rate of water. Magnetic field effects on water are controversial, and many of its claims are still under debate. This chapter discusses a detailed study of magnetic field influence on evaporation of water and aqueous solutions. A custom-made automated setup has been used to monitor the weight changes of water in real-time. We have used water and high concentrated urea and NaCl to understand how magnetic field affects evaporation of concentrated solutions.

Chapter 4 covers work on how the magnetic field affects the evaporation rate of water in a microfluidic channel. This study involves the evaporation of a water meniscus in a microfluidic channel with and without a magnetic field. A careful selection of microfluidic channel materials is an important step in the evaporation experiments. Custom-made magnet assemblies have been used to apply a magnetic field in different directions. The evaporation of water meniscus in a magnetic field were compared with a control water.

Chapter 5 discusses the effect of magnetic water treatment on the precipitation of dissolved $CaCO_3$ and the theory of the magnetic field effect on the de-scaling of pipes. Mineral waters of different hardness are passed through a commercial magnetic water conditioner to explore how a magnetic field influences the preferential precipitation of the polymorphs of $CaCO_3$. The observation of generation of nanobubbles after passing through the magnetic treatment device led to a detailed study, of ultrasound-induced nanobubble generation and precipitation of $CaCO_3$ in deionized, soft and hard water.

Overall conclusions and ideas for future work are presented in Chapter 6. The future work will be the fabrication of smart magneto-responsive structures for directional liquid transport

of liquids. Preliminary research into the fabrication of magneto-responsive structures is reported, using a two-step replica moulding process. To fabricate magneto-responsive pillars, a suitable photosensitive polymer cocktail with suspended magnetic particles was poured over a polydimethylsiloxane (PDMS) replica.

# Bibliography


[1] M. Yamamoto, N. Nishikawa, H. Mayama, Y. Nonomura, S. Yokojima, S. Nakamura, and K. Uchida, Langmuir **31**, 7355 (2015).

[2] B. Hu, Z. Duan, B. Xu, K. Zhang, Z. Tang, C. Lu, M. He, L. Jiang, and H. Liu, Journal of the American Chemical Society **142**, 6111 (2020).

[3] M. Sadegh Cheri, H. Latifi, J. Sadeghi, M. Salehi Moghaddam, H. Shahraki, and H. Hajghassem, Analyst **139**, 431 (2014).

[4] H. Zhang and M. Chiao, Journal of Medical and Biological Engineering **35**, 143 (2015).

[5] D. K. N. Sinz and A. A. Darhuber, Lab on a Chip **12**, 705 (2012).

[6] E. Secchi, S. Marbach, A. Niguès, D. Stein, A. Siria, and L. Bocquet, Nature **537**, 210 (2016).

[7] W. Lei, Z.-H. Jia, J.-C. He, T.-M. Cai, and G. Wang, Applied Physics Letters **104**, 181601 (2014).

[8] D. Tian, N. Zhang, X. Zheng, G. Hou, Y. Tian, Y. Du, L. Jiang, and S. X. Dou, ACS Nano **10**, 6220 (2016).

[9] X.-H. He *et al.*, ACS Applied Materials & Interfaces **7**, 17471 (2015).

[10] Z. Han, Z. Mu, B. Li, Z. Wang, J. Zhang, S. Niu, and L. Ren, ACS Nano **10**, 8591 (2016).

[11] Y. Zhou, S. Huang, and X. Tian, Advanced Functional Materials **30**, 1906507 (2020).

[12] X. Tang and L. Wang, ACS Nano **12**, 8994 (2018).

[13] Z. Wang and J. Zhe, Lab on a Chip **11**, 1280 (2011).

[14] L. Wang, C. Gao, Y. Hou, Y. Zheng, and L. Jiang, Journal of Materials Chemistry A **4**, 18289 (2016).

[15] B. A. Sutermaster and E. M. Darling, Scientific Reports **9**, 227 (2019).

[16] C. Liu, J. Sun, J. Li, C. Xiang, L. Che, Z. Wang, and X. Zhou, Scientific Reports **7**, 7552 (2017).

[17] Y. Lin, Z. Hu, M. Zhang, T. Xu, S. Feng, L. Jiang, and Y. Zheng, Advanced Functional Materials **28**, 1800163 (2018).

[18] D.-M. Drotlef, P. Blümler, P. Papadopoulos, and A. del Campo, ACS Applied Materials & Interfaces **6**, 8702 (2014).

[19] K.-H. Chu, R. Xiao, and E. N. Wang, Nature Materials **9**, 413 (2010).

# Chapter 2

# Magnetic field response of liquid droplets

## 2.1 Introduction

The surface tension of liquids plays a crucial role in wetting and interfacial phenomena. Surface tension or surface energy are key properties of liquids. Microscale and nanoscale device applications such as fluidic micro-robotics and precision micro-manipulators all depend on the surface or interfacial tension of fluids [1]. The basic functioning of the human body itself depends on the surface tension of different biological fluids and surfactants in our body. The flow or properties of liquids could be manipulated by external stimuli such as pH [2], light [3], surface tension gradient/wettability gradient [4] or external fields [5,6]. Contactless control of the physical properties of liquids offers great advantages in versatile areas such as microfluidics and open surfaces, where liquid control is important. Here the use of a magnetic field as a stimulus could have many advantages, for example, 1) it is remote and non-destructive 2) substrate modification can be avoided, reducing chemical waste 3) it is independent of solution conditions (pH, ionicity, temperature etc.). Flow in a microfluidic channel is also controlled by adding magnetic particles along with the liquids in applications such as magnetic cell separation. Creating surface tension gradients remotely is vital where flow control is required.

A recent paper by Hauner et al.[7] reported a high value of surface tension of water of ~ 90 $mNm^{-1}$ during pinch off of pendant droplets on a milliseconds time scale. The static surface tension is the thermodynamic property of a liquid that governs its equilibrium shape. Water, however, was thought to exhibit a different, dynamic surface tension during the pinch-off

process as a pendant droplet becomes detached and falls from an orifice. When a new surfactant interface is formed, its initial surface tension will decrease as surfactant molecules are transported to the interface until the equilibrium value is re-established. During the pinch-off of a pure liquid, the dynamic surface tension inferred is the value at an interface that is in the process of forming the fluid filament, which occurs on a millisecond timescale. He explained this as a dynamic effect where the value of surface tension is higher during the process of forming a fluid filament. The existence of any effect of a magnetic field on the surface tension of water is a controversial topic that has been addressed by many researchers over the years. There is no consensus [8,9], [10], [8,11] , and an adequate explanation for any effect is still missing [10,12-14]. Fujimora et al. for example, reported a small increase of 1.32 $mNm^{-1}$ for surface tension of water in a field of 10 T using a surface-wave resonance method[10]. Others reported a decrease in surface tension of Millipore water with a magnetic field exposure using a commercial magnetic conditioner[8] and neodymium ring magnets[11]. One report states that the magnetic field effects depend on the circulation time and the effect increases with field duration[13]. A recent report by Hayakawa et al. using permanent magnets to apply a field [12] of 250 mT found that the surface tension of was unaffected in a uniform magnetic field, due to the absence of body forces inside the drop. Studies conducted by Katsuki et al. on magnetic field effects on pendant drops in pseudo-microgravity conditions using a superconducting magnet with a field of 15 T found that the size and shape of the drop changes due to magnetic forces[15].

In this work, we have systematically investigated the magnetic field effects on surface tension of different liquids. These experiments were principally aimed at understanding if a magnetic field could produce a change in the surface tension of liquids. We have used custom made magnet assemblies to investigate the magnetic field effects on liquids with different magnetic susceptibility. We have explored possible ways of observing magnetic field effects and have implemented a zero-susceptibility method to differentiate real magnetic field effects from force effects on pendant droplets used to measure surface tension.

## 2.2 Instrumentation

### 2.2.1 Optical contact angle meter

Different methods used to measure a liquids' surface tension include the Du Nouy ring, Wilhelmy plate, and pendant drop methods. The latter is an optical method that deduces the surface tension value from the curvature of a liquid drop captured in a photograph. We use a Dataphysics optical contact angle analyser model OCA 25 to measure the surface tension of the liquids throughout this study. One of the advantages of the pendant drop over other methods is that it requires a very small sample volume. The tensiometer has three main parts, a LED light source, a dispensing unit and a camera. The dispensing unit is software-controlled where dispensing volume and rate can be specified. A high-powered stroboscopic LED source with manual and software control illuminates the suspended drop.

The OCA software interface controls different functionalities of the instrument and it assists in collecting, assessing, and evaluating the measured data. It has a 6x parfocal zoom lens (Field of view 1.32 x 0.99 to 8.50 x 6.38 mm; working distance 87.2mm) with an integrated continuous fine focus (± 6 mm), and adjustable observation angle. The Video measuring system has a USB camera with 768 x 576 pixel resolution and can capture up to 123 images/s. A schematic image of the DATAPHYSICS instrument is shown in Fig.2.1

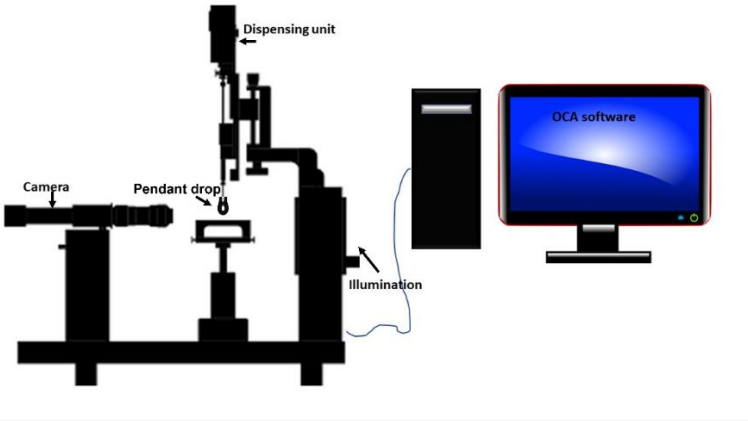


Figure 2. 1 Schematic setup of the OCA25 droplet analyer

The pendant drop method is an optical method to calculate the surface tension of a liquid from the shape of a pendant droplet. The Dataphysics OCA 25 analyser records the shape of a pear-shaped droplet (Fig. 2.2), which depends only on the density of the liquid ρ and its surface tension γ.

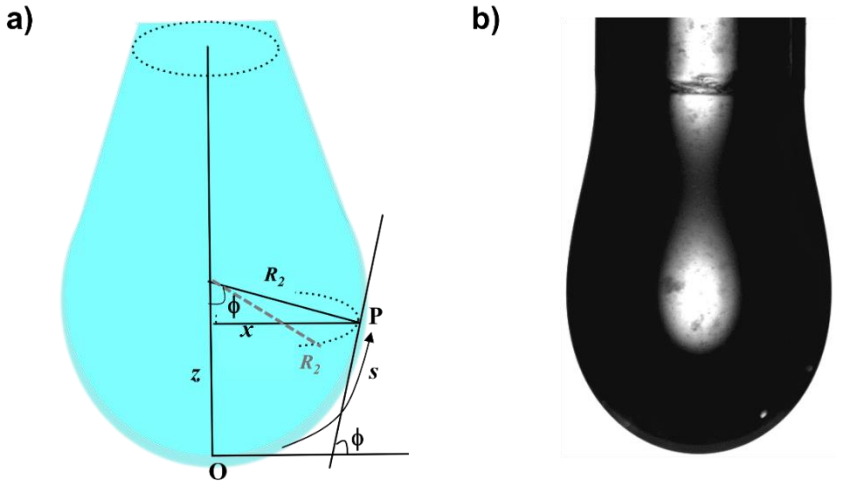


Figure 2. 2: a) Young Laplace fit on a pendant drop b) an example of the captured pendant drop.

The Laplace pressure difference at a point P on the droplet surface with principal radii or curvature $R_1$ and $R_2$ is

$$\Delta P = \gamma(1/R_1 + 1/R_2) \qquad (1)$$

and there is an additional vertical pressure gradient $dP/dz = \rho g$ due to gravity. If the lowest point of the droplet is O, the arc length OP is '$s$' and the tangent to the droplet in a vertical plane containing O and P makes an angle $\phi$ with the horizontal, the surface tension is obtained by

fitting an image of the droplet shape numerically to the three parametric equations (2-4), a procedure carried out automatically by the analyser.

$$\frac{\mathrm{d}\phi}{\mathrm{d}s} = -\frac{sin\ \phi}{x} + \frac{2}{R} \pm \frac{\Delta\rho g z}{\gamma} \quad (2)$$

$$\frac{\mathrm{d}x}{\mathrm{d}s} = cos\ \phi \quad (3)$$

$$\frac{\mathrm{d}z}{\mathrm{d}s} = sin\ \phi \quad (4)$$

The parameter, $\frac{\Delta\rho g z}{\gamma}$ is known as the shape parameter. The negative sign is for the pendant drop and the positive sign is for the sessile dop. In the pendant drop method, surface tension tries to minimise the surface area of a drop and make it spherical, whereas gravity stretches the drop and makes it pear-shaped. For a given ρ, the analyser computes γ from the shape. The DATAPHYSICS tensiometer calculates the value of surface tension from the shape of the captured image of the pendant drop. The software extracts the contour of the pendant drop and fit it the young Laplace equation. We use a nonmagnetic quartz tube with an internal diameter 1.75 mm and an outer diameter 3.02 mm. The lower surface is polished, and the volume of liquid the droplet is approximately 50 μL. Our procedure is to input the density of the liquid to determine the surface tension in zero field $\gamma_0$, and then repeat the measurement in some configuration of magnetic field $\boldsymbol{B}$, noting the difference $\Delta\gamma_{app}$ given by the analyser.

### 2.2.2 SQUID magnetometry

Superconducting Quantum Interference Device (SQUID) magnetometry is a high sensitivity technique employed to measure the absolute moment of a magnetic sample. It is based on a ring of two superconductors separated by two thin weak links called Josephson junctions. The working mechanism of SQUID is quantum tunnelling of superconductor electrons across a Josephson junction, together with flux quantization in a superconducting ring. The weak links

may be made of an insulator or non-superconducting material, as shown in Figure 2.3. In the DC mode, the SQUID can detect moments as low as $10^{-10}$ A $m^{2,}$ and in AC mode the sensitivity increases further with the capability of measuring moments down to $10^{-12}$ A $m^2$.

When a current enters the loop $I_{tot}$, it divides equally into $I_1$ and $I_2$, with equal magnitude and as it passes through each Josephson junction, $I_1$ and $I_2$ undergoes a phase shift when it crosses the Josephson junction. The Josephson zero-voltage supercurrent $I_s = I_c \sin \Delta\theta(t)$ where $I_c$ is the critical current and $\Delta\theta$ (t) is the Josephson phase difference across the junction. The phase difference appears in the presence of a magnetic field; in the absence of a magnetic field, it is zero. The SQUID can detect the change of magnetic flux created by mechanically moving the sample through a superconducting pick-up coil which is converted to a voltage. A SQUID is a flux-to-voltage transducer that can convert a small change in magnetic flux into voltage.

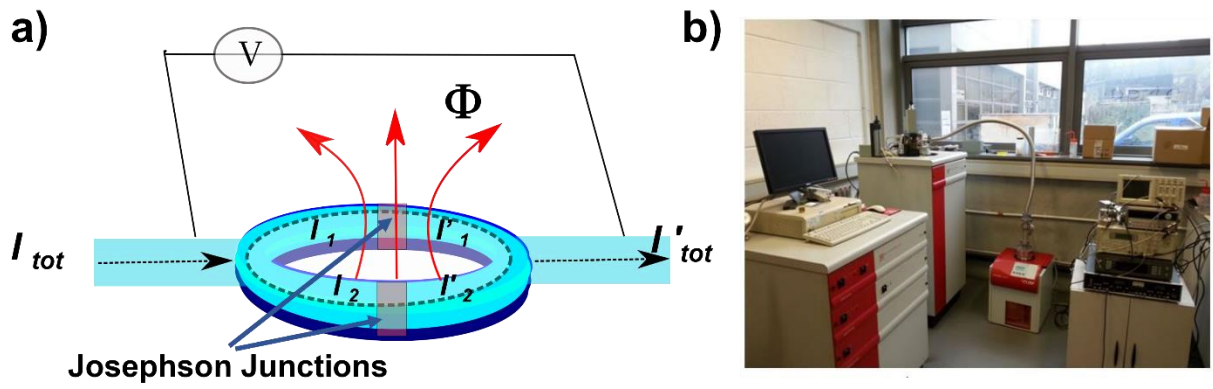


Figure 2. 3:a) Illustration of a DC SQUID, a superconducting loop with two Josephson junctions in parallel. Total current ($I_{tot}$) enters the loop and splits into two paths. A voltage (V) is measured across the loop and Φ is the externally applied magnetic flux (red arrows) b) DC SQUID magnetometry setup.

We made magnetometry measurements in a 5 T Quantum Design MPMS XL-5 SQUID magnetometer. For liquids, the sample must be filled inside a plastic cap made from a plastic straw of diameter ≈ 4 mm to fit into a long non-magnetic plastic straw. The magnetization measurements can be run from 4 K to 400 K and the applied field can be up to 5 T. The sample in the plastic cap is mounted at the centre of the straw. The cap makes a small diamagnetic contribution to the measured signal.

## 2.3 Experimental setup

In view of the small size of the droplet and limited space in the surroundings, we used permanent magnet configurations to generate the uniform and nonuniform fields. Unlike small electromagnets, permanent magnet arrays have the advantage that they generate no heat. The three configurations used are illustrated in Fig.2.4 a) is a uniform horizontal flux source, producing a field $B_y$ of up to 450 mT, depending on the separation of the magnets. b) is an array of five 10 mm magnet cubes made of Nd-Fe-B with a remanence of 1.26 T that produces a vertical field $B_z$ and a vertical field gradient $dB_z/dz$ along the vertical axis. c) is an array of three 10 mm magnet cubes that produces a horizontal field $B_x$ and a vertical field gradient $dB_x/dz$ along the vertical axis.

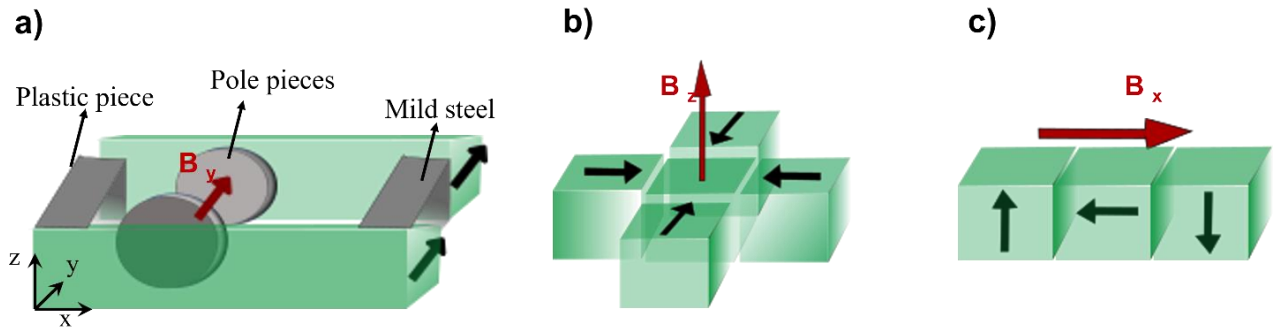


Figure 2. 4: Permanent magnet arrays used to apply magnetic fields to the pendant drop. A) Uniform horizontal field, b) Vertical field with a vertical gradient $dB_z/dz$ c) Horizontal field with a vertical gradient $dB_x/dz$.

The magnetic field profile of the uniform magnetic setup with rectangular permanent magnet and permendur pole pieces is shown in Fig.2.5.

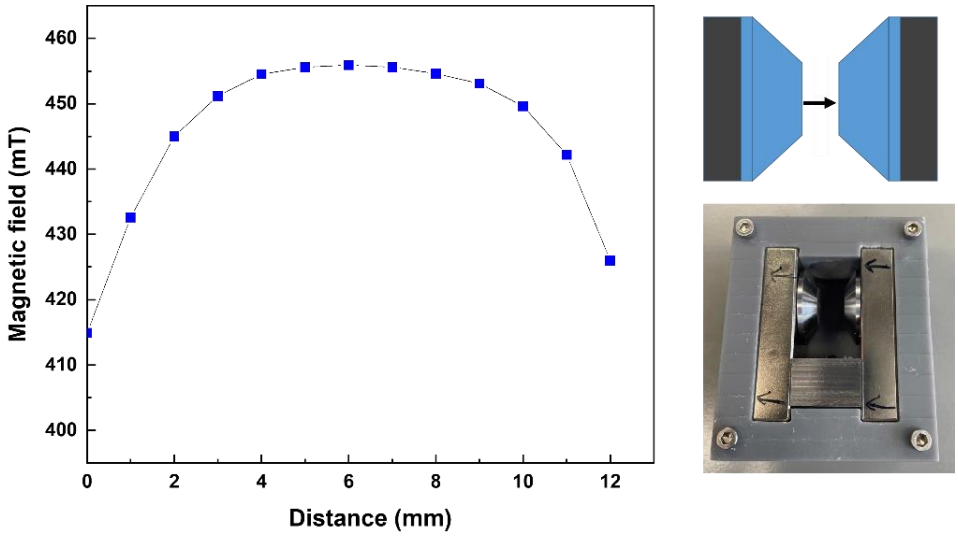


Figure 2. 5: Magnetic field profile of the uniform magnetic field assembly and an image of the assembly.

The droplet shape has been measured at different droplet distances away from the 3 and 5 magnet arrays. Different measurement positions of the centre of the droplet in the 5-magnet vertical field are indicated in Fig.2.6. Position 1, V1 which is 4 mm away from the surface of the magnet assembly is the closest position. Similar notation is used for the 3-magnet horizontal field assembly, where H1 is the position at a distance of 2 mm away from the surface of the magnet. Figures 2.7 and 2.8 show plots of $B$ and d$B$/d$z$ calculated as a function of distance from the surface for the 5-magnet and 3-magnet arrays. The field profile curve marks the magnetic field and field gradient on the drop at different positions.

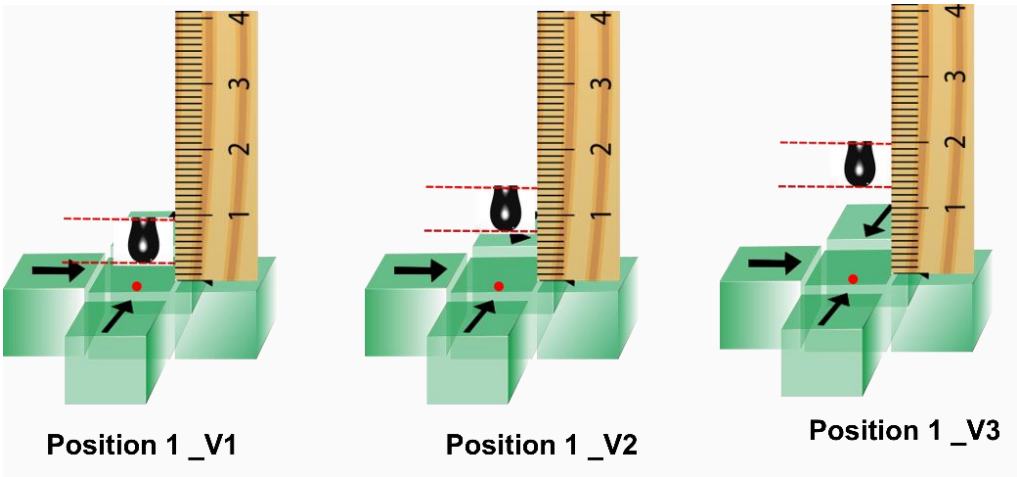


Figure 2. 6: Position of pendant drops at different heights from the surface of the 5-magnet magnetic assembly

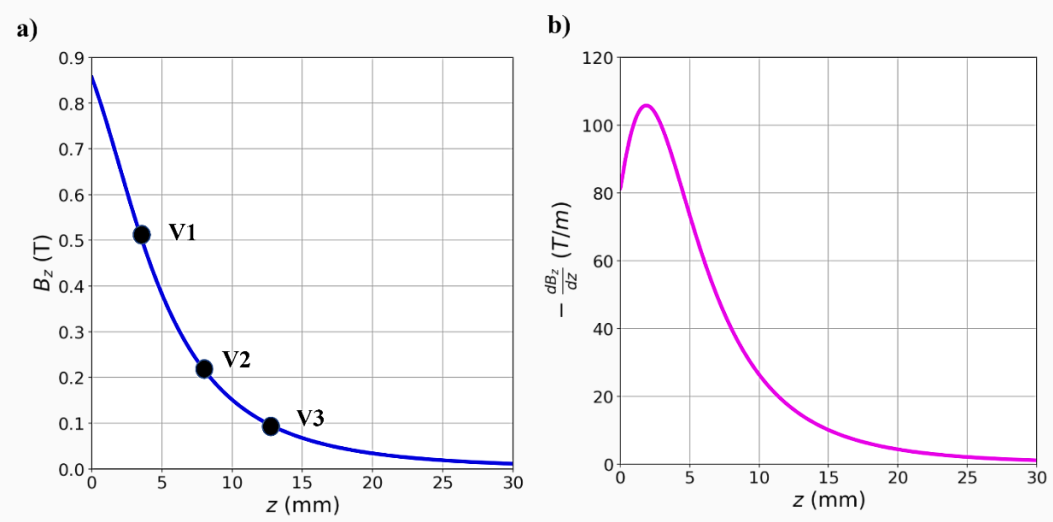


Figure 2. 7. The 5-magnet array with the values of a) $B_z$ and b) $dB_z/dz$ along the vertical axis. Black dots mark the positions of the centre of the droplet.

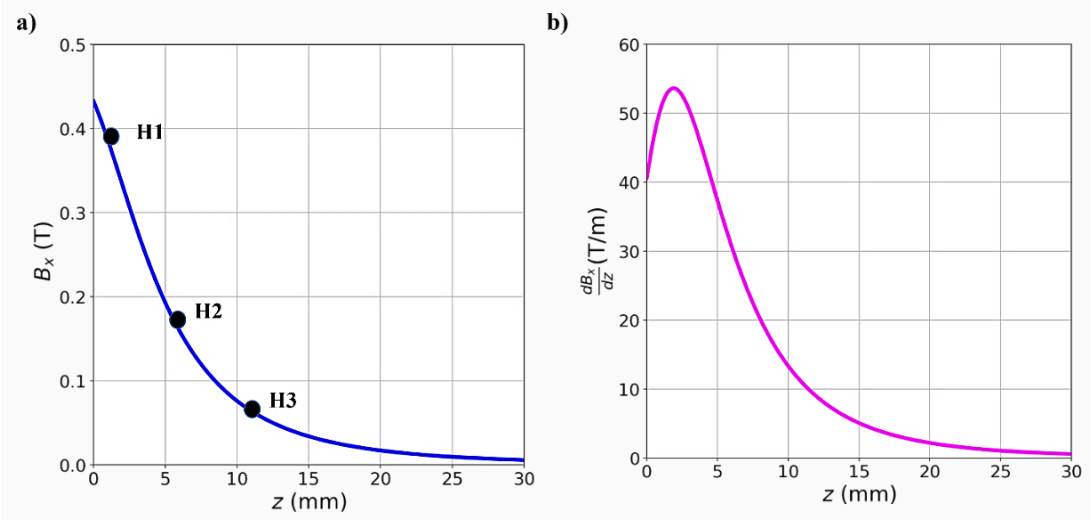


Figure 2. 8: The 3-magnet array, with the values of a) $B_x$ and b) $dB_z/dz$ along the vertical axis. Black dot marks the position of the centre of the droplet.

Measurements of the surface tension in a magnetic field were made as follows: First the liquid droplet was observed in the OCA 25 for a period of 60 seconds. Then the magnet array was raised to the measurement position and recorded for a further 60 seconds before lowering the magnet and re-establishing the zero-field background for a further 60 seconds, as shown in the Fig.2.9. In this way, any drift due to temperature change or evaporation can be corrected.

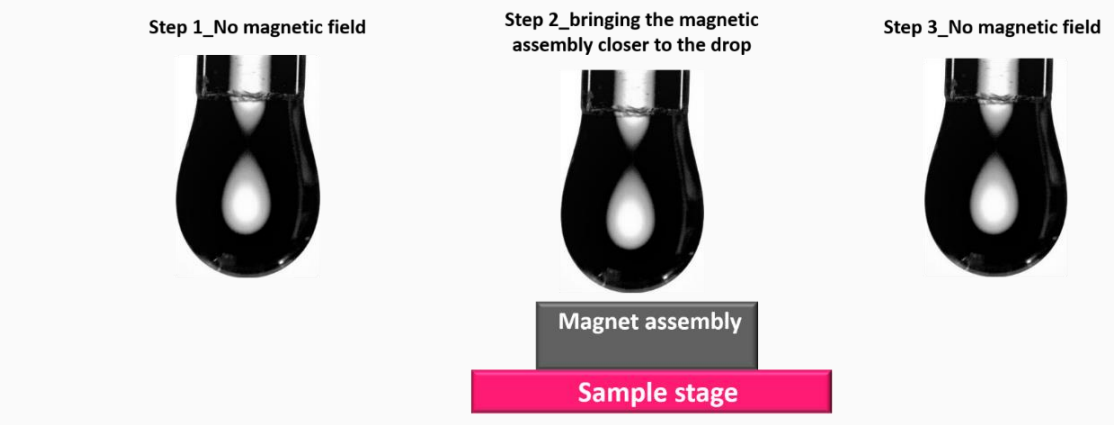


Figure 2. 9: The experimental steps for surface tension measurements

When a magnetic field is present, three effects that could influence the shape in addition to surface tension and gravity are,

i) The Kelvin force $\boldsymbol{F}_K = \chi \nabla B^2/2\mu_0$,

ii) Maxwell stress

iii) A change in surface tension of the liquid induced by the magnetic field

where $\chi$ is the dimensionless SI susceptibility of the liquid ($-9\times10^{-6}$ for water). A schematic representation of the additional forces that act on the drop is shown in Fig.2.10. For all the liquids we are concerned with here, $\chi << 1$, so any effects on surface tension will be linear in $B$.

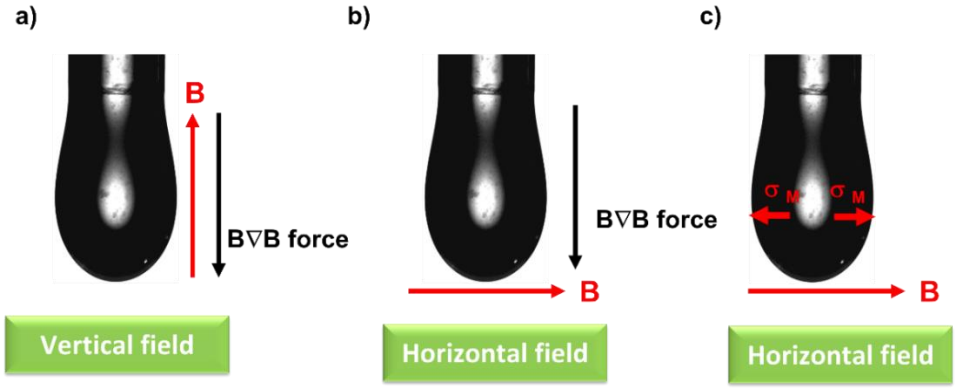


Figure 2. 10: Schematic diagram representing Kelvin $B\nabla B$ force in vertical and horizontal fields and the Maxwell stress $\sigma_M$. Three schematic droplets showing the fields and forces. a) in a vertical field with a vertical gradient, b) in a horizontal field with a vertical gradient and c) in a uniform horizontal field (Maxwell stress)

The Kelvin force (also known as the magnetic field gradient force or $B\nabla B$ force) is therefore vertical for a) and b), so its effect is to reduce the apparent density of diamagnetic liquids and increase it for paramagnetic liquids. When $\nabla B^2$ is big enough, it is possible to completely levitate water; the levitation condition is,

$$\rho g = \chi B \nabla B / \mu_0 \text{ or } B\nabla B = 1360 \text{ T}^2\text{m}^{-1}. \quad (5)$$

For example, if $B\nabla B = 100\ \mathrm{T^2 m^{-1}}$, the apparent density of water is reduced by 7%.

In order to understand the real magnetic field effects on surface tension of paramagnetic liquids, we have adopted a new zero susceptibility method. We make use of the fact that the dimensionless susceptibility of water is negative, $\chi_w = -9\times10^{-6}$, whereas that of 3*d* or 4*f* ions is positive and follows a Curie law

$$\chi = \mu_0 n g^2 p_{eff}^2 \mu_B^2 / 3 k_B T \qquad (6)$$

where n is the number of ions per unit volume. The effective Bohr magneton number $p_{eff}$ is $(S(S+1))^{1/2}$ for 3*d* ions and $(J(J+1))^{1/2}$ for 4*f* ions where *S* and *J* are the spin quantum number and the total angular momentum quantum number, respectively; g is the Landé g-factor [16]. The effective ionic moment is $p_{eff}\,\mu_B$ where $\mu_B$ is the Bohr magneton. The molar susceptibility $\chi_{mol}$ is obtained by replacing n by Avogadro's number $N_0$. The numerical expression for the susceptibility of a mole of ions is $\chi_{mol} = 1.571\times10^{-6}\ p_{eff}^2/T$. The susceptibility of an ionic solution of molarity *x* is therefore

$$\chi = 10^{-3}\chi_w + 1.571\times10^{-6}\ x p_{eff}^2/T. \qquad (7)$$

The first term is the susceptibility of a litre of water. It follows that there is a concentration of any particular paramagnetic ion where the net susceptibility is zero. In this case, Kelvin force and Maxwell stress effects are absent, and any change in the shape of the droplet must be attributed to a change in surface tension of the liquid. Table 1 lists the molar susceptibility of the three ions we considered, $Cu^{2+}$, $Mn^{2+}$ and $Dy^{3+}$, as well as the calculated molarity $x_0 = -9\times10^{-9}/\chi_{mol}$ of the zero-susceptibility solution where $\chi_{mol}$ is the molar susceptibility of the ions, given by Eq.6 with $n = N_0$, using a Landé g-factor of 2 for 3*d* ions and 4/3 for $Dy^{3+}$. Zero-susceptibility concentrations for the three ions at $T$ = 295 K are shown in Table 1. The zero-susceptibility

concentrations, $x_0^{exp}$ experimentally measured using SQUID magnetometry which is explained in §2.4.3

Table 1 Calculated and measured susceptibility at 295 K

| | $Cu^{2+}$ | $Mn^{2+}$ | $Dy^{3+}$ |
|---|---|---|---|
| $m_{eff}$ | 1.73 | 5.92 | 10.65 |
| $\chi_{mol}$ | $16\times10^{-9}$ | $187\times10^{-9}$ | $604\times10^{-9}$ |
| $x_0$ (M) | 0.56 | 0.048 | 0.015 |
| $x_0^{exp}$ (M) | 0.48 | 0.051 | 0.017 |

## 2.4 Results and Discussion

We have measured the surface tension of pure Millipore water, and solutions of 99% pure $CuSO_4$, $MnSO_4$ or $DyCl_3$ in deionised water with the following molarity: $CuSO_4$: 0.1, 0.38, 0.42, 0.45, 0.47 and 0.56 M; $MnSO_4$: 0.048 and 0.052 M and $DyCl_3$: 0.01, 0.05, 0.1, 0.4 and 1M. A uniform magnetic field, vertical magnetic field gradient and a horizontal magnetic field gradient have been used to record the apparent surface tension of liquids with different susceptibilities.

### 2.4.1 Magnetic field effects in a vertical field gradient

We have used water and dysprosium solutions for the surface tension measurements in the 5-magnet vertical field assembly. Changes in droplet shape in a magnetic field are parameterized by $\Delta\gamma_{app}$ in this chapter, which is defined as,

$$\Delta\gamma_{app} = \gamma_B - \gamma_0 \qquad (8)$$

where $\gamma_B$ is the value of surface tension returned by the analyser when a magnetic field is present and $\gamma_0$ is the value in zero magnetic field. Note that the body force acting on the droplet changes its shape, which the instrument interprets as a change in surface tension, since the effective gravitational acceleration is presumed constant. In diamagnetic water, there is a compression of the droplet, upwards, and an apparent increase in surface tension (or rather a decrease of effective gravitational acceleration), but for paramagnetic solutions, such as dysprosium chloride, the negative vertical magnetic field gradient results in a downward volume force and extends the droplet, corresponding to an apparent decrease in surface tension (or rather an increment in effective gravitational acceleration).

The apparent surface tension of water and different concentrations of dysprosium solutions have been measured at different drop positions, V1, V2, V3, from the magnet assembly. 0.01M, 0.05 M, 0.1M and 1M dysprosium solutions have been used to understand the dependence of the concentration of ions to surface tension.

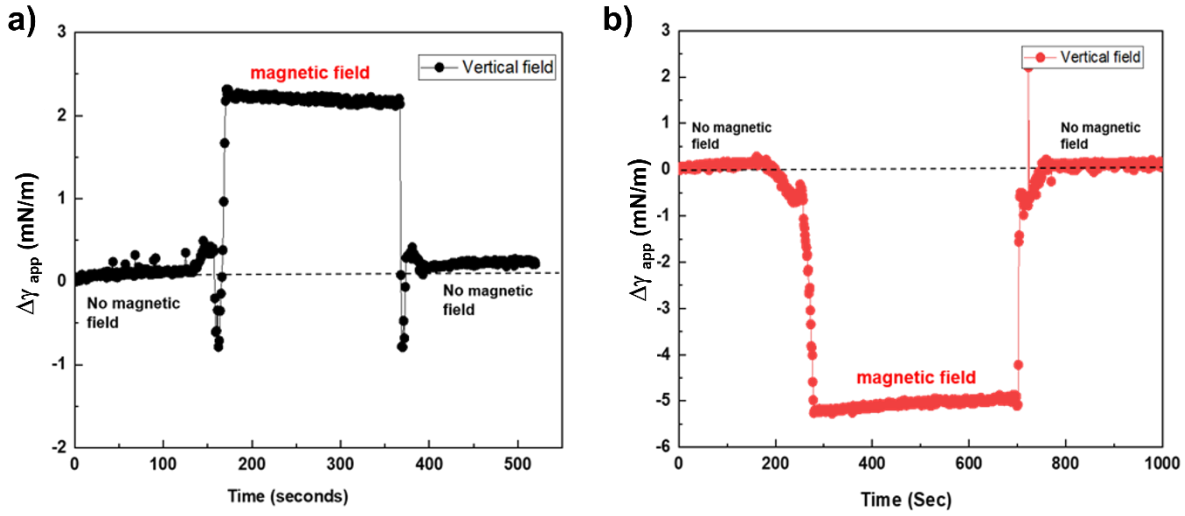


Figure 2. 11: Apparent surface tension changes $\Delta\gamma_{app}$ in a vertical magnetic field gradient a) Water, b) 0.1 M $DyCl_3$ at position 1.

Figure 2.11 shows apparent changes in the surface tension of water and 0.1M dysprosium droplets in a vertical magnetic field, based on the change of shape, as recorded by the OCA25. Observed changes of apparent surface tension are 2.2 $mNm^{-1}$for water and -5.1 $mNm^{-1}$ for dysprosium in the vertical gradient field of Fig.2.11 at position V1. This observation shows a significant change in apparent surface tension value for both solutions. We have observed an undershoot behaviour of water when a magnet brought near to the pendant drop. A careful analysis of the pendant drop at this points did not show any peculiar behaviour and therefore it could be due to the small vibrations on the drop during the magent movement. We repeated the experiments for a lower concentration of $DyCl_3$ as well and observed a surface tension change proportional to the concentration, as shown in Fig.2.12.

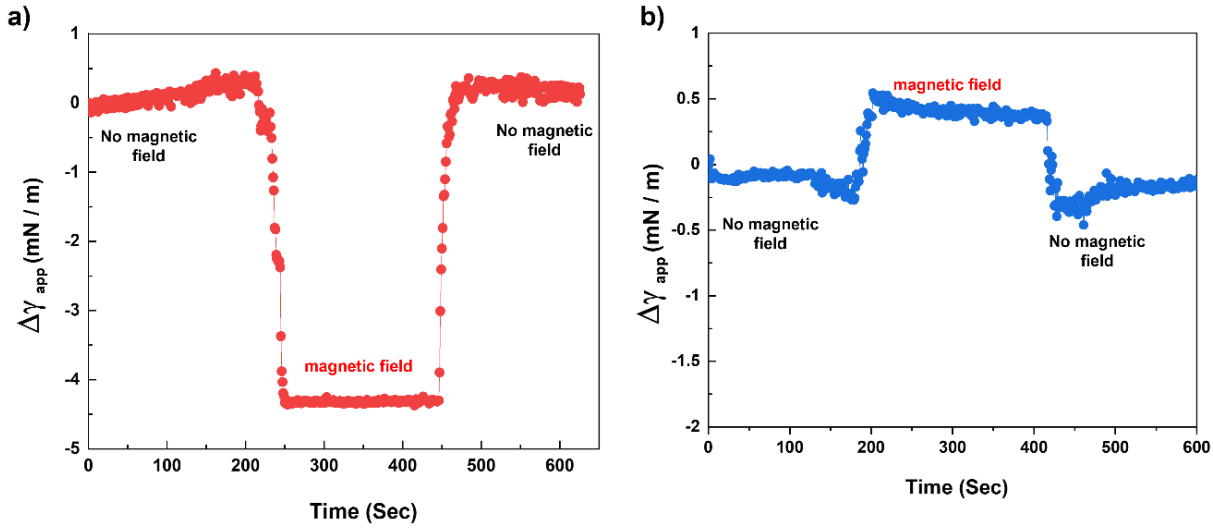


Figure 2. 12: Changes of apparent surface tension in a vertical magnetic field gradient a) 0.05 M $DyCl_3$, b) 0.01 M $DyCl_3$ at position 1.

0.05M and 0.01 M $DyCl_3$ solutions show apparent surface tension changes of - 4.4 $mNm^{-1}$ and + 0.4 $mNm^{-1}$, respectively. The positive value of surface tension for 0.01M implies the domination of the diamagnetic susceptibility of water in the solution over that of the paramagnetic dysprosium ions. It shows a direct relation of the apparent surface tension change

to the susceptibility of the solution. We monitored the apparent surface tension changes of a concentrated 1M dysprosium solution, shown in Fig.2.13 b).

Fig.2.13 shows the surface tension measurement of 0.05 M and 1 M $DyCl_3$ at various drop distances from the magnetic assembly. The surface tension change is much smaller when the drop is further away from the magnet. The magnetic field and field gradient decrease rapidly with distance. Thus field acts on the drop away from the magnet at positions of V2 and V3 are way lower than at V1. This explains why the surface tension changes are feeble at distances further away from the magnet. For higher concentration 1M Dy solutions, the drop breaks off at position 1 due to the higher field gradient. However, the apparent surface tension change is still higher, -3.5 $mNm^{-1}$ at position 2.

0.1M $DyCl_3$ solutions show a similar surface tension change as 0.05 M $DyCl_3$ though its concentration is double. Since the surface tension calculation is shape-dependent, there is a limitation to the elongation of the drop before the pinch-off. For 0.1M $DyCl_3$, the maximum elongation limit has reached, so the maximum apparent surface tension change it can show is 5.1 $mNm^{-1}$. Therefore, it is essential to check the shape of the pendant drop in the magnetic field since it is the shape that determines the surface tension calculation.

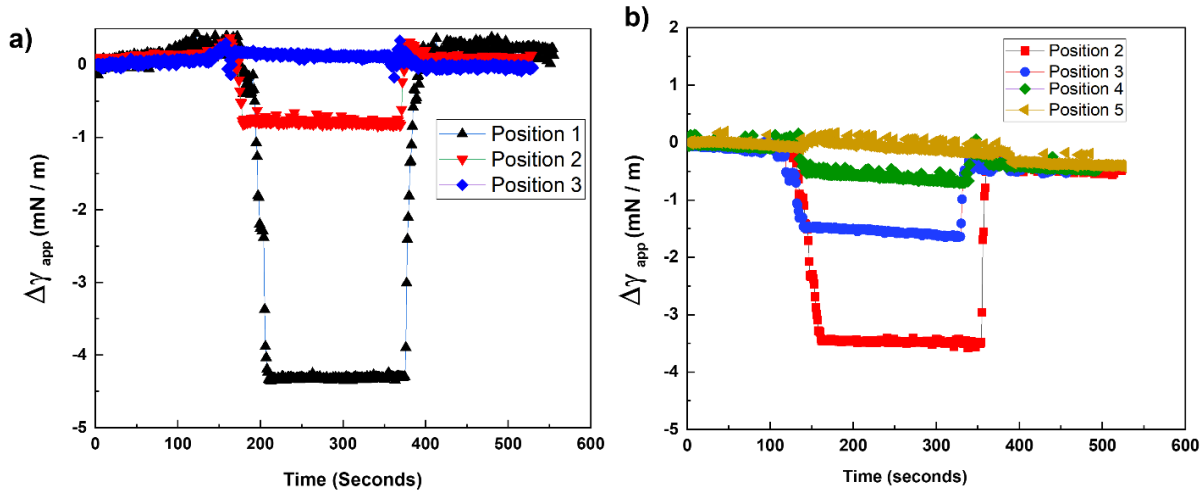


Figure 2. 13: Apparent changes in surface tension of a) 0.05 M $DyCl_3$ and b) 1M $DyCl_3$ in a vertical field gradient measured at different positions

The shape of the pendant drop has been extracted using a MATLAB code[1]. Two input images have been used; one when there is no field and the other with a magnetic field, to understand the effect of magnetic field on drop shape. The written MATLAB code extracts the contour of the drop images and superimpose it. Fig.2.14 shows a shape change of water and 0.1M $DyCl_3$ drop before and after applying the magnetic field. The green countour shows the drop shape when there is no magnetic field and the dotted red contour depicts the shape pof the drop when a magentic field is present. The water drop is compressed, corresponding to the apparent increase in surface tension, whereas dysprosium drop is extended when a magnetic field is present, corresponding to an apparent decrease in surface tension. Thus, we call it an apparent change in surface tension throughout the chapter. The change of drop shape in the magnetic field raises a question about whether the observed surface tension changes are real or a misinterpretation by the instrument. We will analyse this later in this chapter.

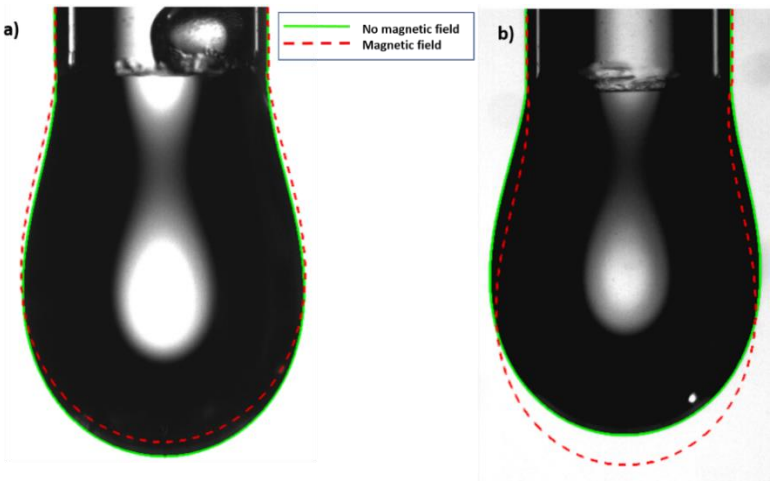


Figure 2. 14: Images of pendant droplet of a) water b) 0.1M $DyCl_3$ without and with a vertical field gradient magnetic field. Green drop contour is when there is no magnetic field and the dotted red contour shows the shape of the drop when a magnetic field is present.

[1] Code written by Ms. Jennifer Quirke

### 2.4.2 Magnetic field effects in a horizontal field gradient

A 3-magnet assembly with a horizontal magnetic field and a vertical field gradient have been used to monitor the surface tension changes of water and dysprosium solutions of different concentrations. In this configuration, the magnetic field direction and Maxwell stress are along the same direction. This configuration was originally designed to understand the Maxwell stress effect on the shape of the pendant drop, which turns out to be negligible.

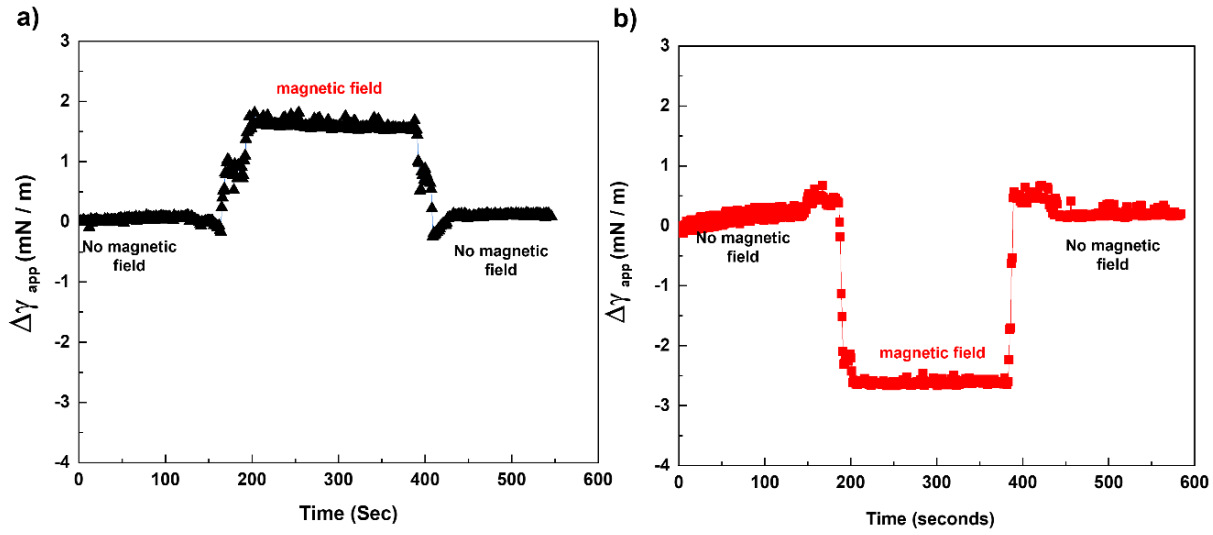


Figure 2. 15: Apparent surface tension changes in a vertical magnetic field gradient a) Water, b) 0.1 M $DyCl_3$

The apparent surface tension changes in a horizontal magnetic field for water and 0.1M $DyCl_3$ are + 1.8 $mNm^{-1}$ and -2.8 $mNm^{-1}$, respectively, as shown in Fig.2.15. The magnitude of apparent surface tension is lower than in the vertical field gradient since the magnetic field strength and field gradient are lower. The measured surface tension of 1M $DyCl_3$ drops at different distances from the magnet is given in figure 5.16. The drop breaks off at position H1 due to the high field gradient forces as it does in the vertical field gradient.

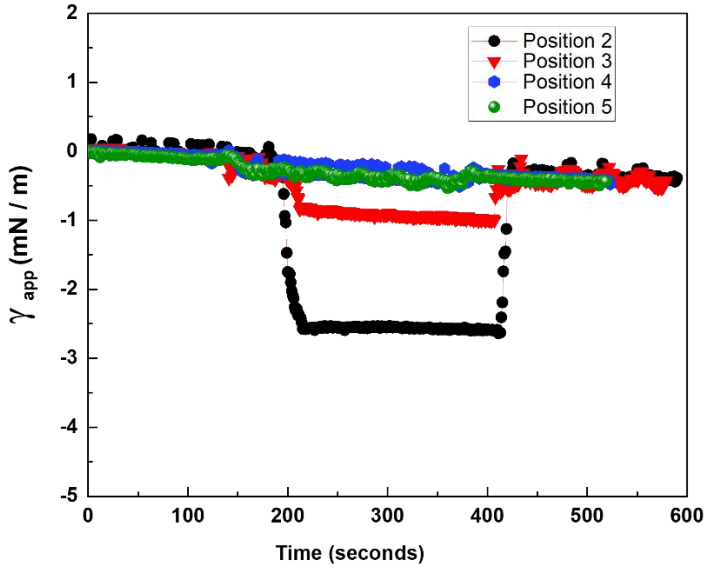


Figure 2. 16: Apparent changes in surface tension of 1 M $DyCl_3$ in a horizontal field with a vertical field gradient at different positions

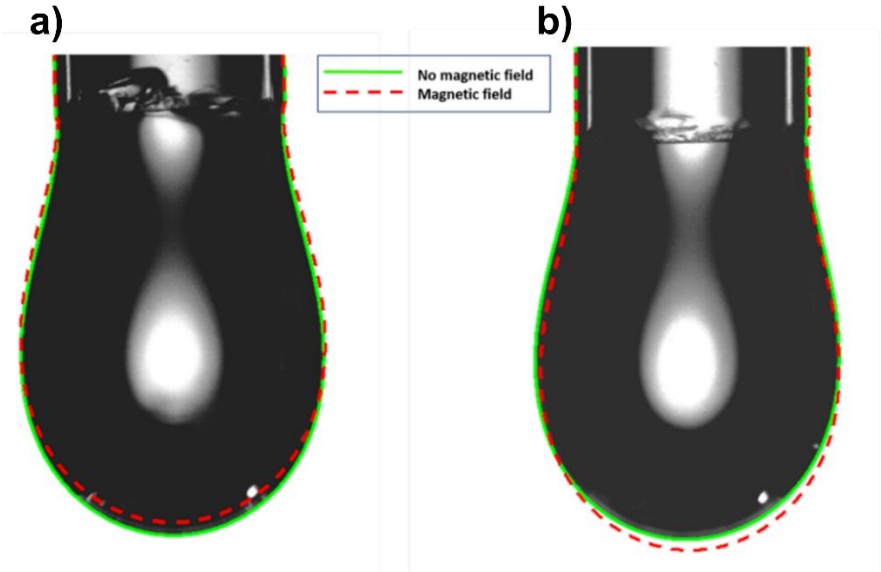


Figure 2. 17: Images of pendant droplet of a) water b) 0.1M $DyCl_3$ without and with a horizontal magnetic field with a vertical field gradient.

The change of drop shape shown in Fig.2.17, in a horizontal field follows a similar trend to that of the vertical field but to a smaller extent. The body force acting on the droplet in the inhomogeneous field changes its shape, which the instrument interprets as a change in surface tension. The observed change in apparent surface tension $\Delta\gamma_{app}$ is largely influenced by the shape change of the drop in the magnetic gradient field. Depending on the solution's magnetic susceptibility, the field gradient force acting on the drop elongates or compresses it. The $B\nabla B$ value is 14 $T^2m^{-1}$ for the 3-magnet horizontal field at position H1 and 80 $T^2m^{-1}$ for the 5 magnet vertical field at position V1.

Levitation of water means that it behaves as if it has an effective density of zero. Thus the $B\nabla B$ force on a droplet is equivalent to an effective change of density. This does not imply that the density of the droplet really changes, it is only an apparent change due to the magnetic gradient force. We measure the apparent change of surface tension at different positions in horizontal and vertical fields, and in each case, use the analyser to find the corresponding change of apparent density $\Delta\rho_{eff}$ that will give the same reading. For water, the apparent increase in surface tension is in good agreement with the effective decrease in density as shown in figure 2.18 a). The effective changes of density for water in vertical and horizontal magnetic field assemblies would be -6% and -1%, while the corresponding changes for 0.1 M $DyCl_3$ are 39% and 7%, respectively.

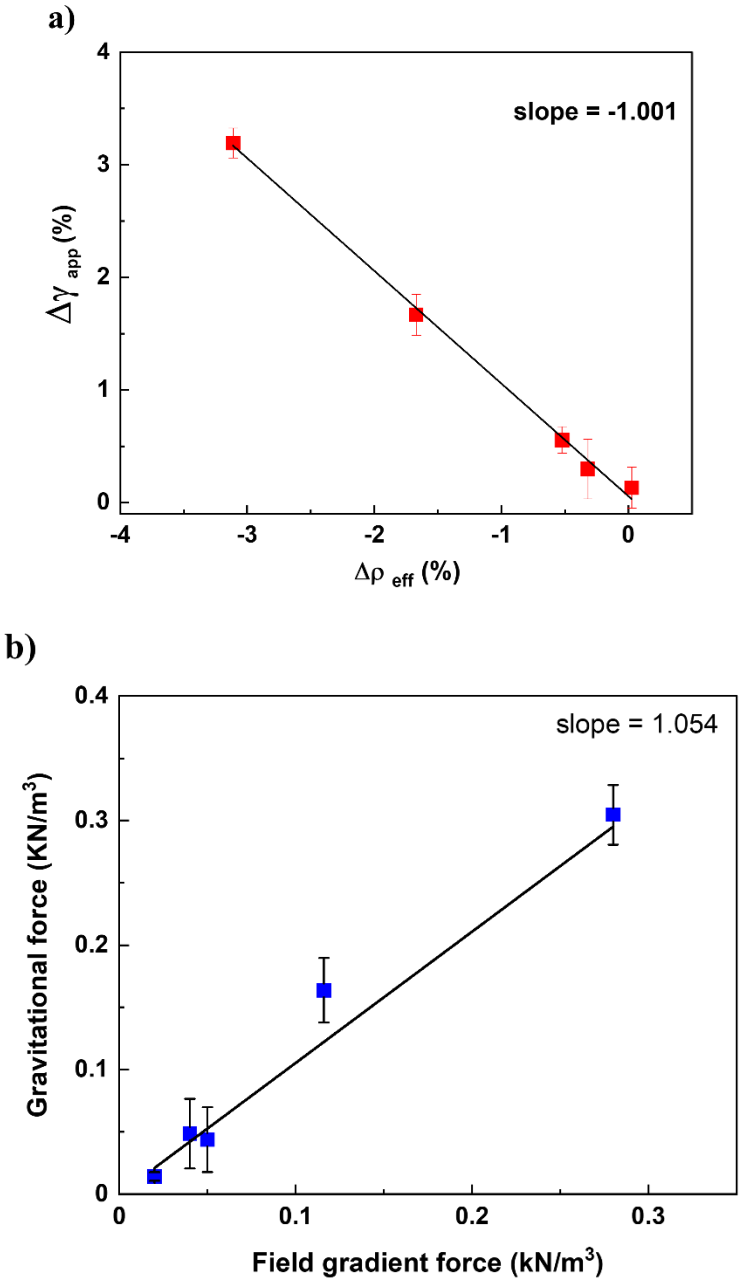


Figure 2. 18: Plots of $\Delta\rho_{eff}$ (%) calculated from Eq 5 versus measured change in apparent surface tension ($\Delta\gamma_{app}$ ) for water and b) plot of gravitational force versus field gradient force of water.

Figure 2.18 a) is a plot of the measured apparent surface tension changes computed by the OCA 25, against the change of density needed to fit the droplet shape at constant surface tension. The slope of the graph is -1.00 ± 0.02, as expected, because $\gamma$ depends linearly on $\rho$, for small changes. In Figure 2.18b) we plot the change in gravitational force corresponding to the change of density needed to fit the droplet shape against the field gradient force obtained from the known values of $B\nabla_z B$, using Eq.6 for force, both in $kNm^{-3}$. Here the slope is 1.05 ± 0.09. This suggests that there is no appreciable change in surface tension due to the applied field. The value in a field of 0.5 T (that of the 5-magnet array at position V1) is 0.13 ± 0.2 $mNm^{-1}$.

The gravitational force calculated from the apparent change in density of the liquid in a magnetic field is in good agreement with field gradient force, as in Fig. 2.18 b). This shows that the apparent change in surface tension, which can be expressed as a change in density, is caused by magnetic field forces. This supports our idea that when a magnetic field is present, the tensiometer misinterprets the drop shape change as a surface tension change.

Further presentation of the force effects on the high concentration paramagnetic solutions 1M, $MnSO_4$, 1M $DyCl_3$ are shown in Fig. 2.19. For $MnSO_4$ solutions the gravitational and field gradient forces seem to agree, although we only have two points on the plot, whereas points for the $DyCl_3$ solutions are not close to slope 1. Therefore, the change in density is no longer only proportional to the $B\nabla B$. The plot of $\Delta\gamma_{app}$ (%) versus $\Delta\rho_{eff}$ (%) graph shows consistency with the lower molarity solutions data, when fitted with a fixed slope of -1 for both 1 M $MnSO_4$ and $DyCl_3$ solutions.

For paramagnetic solutions, the magnetic field gradient force stretches the drop downwards, towards the magnet and the extent of the stretching increases with concentration of the paramagnetic solution. The limiting factor to the stretching here is the shape of the pendant drop just before the pinch-off limit. There is a threshold extension for the paramagnetic pendant drop, beyond which the drop detaches and sticks to the magnet. Thus the maximum stretching deformation is much the same for 0.1 M $DyCl_3$ and 1 M $DyCl_3$, as is determined by the critical

nature of the necking process. All the measurements are made on droplet shapes that are stable, which limits the measurements of $\Delta\gamma_{app}$ to a maximum of -4 $mNm^{-1}$.

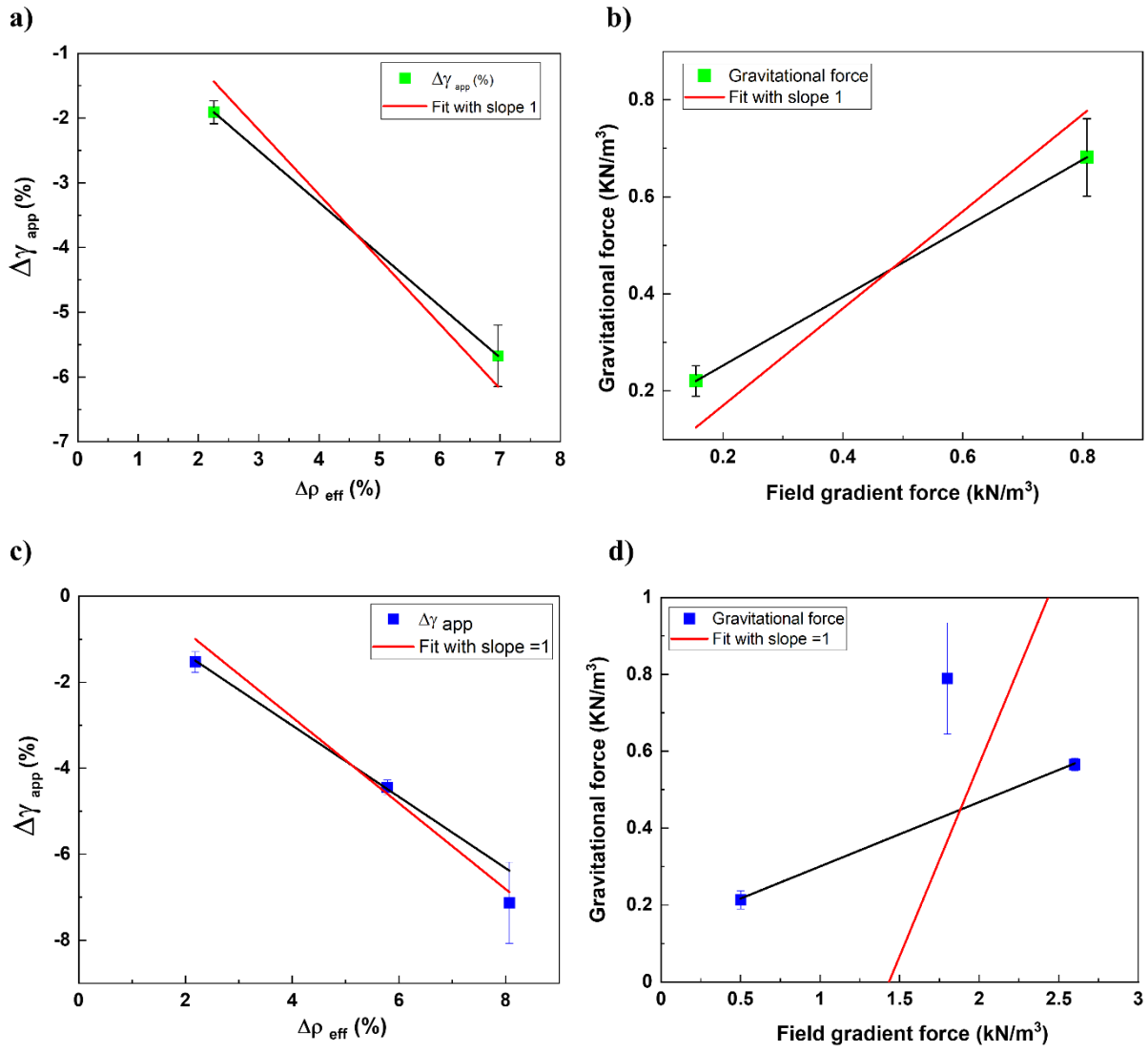


Figure 2. 19: Figure a) and c) are plots of $\Delta\rho_{eff}$ (%) calculated from Eq 5 versus measured change in apparent surface tension ($\Delta\gamma_{app}$ (%)) for 1M $MnSO_4$ and 0.1 M and 1M $DyCl_3$ respectively and b), d) are plot of gravitational force versus field gradient force of 1M $MnSO_4$ and 0.1 and 1M $DyCl_3$. Black line connects the datapoints and the red line is the fit with a fixed slope of 1.

### 2.4.3 Zero susceptibility method

We have used a zero susceptibility method to eliminate all magnetic body forces on the droplet, in order to look for any intrinsic magnetic field effect on surface tension of magnetically undeformed droplets. Since any surface tension change is likely to be small, it is important to ensure that the solutions we are using really have zero susceptibility. This cannot be assured reliably just based on mass measurements before dissolving the salts in water. The soluble salts are hygroscopic and readily absorb water before and during weighing, and there might be some slight deviations from the theoretical Curie law due to weak interionic exchange related to the association of ions in the solution, for example.

Furthermore, Eq 7 is valid only in the dilute limit, when the density of water is independent of the concentration of dissolved ions. This is a questionable assumption for 0.5 M $CuSO_4$. We, therefore, measured the susceptibility of the solutions directly in a SQUID magnetometer, in the range -5 T to 5 T. The data for determining $x_0^{exp}$ for $CuSO_4$, $MnSO_4$ and $DyCl_3$ solutions is shown in Fig. 2.20. The experimentally determined zero-susceptibility solutions are given in the fourth row of table 1.

Experimentally measured zero susceptibility for $CuSO_4$, $MnSO_4$ and $DyCl_3$, values were a little different (14%), compared to $x_0$ (see Table 1). We then measured the change of surface tension induced in a vertical magnetic field as a function of concentration to the value of $\Delta\gamma$ when there is no magnetic body force. Some data are shown in Fig.2.21 for $CuSO_4$.

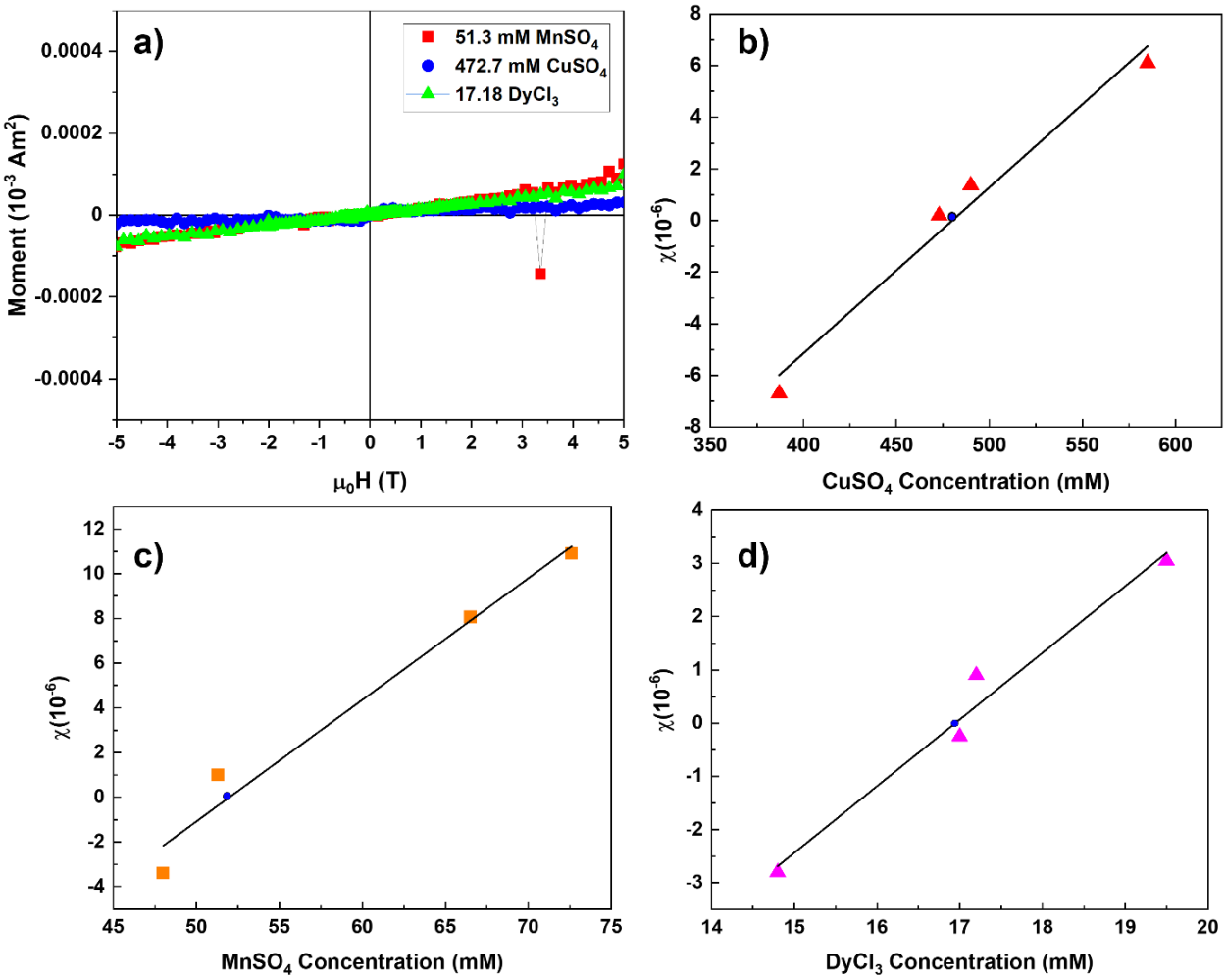


Figure 2. 20: a) SQUID measurements of the zero moment $CuSO_4$, $MnSO_4$ and $DyCl_3$ solutions. Zero susceptibility optimisation of different concentrations of b) $CuSO_4$, c) $MnSO_4$, d) $DyCl_3$. The blue dot in the figures marks the zero-susceptibility concentration in each case.

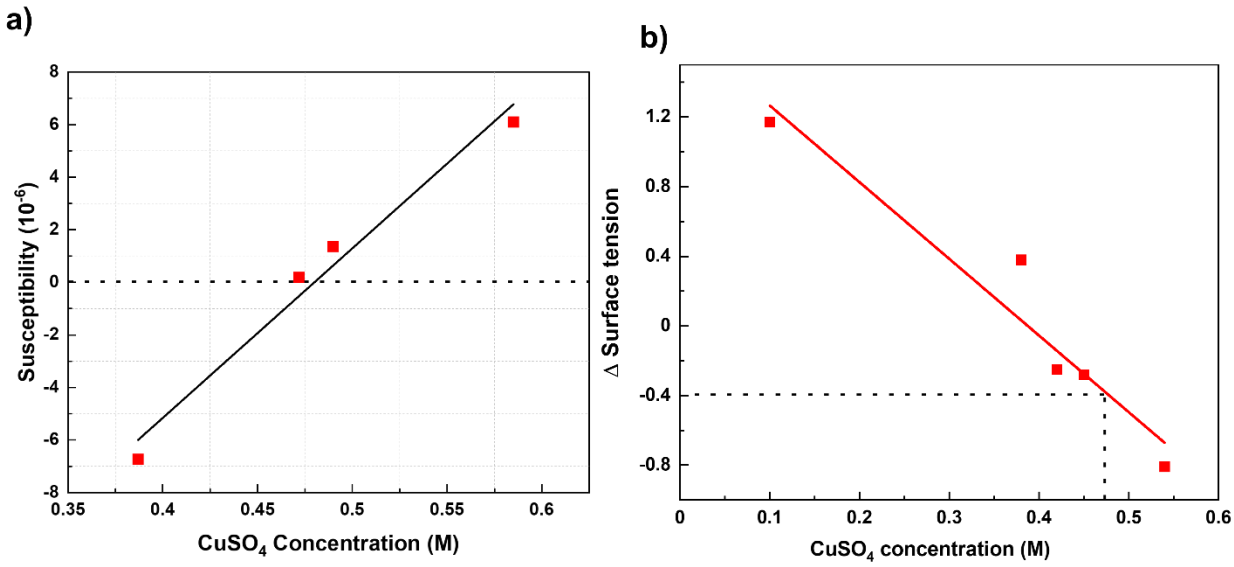


Figure 2. 21: a) Zero susceptibility optimisation of different concentrations of $CuSO_4$, using SQUID data b) Variation of apparent surface tension as a function of the concentration of copper solutions

The zero-susceptibility method gives an accurate measurement of the magnetic field effect on the surface tension of the ionic solutions. The change of surface tension from Fig.2.21 b) for $CuSO_4$ in 0.5 T is ~ -0.40 $mNm^{-1}$ . It is a real change, not a result of a magnetically-induced change of shape since the magnetic body forces, Kelvin force and Maxwell stress, are absent when the susceptibility is zero. The corresponding results for $MnSO_4$ and $DyCl_3$ are -0.48 $mNm^{-1}$ and -0.30 $mNm^{-1}$. The values for the ionic solutions are all small, but opposite in sign to the result for pure water in a uniform field, 0.19 ± 0.21 $mNm^{-1}$ (see below).

### 2.4.4 Magnetic field effect on water and zero susceptibility solutions in a uniform field

We have used pure water and different concentrations of $DyCl_3$, $MnSO_4$, $CuSO_4$ and the magnet configuration of Fig. 2.4 a) to see how a uniform magnetic field affects the surface tension.

For water in a uniform field, the effect of Maxwell stress is negligible, and there is no field gradient, so any effect must be attributed to a magnetically-induced change of the surface tension of water. We repeated the experiment 37 times as given in table 2 and observed an average surface tension change of $0.19 \pm 0.21$ $mNm^{-1}$, where the error is the standard deviation on the mean. The droplet is only perturbed while it experiences the gradient field of the magnet (in the transitions only), and these up-thrust regions lead to a temporary distortion of the droplet shape. The wetting conditions at the edge of the capillary may be slightly altered each time, thus leading to the relatively large error estimate of the effect of the uniform field on surface tension. Uncertainty may occasionally arise from small changes in wetting area at the capillary upon the raising and lowering of the magnet assembly. It is impossible to avoid subjecting the drop to a field gradient when moving the magnets, even when the homogenous field magnet in Fig. 2.4a) is used.

Table 2: Surface tension measurements of water in a uniform 450 mT field

| **Measurement Number** | $\Delta\gamma$ **(** $mNm^{-1}$**)** | **Measurement Number** | $\Delta\gamma$ **(** $mNm^{-1}$**)** | **Measurement Number** | $\Delta\gamma$ **(** $mNm^{-1}$ **)** |
|---|---|---|---|---|---|
| 1 | -0.32 | 13 | 0.21 | 25 | -0.04 |
| 2 | -0.17 | 14 | 0.22 | 26 | -0.02 |
| 3 | -0.12 | 15 | 0.31 | 27 | 0.37 |
| 4 | -0.11 | 16 | 0.32 | 28 | 0.24 |
| 5 | 0 | 17 | 0.37 | 29 | 0.34 |
| 6 | 0.05 | 18 | 0.07 | 30 | 0.31 |
| 7 | 0 | 19 | 0.20 | 31 | 0.39 |
| 8 | 0.40 | 20 | 0.02 | 32 | 0.42 |
| 9 | 0.56 | 21 | 0.16 | 33 | 0.35 |
| 10 | 0.27 | 22 | -0.13 | 34 | 0.43 |
| 11 | 0.17 | 23 | -0.10 | 35 | 0.25 |
| 12 | 0.13 | 24 | 0.85 | 36 | 0.39 |
| | | | | 37 | 0.33 |
| | | | | Mean | 0.19 ± 0.21 |

In the 450 mT uniform field, the surface tension changes corresponding to the zero-susceptibility concentration are -0.50 ± 0.35 $mNm^{-1}$ for $DyCl_3$ (9 measurements), -0.51±0.50 $mNm^{-1}$ for $MnSO_4$ (15 measurements) and -0.11 ± 0.50 $mNm^{-1}$ for $CuSO_4$ (21 measurements).. This sign of the effect in each case is always negative in the uniform field, just as we found for the zero-moment solutions in the gradient field in § 2.4.3, and it is opposite in sign to the effect in deionized water.

### 2.4.5 Non-uniform magnetic field gradient forces on concentrated Dy solutions.

The apparent decrease in surface tension of Dy solutions in the field is much underestimated. This is a reflection of the spatial variation of the magnetic field *gradient* over the volume of the droplet.

The introduction of inhomogeneous field gradients to the problem results in a spatial variation of the body force experienced by the drop. This can be explicitly taken into account in the modelling by an additional term in the right-hand side of eq. 2 (§2.2.1), of the form: $\Delta\rho.[g + (dg/dz).z](z/\gamma)$, taking into account, not any changes of the gravitational acceleration, but rather changes of the field gradient product along the main (vertical) *z*-axis. We have included this additional term in an version of the differential solver used to integrate eq. 1- 4, in an improved MathCad™, computational and fitting routine [2]. The ability to extract this additional parameter $\delta = dg/dz$, depends on the level of pixel noise in the images of the drops acquired and the overall amount of non-trivial droplet shape deformation, which can be provided by the gradient field magnetic assemblies used.

Analysis of second-order effects on droplet shape goes beyond the routine analysis provided by the manufacturer's software described in the introduction, by introducing the effective gradient of gravitational acceleration into the standard model of differential equations. An example of this process is shown in Fig. 2.22.

[1] Code written by Prof Plamen Stamenov

It can be seen that the quality of the shape parameter fit is improved by the introduction of this additional free parameter. Its reliable extraction, however is impeded by the spatial resolution of the acquired images (pixel density) and random pixel noise, which control the precise extraction of the droplet profile. The fitted values of the effective parameters for the fit of figure 2.22 are: $\gamma$ = 55.5 $mNm^{-1}$, $\delta$ = -9.6 g/m. This extracted surface tension value agrees with the observed surface tension value of zero field 0.1M $DyCl_3$ solution; 68 $mNm^{-1}$. The high value of the effective gradient of the gravitational acceleration is primarily due to the maximal gradient field product of 80 $T^2m^{-1}$ and the substantial susceptibility of the $DyCl_3$ solution of + $59 \times 10^{-6}$.

In summary, magnetic field gradients thus provide a relatively convenient way to investigate the effects of inhomogeneous body forces (gravity) on liquid drops, without the complexity and cost of microgravity experimental environments, following the same underlying principles as magnetic levitation. As the solution used here is more than a factor of ten below the solubility saturation limit, there is potential to increase the magnitude of the observed effects by up to an order of magnitude, preserving the simplicity of the magnet arrays used.

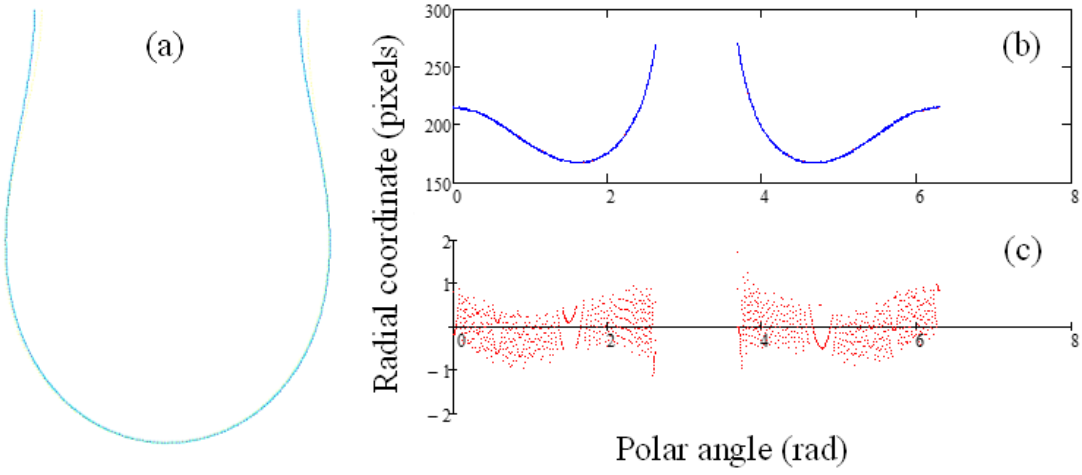


Figure 2. 22: An example of the fitting process for a 0.1 M $DyCl_3$ solution, using the vertical gradient 5-magnet array. (a) a representation of the border of the drop`s projection (b) the fitted data and fitting curve in polar coordinates (c) residual plot of the fit in polar coordinates.

We end this section with a brief discussion of Maxwell stress[17,18]. Consider a spherical drop with susceptibility $\chi$ in a uniform horizontal magnetic field, as shown in Fig. 2.23. When $\chi \lesssim 10^{-3}$, demagnetizing effects are negligible. The drop has uniform magnetization $\boldsymbol{M} = \chi \boldsymbol{H}_0$, which can be represented by a surface magnetic charge density $\sigma_m = \boldsymbol{M}.\mathbf{e}_n$, where $\mathbf{e}_n$ is the surface normal. This results in a tensile stress $\sigma$, as shown in the figure, and a spheroidal deformation of the drop, with half axes c and a, where c = a(1+x). We compare the pressures at the points A and B, as shown. There is no magnetic pressure at A, since $\boldsymbol{M} \perp \mathbf{e}_n$, but at B $\boldsymbol{M} \parallel \mathbf{e}_n$, and $\sigma_m = \chi H_0$. The magnetic pressure is therefore $P_m = \mu_0 H_0 \sigma_m = {}^1/_2\, \chi\, \mu_0 H_0^2$. If $\mu_0 H_0$ = 500 mT and $\chi$ = 10 x$10^{-6}$, $P_m$ = 1 Pa. We equate this to the pressure difference between points A and B. Each is given by Eq. 1, where the two radii of curvature at point A are $c^2/a$ and a and at point B both are $a^2/c$. Setting c = a(1 + x), we find $P_m$ to first order in z

$$P_B - P_A = 4x\gamma/a \,. \qquad (9)$$

Taking a = 2 mm, we find that the deformation of the drop is x = 0.7 %. The Maxwell stress would therefore produce an oblate compression of 0.6 % in the shape of a spherical drop of water and a 3.5% prolate extension shape of a spherical drop of 0.1M Dy solution. The effects in pendant droplets will be similar. There effects are small in relation to the droplet deformations illustrated in Fig. 2.14.

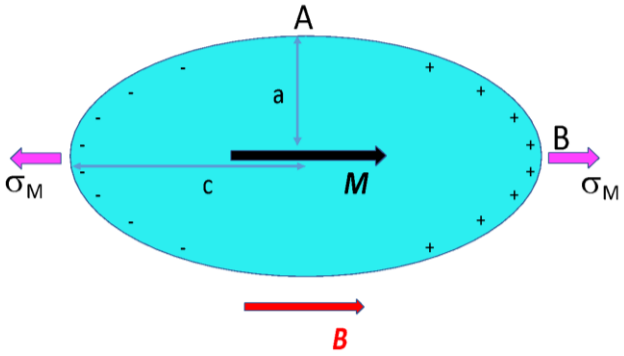


Figure 2. 23: Prolate deformation of a spherical drop with a positive susceptibility due to Maxwell stress $\sigma_M$ due to the distribution of positive and negative magnetic charge induced by the magnetic field

## 2.5 Conclusions

Magnetic field effects on surface tension can be evaluated from droplet shape in either of two ways — in a uniform magnetic field, or in aqueous solutions of paramagnetic ions where the Curie-law paramagnetism cancels the diamagnetism of water to give zero net magnetic susceptibility, and therefore no magnetic body force. The effects are small; the first method applied to water gives changes that are barely significant, $0.42 \pm 0.47$ $mNm^{-1}T^{-1}$. The second method, applied to zero-susceptibility solutions of $Cu^{2+}$, $Mn^{2+}$ and $Dy^{3+}$ gives negative values in the range -0.77 to -1.13 $mNm^{-1}T^{-1}$. These measurements should be extended to much larger, uniform magnetic fields.

The shapes of pendant droplets of water and paramagnetic solutions are mainly deformed by the magnetic field gradients produced by permanent magnet arrays. Uniform vertical field gradients over the droplet volume are equivalent to changes of effective liquid density. The corresponding changes of droplet shape are interpreted by the droplet analyser as changes of 'apparent surface tension'. Nonuniform magnetic field gradients, however, produce droplet deformations that cannot be interpreted using the standard fitting algorithm. The droplet shapes can be fitted by adding a term with a gradient of gravitational acceleration into the differential equations. These second-order effects are dominant for strongly-paramagnetic solutions and have been calculated for 0.1 M $DyCl_3$. An 'effective surface tension' of 55.5 $mNm^{-1}$ has been measured in 0.1M $DyCl_3$ in an 'effective gravity gradient' of 0.1 $ms^{-2}$/mm. Such analysis of the non-uniform Kelvin force over a pendant drop requires high-resolution images of the droplet shape. The standard fitting algorithms are inapplicable for such solutions in a nonuniform magnetic field. Maxwell stress makes a minor contribution to the deformation.

Our method of measuring the static droplet deformation, which images the droplet in zero field before and after imaging it in the presence of the field, involves moving the permanent magnet array to and from the droplet and exposing it to a variable, transient field gradient. The method provides the zero-field baseline and allows the correction of small drifts in the course of a measurement, but there is an upper limit to the susceptibility that can be measured in a iven

magnet array, beyond which the droplet is pulled off when the magnets are first moved towards it. Measurements of changes in ‘apparent surface tension’ are limited to about 6 $mNm^{-1.}$

# Bibliography

[1] P. Lambert and M. Mastrangeli, Micromachines **10** (2019).

[2] A. Dunne, W. Francis, C. Delaney, L. Florea, and D. Diamond, in *Reference Module in Materials Science and Materials Engineering* (Elsevier, 2017).

[3] D. Baigl, Lab on a Chip **12**, 3637 (2012).

[4] K. Koch, B. Dew, T. E. Corcoran, T. M. Przybycien, R. D. Tilton, and S. Garoff, Mol Pharm **8**, 387 (2011).

[5] N.-T. Nguyen, Microfluidics and Nanofluidics **12**, 1 (2012).

[6] A. V. Zakharov, P. V. Maslennikov, and S. V. Pasechnik, Physical Review E **101**, 062702 (2020).

[7] I. M. Hauner, A. Deblais, J. K. Beattie, H. Kellay, and D. Bonn, The Journal of Physical Chemistry Letters **8**, 1599 (2017).

[8] M. Amiri and A. Dadkhah, Colloids and Surfaces A: Physicochemical and Engineering Aspects **278**, 252 (2006).

[9] Y. Fujimura and M. Iino, Journal of Physics: Conference Series **156**, 012028 (2009).

[10] Y. Fujimura and M. Iino, Journal of Applied Physics **103**, 124903 (2008).

[11] E. Chibowski, A. Szcześ, and L. Hołysz, Colloids and Interfaces **2** (2018).

[12] M. Hayakawa, J. Vialetto, M. Anyfantakis, M. Takinoue, S. Rudiuk, M. Morel, and D. Baigl, RSC Advances **9**, 10030 (2019).

[13] A. Szcześ, E. Chibowski, and E. Rzeźnik, Colloids and Interfaces **4** (2020).

[14] H. U. O. Zhong-feng, Z. Qian, and Z. Ying-hua, Procedia Engineering **26**, 501 (2011).

[15] A. Katsuki, K. Kaji, M. Sueda, and Y. Tanimoto, Chemistry Letters **36**, 306 (2007).

[16] J. M. D. Coey, (2009).

[17] J. Dodoo and A. Stokes, Physics of Fluids **32**, 061703 (2020).

[18] R. E. Rosensweig, *Ferrohydrodynamics* (Dover Publications, New York, 1997).

# Chapter 3

# Magnetic field effects on evaporation of water and solutions of NaCl and Urea

## 3.1 Introduction

The modification of the physical and chemical properties of water by exposure to a magnetic field has been a topic of interest and debate for many years. Most controversial have been claims that by passing hard water through a non-uniform magnetic field, it is possible to influence the subsequent precipitation of limescale when the water is heated. These claims were widely dismissed, despite a body of experimental evidence to the contrary, because no mechanism could be envisaged whereby fleeting exposure of an isotropic, homogeneous solution to a magnetic field could influence its chemical behavior hours later. The picture changed when it emerged[1,2] that calcium carbonate solutions were not simply dispersions of calcium cations and bicarbonate anions in water, but that a significant fraction of the calcium was bound in 'Dollops', nanoscale polymeric clusters of amorphous soft matter, that act as prenucleation seeds for the eventual nucleation of calcium carbonate from supersaturated solution[3]. The new theory of nucleation is itself under debate [4], but it opens the possibility of understanding the long-term consequences of exposing hard water to a magnetic field[5].

Magnetic memory of water is another controversial topic that proposes the sustained effects of magnetic field exposure in water after removing magnetic fields [6,7]. A detailed study of magnetic water treatment in a capillary tube and the relaxation time for restoration by Azoulay

et al.[6], found a memory effect as weak as 0.12 T for 210 minutes. Colic et al.[7]explained magnetic memory as it persists due to the relaxation of gas/water interface.

Here we are concerned with a simpler question. Do the intrinsic properties of pure water such as density, surface tension, boiling point, and evaporation rate change in the presence of a static magnetic field? and if so why? A review of magnetic water treatment by Chibowski and Szcses [8] mentions persistent magnetic field effects to increase or decrease the surface tension [9-12], increase the viscosity [13], and change in pH and conductivity [14,15] besides enhancing the water evaporation rate [16], [10,17-20] , which is the focus of this chapter.

There have been three types of experiments, first are those where the weight of a certain quantity of water is measured as it is exposed to a static magnetic field *B* and compared to a no-field reference[10,20-22]. These usually involve interrupting the experiment after different lapses of time to weigh the evaporating water, which may be left at ambient temperature or heated in an oven[23]. Alternatively, the loss of weight by evaporation can be measured in zero field as different times, after a single exposure to a static field[24]. The field is usually produced by a permanent magnet, and it is not uniform in magnitude or direction over the surface of the evaporating water, which is contained in a beaker.

In the second type of experiment, the water is exposed to a nonuniform field, by continuous dynamic circulation at a velocity $\lesssim 1 ms^{-1}$ around a circuit where a permanent magnet surrounds a section of the pipe [21,25-27]. The experimental setup resembles that used for magnetic treatment of hard water to inhibit limescale formation, except that the water is circulated repeatedly through the inhomogeneous magnetic field, rather than just once. This type of treatment is equivalent to periodically exposing the water to a 20 – 50 ms magnetic field pulse at a frequency of about 1 Hz. After the circulation period, the magnetically-treated water is removed and its rate of evaporation is tracked by weighing at different time intervals. Remarkably, both types of experiments give qualitatively similar results. They have been combined in a two-stage experiment to increase the effect[28]. Exposure of water to a magnetic field of a few tens or hundreds of milli Tesla appears to significantly increase the subsequent

rate of evaporation. This means that the water retains a memory of its dynamic or static[24] magnetic treatment that persists for times of order an hour or more[20,28]. Various authors use different experimental protocols, and the results depend on temperature, humidity, magnetic field strength and time in different ways, so there is much inconsistency among their results. The reported increases in evaporation rate associated with the magnetic field range from a few percent to more than 30% [10,19,20,23,24,27,29]. The magnetic field is thought to modify, somehow, the network of molecular hydrogen bonding in water. There is no agreed explanation of how this occurs, but the direct increase in energy of a mole of water, with susceptibility $\chi_{mol}$ = -1.62 $\times 10^{-10}$ in a field[30] of 1 T is $-\frac{1}{2}\chi B^2/\mu_0$ = 65μJ/mol, compared with the energy of the water hydrogen bond in water, which is 23.3 kJ/mol [31], nine orders of magnitude greater. Effects of such weak fields on chemical reactions are usually associated with transitions between electronic or nuclear molecular singlet and triplet states. It has been suggested by Vaskyna et al. that the effects of magnetic water treatment are associated with the proportions of ortho and para isomers of $H_2O$, that have net nuclear spins $I = 1$ and $I = 0$, respectively, and an influence of magnetic field on their librational oscillations[32].

The third type of experiment is different. Here the water is exposed to a strong magnetic field in a superconducting solenoid, with a large horizontal field gradient $\nabla_x B$. The product $B\nabla_x B$ is 320 $T^2m^{-1}$ . In this case, the explanation is related to the paramagnetic susceptibility of oxygen in the atmosphere[16], which is displaced by the evaporating water vapour. The changes are 17 % of the buoyancy forces on air, which leads to a field-induced modification of convection and evaporation rate. Similar experiments have been conducted in a vertical field gradient sufficient to levitate a water droplet $B\nabla_z B \approx$ -1450 $T^2m^{-1}$, or double the effective gravitational force $B\nabla_z B \approx$ -2900 $T^2m^{-1}$. Buoyancy effects are again observed, and evaporation was found to be faster in microgravity[18].

In this work, we investigate the evaporation rate in a much smaller, quasi-uniform field. We have built an automated setup to monitor the evaporation of water and other aqueous solutions continuously, in real-time, comparing the evaporation rates in a magnetic field with

that of a no-field control for periods of up to 60 h, while recording continuously the temperature and humidity. We compare the effects on pure water with those on a salt solution and concentrated solutions of urea, where hydrogen bonding is disrupted by the solute. Results are discussed in terms of the possible effects of a magnetic field on the two isomers of water, which behave as quasi-independent gasses in the vapour phases. We have also used NMR, Raman and FTIR spectroscopy in an attempt to identify magnetic field effects on water.

## 3.2 Experimental methods

The experimental setup has two identical KERN Model EW-2200 Precision balances (2.2 kg capacity, 10 mg sensitivity) to monitor the weight of water or aqueous solution as it evaporates in a 100 mL beaker while exposed to a magnetic field and compare it to a no-field control. The beaker (ID: 46.80 mm, height: 70mm) was completely inside the bore of the magnet. The balances are side by side in closed polymethylmethacrylate (Perspex) box as shown in Fig.3.1. The mass of water is automatically recorded for periods of up to 16 h. No transfer of liquid is involved, just a real time record of the change of mass with and without a magnetic field. The horizontal magnetic field, parallel to the liquid surface, is produced by an 8-segment Nd-Fe-B Halbach ring magnet with inner and outer diameters of 130 mm and 330 mm, and height of 95 mm. The field is 487 mT at the centre of the bore. The in-plane field profile across the bore is shown in Fig. 3.2.a) and the profile of the field along the axis is shown in Fig 3.2b).

The beaker was centred in the magnet bore and the liquid surface was close to the middle of the magnet, The average field over the liquid surface was close to 500 mT. The beakers are raised 140 mm above the patens of the balances, and the magnet is mounted on a four-legged aluminium stand in a position where its magnetic field has no direct influence on the balance reading. Four thermocouples are suspended with one inside and one outside each beaker, and there is a temperature/humidity sensor in the Perspex box.

The readings from both the balances and the temperature and humidity sensors were collected with a TESTO 174H data logger and monitored in real-time using a specially written LabVIEW

code. Although there are small fluctuations in ambient temperature and changes in relative humidity that modify the evaporation rate over the course of a 16-hour run, the conditions are always similar for both the in-field liquid and the no-field control. The quantities of water used were 10, 20, 30 and 50 mL and for NaCl and Urea solutions the quantity was 50 mL. Experiments for each quantity of liquid were repeated 4 – 6 times on different days, including experiments where the balances were interchanged.

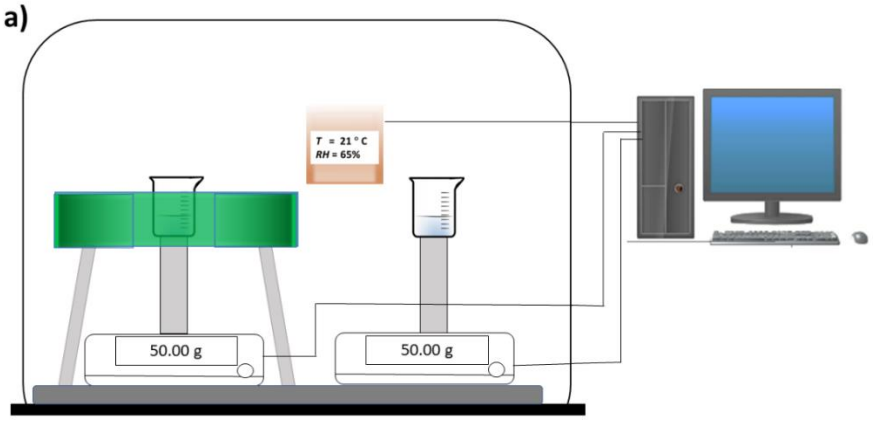


Figure 3. 1: Experimental evaporation setup. The water sample and the control are mounted on two identical balances in a Perspex box, and a 0.5 T magnetic field is applied to the sample using the Halbach ring magnet (blue)

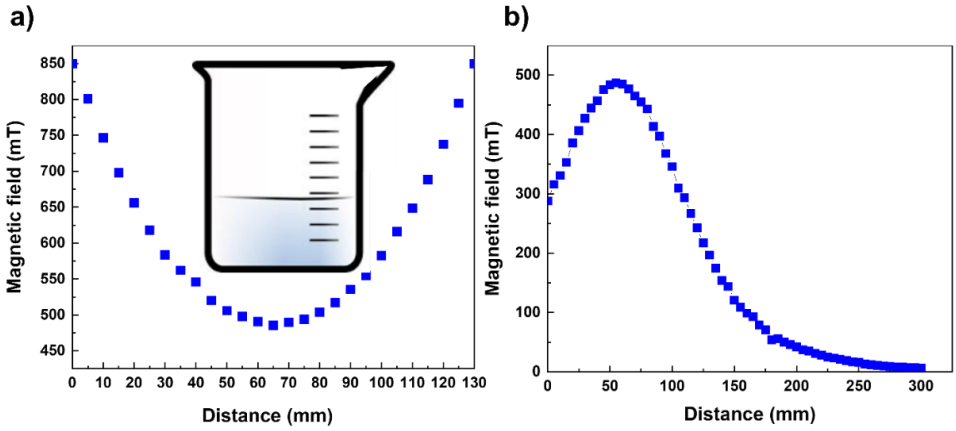


Figure 3. 2: The field profile inside the bore of the Halbach ring magnet a) across a central diameter and b) along the magnet axis

Table 1 gives details of the liquids investigated. Surface tension was measured using a Data Physics OCA25 droplet analyser

| Liquid | | Specific Gravity | Surface tension ($mNm^{-1}$) | pH | Conductivity ($Sm^{-1}$) | Boiling temperature (°C) |
|---|---|---|---|---|---|---|
| **Water** | Millipore 18.2 MΩ | 1.000 | 72.0 | 7.6 | 0.01 | 99.9 |
| **NaCl solution 99%** | 1.0 M | 1.058 | 74.8 | 5.3 | 20 | 102.2 |
| **Urea solution 99.9%** | 1.5 M | 1.020 | 72.6 | 7.3 | 0.01 | 101.3 |
| **Urea solution 99.9%** | 3.0 M | 1.045 | 74.2 | 7.7 | 0.01 | 102.5 |

## 3.3 Characterization Methods

The magnetic field effects on physical properties were measured using different spectrometry techniques which could give a detailed understanding of the effect in atomic and molecular level. Pang et al.[33]observed a change in infrared and ultraviolet absorptions, Raman scattering and X-ray diffraction of magnetized water relative to that of pure water. We investigated the magnetic field effects on water using FTIR, Raman and NMR.

Magnetic field effects on water have been studied in two ways, first by magnetizing the water sample before the measurement to test the memory effect of water and second, by instantaneous application of magnetic field while recording the spectrum. A tapered Halbach cylinder that produces a B∇B field has been used to magnetize water for varied time intervals. A 10 mm magnet cubes made of Nd-Fe-B with a remanence of 1.26 T that produces a surface field of 0.4 T has placed on the side of the water drop while recording the spectrum in Raman spectroscopy.

### 3.3.1 Fourier Transform Infra-Red Spectroscopy

Fourier Transform Infrared spectroscopy (FTIR) is the study of interactions between matter and electromagnetic fields in the infrared region. When infra-red (IR) radiation is passed through a sample, it absorbs radiation at frequencies similar to its molecular vibration frequencies and transmits other frequencies. An infrared spectrometer detects frequent radiation and plots the absorbed energy against frequency. FTIR uses the mathematical process (Fourier transform) to translate the raw data into an actual spectrum. IR spectroscopy is a powerful technique that provides fingerprint information on the sample's molecular composition.

FTIR is useful to identify functional groups that are IR active, molecules with a dipole moment. When IR radiation interacts with a covalent bond of a molecule with dipole moment, it induces a back-and-forth oscillation of the bond leading to an absorption of energy. A single atom or symmetrical molecules do not absorb IR radiation because of the absence of dipole moment.

The typical FTIR spectrometer consists of an IR light source, interferometer, sample compartment, detector, amplifier, and computer. The light source generates IR radiation which strikes the sample passing through the interferometer and reaches the detector. Then the signal is amplified and converted to digital signal (interferogram) by the amplifier and analog-to-digital converter, respectively. Eventually, the interferogram is translated to spectrum through the fast Fourier transform algorithm. Michelson interferometer is the main core of FTIR spectrometer.

The interferometer consists of a beam splitter, fixed mirror, and a moveable mirror that translates back and forth, very precisely. The beam splitter is made of a special material that transmits half of the radiation striking it and reflects the rest half of the radiation. Light from the source passes through a collimating mirror and beam splitter and splits into two beams at the beam splitter. One beam is transmitted to the fixed mirror, and the second to the moving mirror. The fixed and moving mirrors reflect the radiation back to the beam splitter. Accordingly, both of these reflected radiations are recombined at the beam splitter, resulting in one beam that leaves the interferometer and interacts with the sample and strikes the detector,

as shown in Fig. 3.3. Perkin Elmer FTIR 100 Attenuated total reflectance (ATR) spectrometer has been used to record the spectrum of the magnetized water.

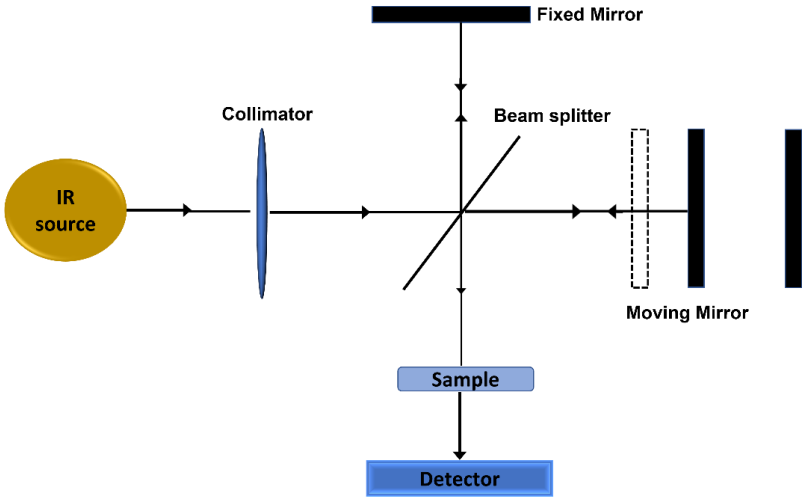


Figure 3. 3: Schematic of FTIR spectroscopy instrumentation

## 3.3.2 Raman Spectroscopy

Raman spectroscopy is another commonly used vibrational spectroscopic method to access the molecular motions and fingerprint the chemical species in a sample. Raman spectroscopy is based on the in-elastic scattering of photons, known as Raman scattering. When a monochromatic light interacts with the molecular vibration, its energy gets shifted up or down. This shift in energy gives information about the vibrational modes of the molecules.

When photons undergo collisions with molecules that are perfectly elastic, they will be deflected with energy unchanged. If the molecule gains energy $\Delta E$, the photon will be scattered with energy ($h\nu-\Delta E$) and the equivalent radiation will have a frequency ($\nu-\Delta E/h$). If the molecule loses energy $\Delta E$, the scattered frequency will be ($\nu+\Delta E/h$). Radiation scattered with a frequency lower than that of incident beam is referred to as Stokes Raman scattering, while that at higher frequency is called anti-Stokes Raman Scattering as given in figure 3.4 b). Stokes Raman scattering is generally more intense than anti-Stokes Raman scattering.

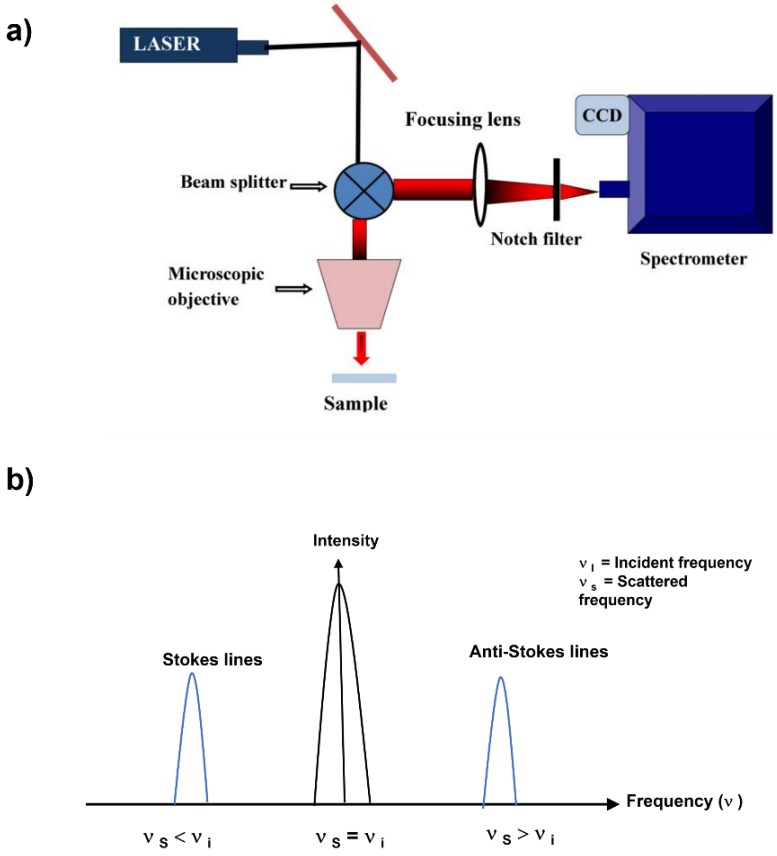


Figure 3. 4: a) Schematics of Raman spectroscopy instrumentation, b) Stokes and anti-stokes sidebands

Raman spectrometer consists of a laser source, beam splitter, microscopic objective lens, focusing lens, notch filter, spectrometer and a charged coupled device (CCD) as shown in figure 3.4 a). A highly collimated laser beam is focused to a particular point on the sample using a microscope. A part of laser light is passed onto the spectrometer and the other is passed onto the sample. The light scattered from the sample is recorded using a CCD camera. Elastic scattered radiation and Anti-stokes line is filtered by the notch filter and Stokes lines of the Raman spectra are recorded.

### 3.3.3 Nuclear Magnetic resonance

Nuclear Magnetic Resonance (NMR) is a non-invasive, non-destructive atom/isotope selective method which provides information on a microscopic scale. In NMR, the nuclei are subject to a strong magnetic field $B_0$ has two effects on the nuclear magnetic moments. The first effect is to cause the moments to precess with a frequency $\nu_0$ about the direction of $B_0$ as shown in Figure 3.5(a).

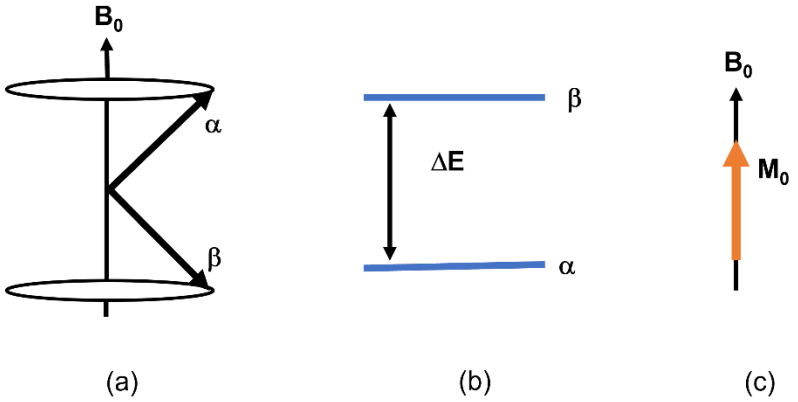


Figure 3. 5: (a) The two spin states α and β, of a nucleus with I = 1. (b) The energy levels of a nucleus with I = 1. (c) The total nuclear magnetization at thermal equilibrium ($M_0$) in a magnetic field $B_0$

The second effect of $B_0$ is to lift the degeneracy of the spin states. At thermal equilibrium, the precession phases of the nuclei are random but there is an excess of spins in the lower energy state, so the bulk or total nuclear magnetic moment, denoted $M_0$, lies along $B_0$, as shown in Figure 3.5 (c). To obtain an NMR spectrum, the nuclei are subjected to a second small magnetic field, denoted $B_1$, which is oriented perpendicular to $B_0$ and which oscillates at a frequency at or near $\nu_0$ which is demonstrated in figure 3.6. The $B_1$ field when applied at the resonance frequency, slightly rotates the net magnetization $M_0$ away from the $B_0$ direction thus inducing a component transverse to $B_0$ which precesses about Bo at the frequency $\nu_0$ at the same time relaxing back to the equilibrium state of figure 3.5(c).

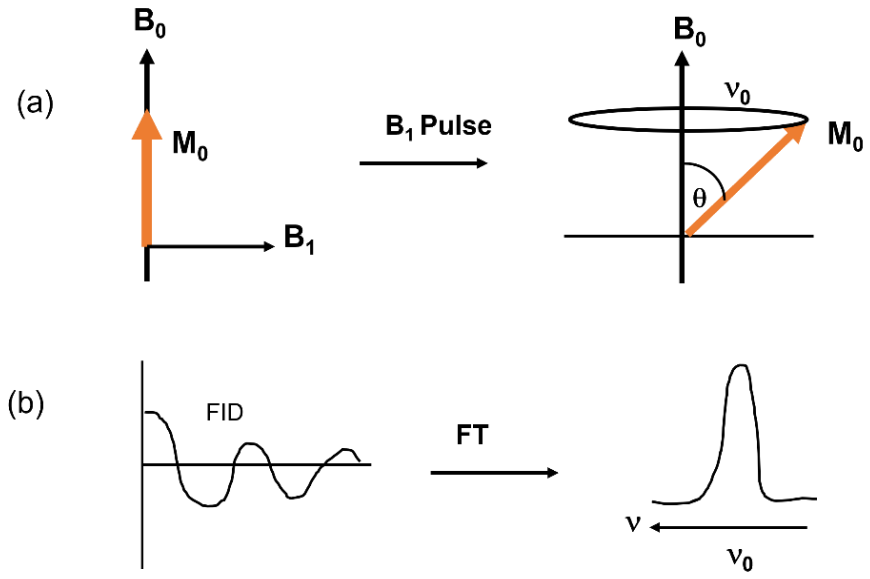


Figure 3. 6: (a) The action of a magnetic field $B_1$ on the total nuclear magnetization $M_0$ and the precession around $B_0$. ($\theta$ is the flip angle and $\nu_0$ is the precessional frequency. (b) The time-based free induction decay (FID) resulting from detection of the precessing transverse component of the nuclear magnetization after a pulse, and its Fourier transform to give the frequency sweep spectrum

The resonance frequency depends on the chemical environment of the nucleus. The greater the electron density around a proton, the weaker the effective field it experiences (shielded) resulting in lower frequency transitions. Thus, a higher magnetic field has to be applied to achieve resonance. The electron cloud generates a small, induced field in response to the applied field $B_0$, thus shielding or screening the nucleus from $B_0$. The shielding field is proportional to $B_0$. The variation of $\nu_0$ with the chemical nature is known as the chemical shift. Bruker Avance II 600 NMR has been used to record the proton NMR spectrum of magnetized water that has been exposed to a B∇B field.

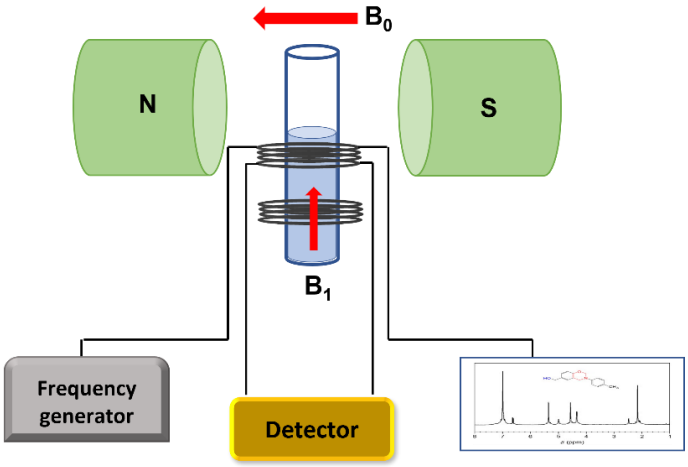


Figure 3. 7: Instrumentation of *NMR* spectrometer

## 3.4 Results and Discussion

### 3.4.1 Evaporation

Besides magnetic field, the subject of our investigation, the evaporation rates of water and aqueous solution depend on temperature, humidity and airflow. Convection at the liquid surface is limited by the Perspex enclosure and the walls of the beaker and the magnet. Temperature and humidity are not controlled, but they are monitored over the 16 h – 60 h duration of each run. Figure 3.8 shows the reduced mass of different volumes of water, 10, 20 and 50 mL, comparing the reference with no magnetic field (black lines) to the water in the magnet (red lines). The evaporation rate has been calculated using Eqn.2.

$$\text{Reduced mass} = M_t/M_0 \quad (1)$$

$$\text{Evaporation} = \Delta M / (A*t)\ \text{kgm}^{-2}\text{h}^{-1} \quad (2)$$

$\Delta M = M_t - M_0$

A = area of the beaker

t = total time of the experiment

The average magnetic field over the surface is similar in the three cases, 505 mT, 505 mT and 495 mT, respectively, and the maximum magnetic field gradient at the surface is 3 $Tm^{-1}$. In the course of these experiments, the evaporation rate fluctuated by 10 % or more because of slow variations of ~ 1 ℃ in temperature and ~ 5% in relative humidity.

The plot in figure 3.8 d) shows that the percentage weight loss after 16 hours varies as the inverse of the mass of the sample, and the rate of evaporation of water is enhanced by 8 ± 2 % in the magnetic field. The proportionality of mass loss to inverse sample mass means that the evaporation is a surface effect, proportional to the surface area exposed to the magnetic field. The evaporation rate is 0.0293 $kgm^{-2}h^{-1}$ without field and 0.0330 $kgm^{-2}h^{1}$ in the 500 mT field.

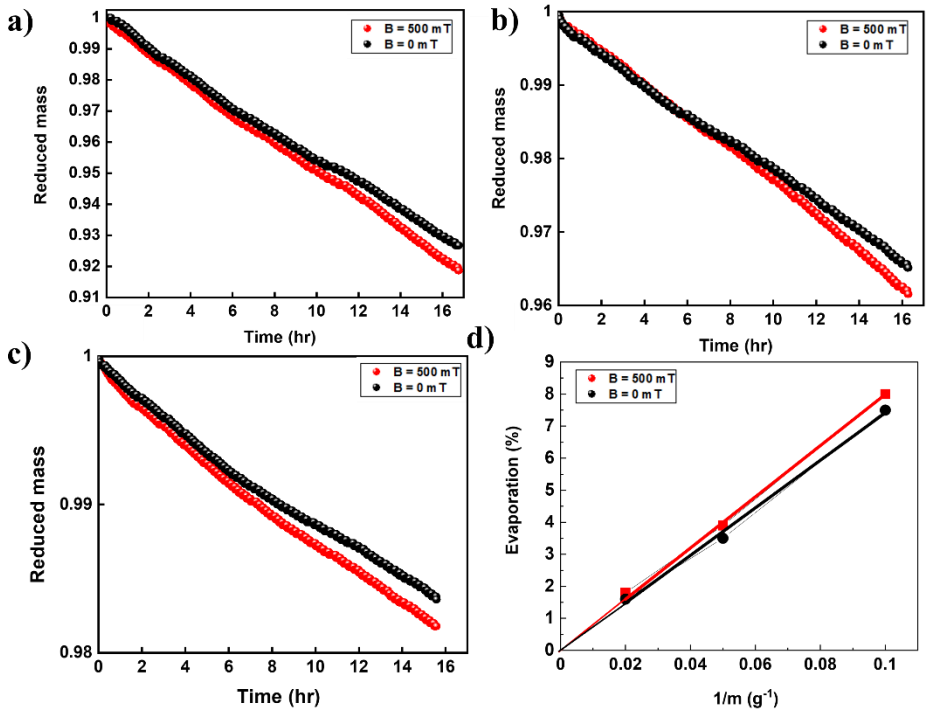


Figure 3. 8: Relative weight loss by evaporation of water in a 500 mT magnetic field parallel to the surface (red lines) and a reference with no magnetic field (black lines). The initial masses are 10 g (a), 20 g (b) and 50 g (c). The fourth panel plots the weight loss as a function of inverse sample mass showing the effect scales with surface area, and the weight loss is 8 % faster in the magnetic field.

In figure 3.9, we show data for 30 mL of water and 50 mL of 1M NaCl and 6M Urea in runs where the evaporation rate remained almost constant over the course of the 16 hour experiments, due to smaller fluctuations in ambient temperature and relative humidity, or correlated and opposite drifts in these uncontrolled variables. In figure 3.9 a) for 30 mL water, the increase in evaporation rate in the field is 19%, but the effect on the 50 mL 1 M and NaCl and 6M urea solutions in Fig 3.9 c) and e) is quite different. The evaporation is inhibited by the magnetic field, being reduced by 23% and 28% respectively. In three runs the zero-field evaporation rates are 0.0445. 0.0335 and 0.0425 $kgm^{-2}h^{-1}$respectively, and the temperature and humidity variations are illustrated in the left-hand side of the panels in figure 3.9.

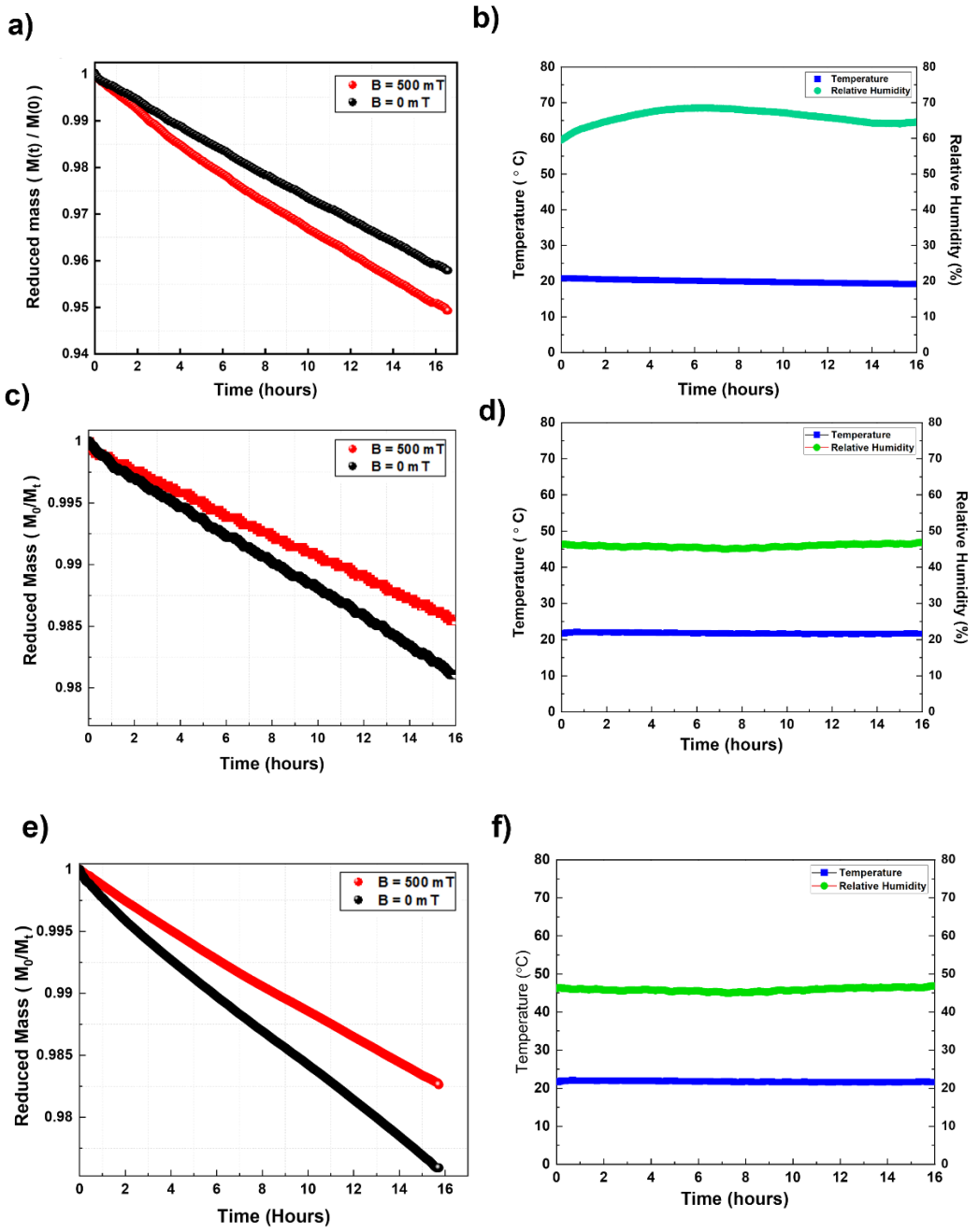


Figure 3. 9 : Relative weight loss by evaporation in runs where only minor fluctuations of temperature and humidity over 16 h a) 30 mL water, c) 50 mL 1M NaCl and e) 50 mL 6 M Urea. Black lines are for reference samples, red lines for samples exposed to a 500 mT magnetic field. Panels b), d) and f) shows the corresponding temperature and relative humidity during the runs.

We have also analyzed extended runs where the evaporation of 50 mL of water was monitored over a period of 60 hours. The ambient temperature and humidity fluctuated over the run, as illustrated in Fig. 3.10, but the evaporation rate of the sample in the magnetic field was hardly ever less than that of the reference. At the end of the experiment, the time-averaged weight loss in the magnetic field was 15% greater than that of the reference.

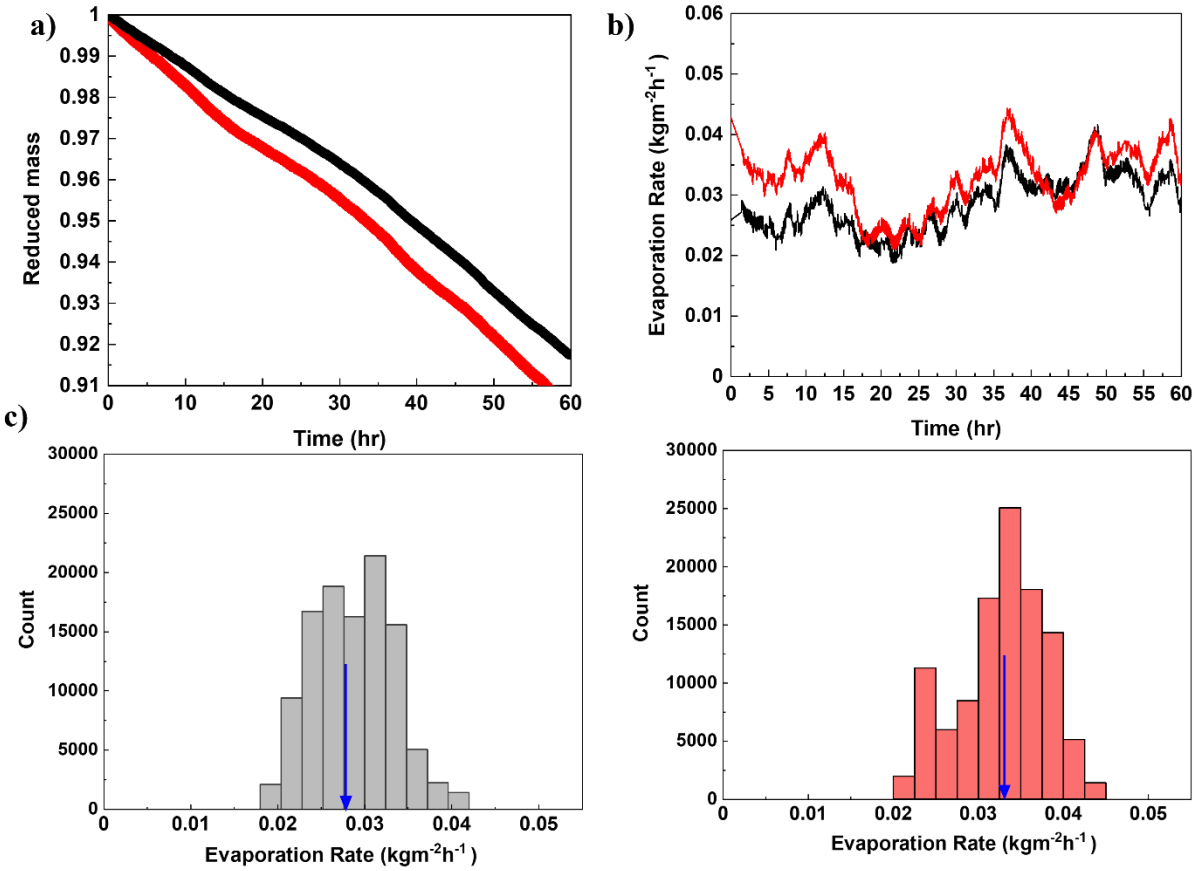


Figure 3. 10: Extended 60 h run of evaporation versus time for a 50 mL water sample in 500 mT(red) and the no-field reference (black). a) relative weight loss by evaporation b) evaporation rates versus time and c) histograms of the evaporation rates (reduced mass loss per hour), where the average values are marked

The temperature of the evaporating water was found to increase by about 1°C in the course of a 16 hour run, and the temperature change for the samples in the magnetic field was slightly (~0.1 1°C) higher, Fig. 3.11, but this does not explain the difference in evaporation rate.

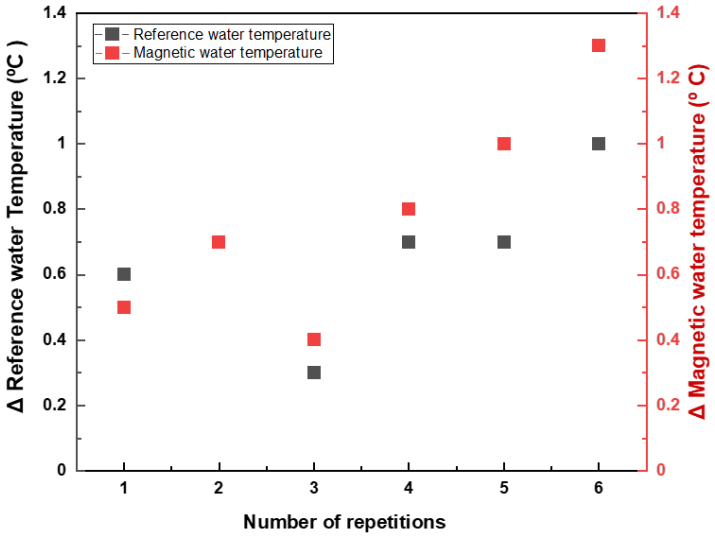


Figure 3. 11: Difference of change of temperature in the course of 16 h runs between in-field and zero field water. The average over 6 runs in only 0.1 °C.

Shorter-term two-hour runs were carried out to follow the initial minutes of evaporation after pouring the deionized water or urea solution into a beaker in a closed balance. Typical results are illustrated in Figure 3.12. Evaporation in zero field is fastest in the first few minutes for water and it then settles down to less than half the initial rate after about half an hour. The urea solution is quite different. The initial evaporation is very slow, and it becomes three times faster after the initial transient. The data were fitted to the function

$$m(t) = m_0 e^{-t/to} + m_1( 1- g_1 t). \qquad (3)$$

The time constant of the initial exponential transient, when the water vapour in the air in contact with the water surface has the equilibrium 3:1 ortho/para ratio, is $t_o$ = 9 min. At longer times the isomeric ratio will approach that of the freshly-evaporated water. The average of eight one-hour runs for water gave an initial evaporation rate of 0.134 ± 0.030 and an average $t_o$ of 14 ± 3 min.

The long-time evaporation rate is 0.068 ± 0.010 kg/m$^2$/hr. The average of five one-hour runs for urea gave an initial evaporation rate that was more than ten times slower than that of water, while the difference in long-time evaporation rate was much smaller, although evaporation of urea was still slower than water in conditions of comparable humidity (Table 5). The decay time of the initial transient was $t_0$ = 62 min much longer than for water, so the 'steady' decay times from the one-hour runs are underestimates.

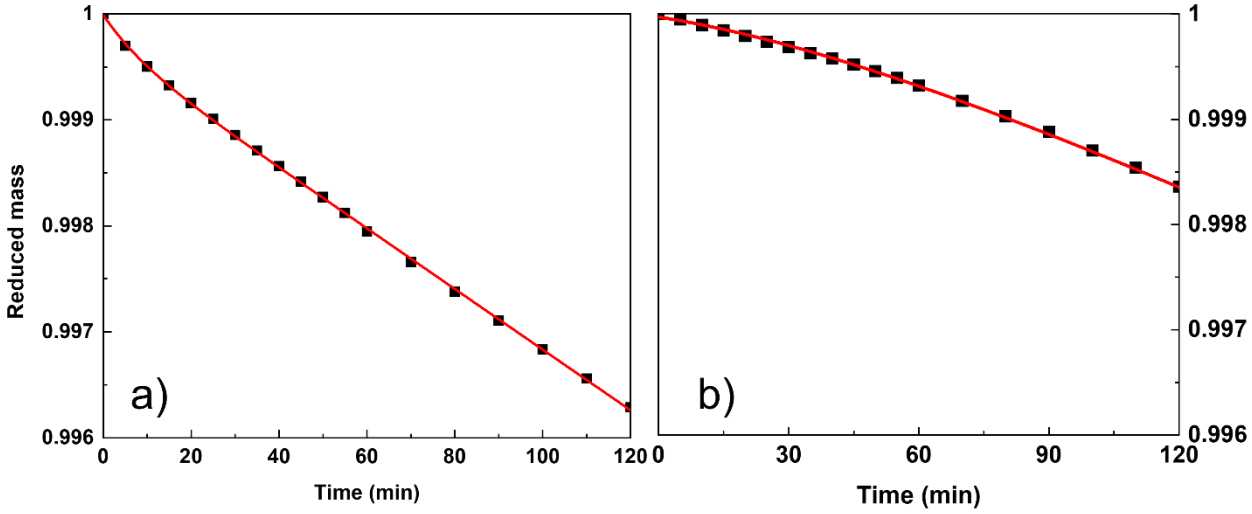


Figure 3.12. a) Short-term evaporation of Millipore water (a) and Urea solution (b) in stagnant conditions, showing the steady-state and initial transient regimes. The transient, which decays exponentially with a time constant of 9 min for water and 62 min for urea has opposite signs in the two cases.

The evaporation rate is very sensitive to the ambient relative humidity. Although we did not control it, the value was mostly in the range 60% – 70%. On some days it was quite steady over a 16-hour period, but on others it changed by 5% - 20% in the course of a run, with a corresponding change in evaporation rate. We make use of those data to plot the of change of evaporation rate $\Delta g$ versus the change in relative humidity $\Delta RH$ in Figure 7. The variation of $g$ with $RH$ is nonlinear. The fitted slope in Fig. 3.13 is -2.2.

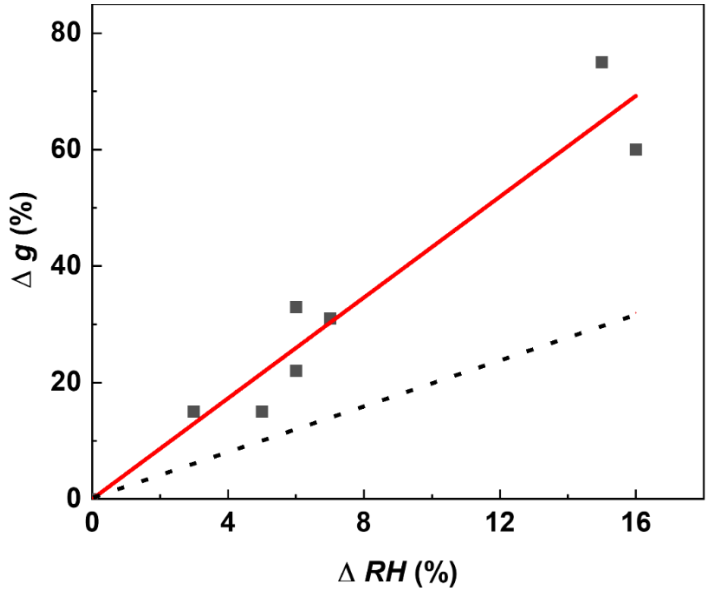


Figure 3.13. Variation of evaporation rate g with relative humidity *RH*, plotted as change of *g* versus change of *RH*. The dashed line with slope 1.0 would be expected for a linear relation between these quantities.

A final experiment has been conducted in an OCA 25 droplet analyser to find out if there is any change of surface tension when Millipore water with 18.2 MΩ.cm resistivity is exposed to a 450 mT field. The result of 37 measurements was that the mean increase of the surface tension of water was barely significant, 0.19 ± 0.21 $mNm^{-1}$, a result that is consistent with previous work in a similar magnetic field[11], and not inconsistent with the increase of 1.31 $mNm^{-1}$ found in 10 T [9].

Table 2 Summary of average evaporation rates and relative humidity.

| | Evaporation rate ($kgm^{-2}h^{-1}$) B = 500 mT | Evaporation rate ($kgm^{-2}h^{-1}$) B = 0 | *RH* (%) |
|---|---|---|---|
| Water | 0.0301 | 0.0274 | 72 |
| 6 M urea | 0.0321 | 0.0391 | 65 |

Table 3 Initial and steady-state evaporation rates, initial decay time, temperature and relative humidity in no applied magnetic field (data in Fig.6).

| | Initial evaporation rate ($kgm^{-2}h^{-1}$) | Decay time (minutes) | Steady evaporation rate ($kgm^{-2}h^{-1}$) | *T* ($^oC$) | *RH* (%) |
|---|---|---|---|---|---|
| Water | 0.1360 | 9 | 0.0452 | 24 | 60 |
| 6 M urea | 0.0166 | 62 | 0.0310 | 24 | 60 |

The concept of magnetic memory [7,25,34] of water has been tested by exposing water to a uniform magnetic field for 5 hours. The reference water and the water exposed to the magnetic field were kept inside the perspex box without any magnet and monitored the evaporation for 16 hours. We have also tested the magnetic memory on 6M urea solutions since the evaporation of urea solution was slower than water from our experimental observation. Evaporation of reference water and water exposed to the magnetic field did not show any significant difference in evaporation, as shown in Fig.3.14a). However, urea solution exposed to magnetic field showed a small but slower evaporation rate than reference solution as shown in Fig. 3.14b).

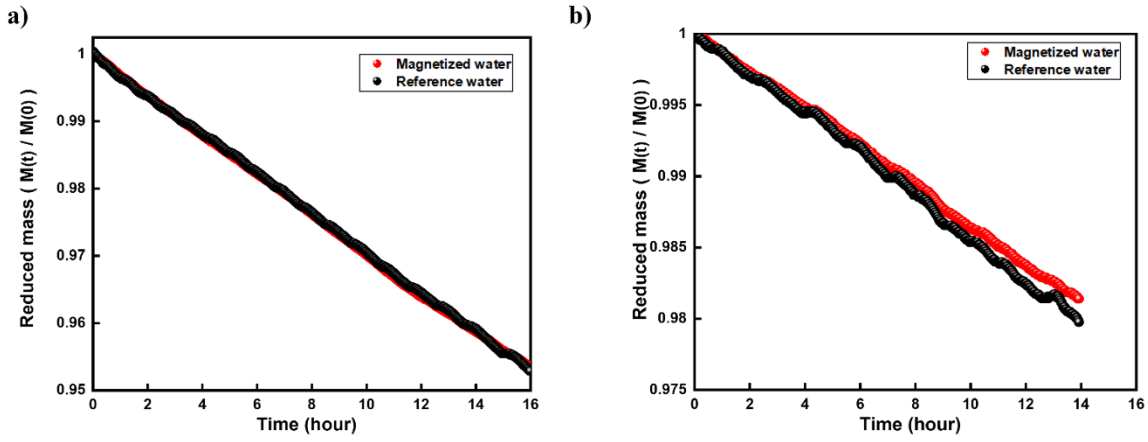


Figure 3.14: The magnetic memory of water tested by exposing magnetic field for 5 hours and then measured the evaporation for 16 hours a) water and b) 6M urea

Ours is the first study where the effect of a uniform magnetic field on the evaporation rate of water or urea solution has been monitored over long periods simultaneously for an in-field sample and a no-field reference. Ambient laboratory temperature *T* and relative humidity *RH*, which were monitored throughout, are the same for the in-field and no-field samples in each run. Evaporation rates increase with temperature and decrease sharply with relative humidity. There are also some uncontrolled fluctuations in the beakers, despite the long duration of our measurements, probably due to inevitable variations in surface airflow related to convection as water vapor evaporates and condenses at the water/air interface. Differences are observed between different measurement campaigns and even when the experimental setup was moved to a different place in the laboratory. Nevertheless, it is clear that there is an increase in the net evaporation rate of water of about 12% in the field, and a decrease in the net evaporation rate the urea solution that is at least as large. A table with details of all the 16 and 60 hour runs is provided in the Appendix A. Furthermore, we have found significant differences in the transient and longer term evaporation of both water and urea. These are the data we seek to explain.

A commonly-used empirical formula used by engineers that relates the net evaporation rate of water from a free surface in $\mathrm{kgm^{-2}h^{-1}}$ to relative humidity *RH* and the temperature-dependent capacity $x_s$ of dry air to absorb water vapour is [35]

$$g = \Theta x_s(1 - RH) \qquad (4)$$

where $x_s$ is plotted in Fig. 3.15. The prefactor $\Theta$ is $(25 + 17v)$ where $v$ is the speed of the surface airflow in $\mathrm{ms^{-1}}$. The numerical factors actually have dimensions $\mathrm{kgm^{-2}h^{-1}}$ (25) and $\mathrm{kgm^{-3}} \times 3600$ (17). According to this formula, the anticipated evaporation rate from a free water surface in still air, $v = 0$, at $T = 22$ ℃ and $RH = 70\%$ is 0.150 $\mathrm{kgm^{-2}h^{-1}}$. The evaporation rate increases by 10% whenever the temperature increases by 1.6 ℃, the *RH* decreases by 5% or the surface air speed increases by 15 $\mathrm{cms^{-1}}$.

The initial no-field evaporation rate of water from the surface of the partly-filled 100 mL beakers was 0.136 ± 0.045, close to that predicted by Eq. 4 with $\Theta = 25$, but it fell back to

about a third of the initial rate value after about 15 minutes, as shown in Figure 3.12 and Table 3, Figure 3.16 gives evaporation rates based on final weight loss for 16 hour runs where the temperature of 20.8 – 23.0 ℃ and $RH$ of 54 – 79% remained fairly constant. Humidity is an important variable, particularly since the data in Fig. 3.13 showed that a 5% change in relative humidity produces a 21 % change in evaporation rate, not the 10% change predicted by Eq 4. The relation between evaporation rate and relative humidity is quadratic, not linear. The considerable scatter of the data in Fig. 3.16 can be ascribed to differences in humidity and temperature as well as uncontrolled local convection at the surface of the water between runs. The slope of the lines here are $\Theta = 5.57 \pm 0.24$ kgm$^{-2}$h$^{-1}$ in zero field and $\Theta = 5.01 \pm 0.27$ kgm$^{-2}$h$^{-1}$ in 500 mT.

The average increase of 11 - 12 % in the evaporation rate of water in the magnetic field cannot be attributed to change of temperature in the course of a run; the average temperature difference between the magnetic and reference water was 0.1 K, and in no case did it exceed 0.3 K in any run (Fig. 3.11). The mass of water vapour, 10g/kg present in the 0.182 m$^3$ Perspex enclosure is 1.82 g, which is the amount produced by the water in the two beakers in 21 h. By the end of a 16 h run, much of the water vapour in the enclosure has been generated from the beakers. There was no evident trend of increasing relative humidity in the enclosure during a run, because it is not hermetically sealed and it exchanges air with the ambient atmosphere in the laboratory .

The evaporation rates of water from filled circular vessels of different diameters including one similar to our beakers, were studied by Hisatake et al[36,37] in a fixed airflow. They found that rates in an airflow of 90 cms$^{-1}$ are roughly double the ones we find for our 50 g samples in partly filled beakers where the water vapour escaping from the surface is not blown away.

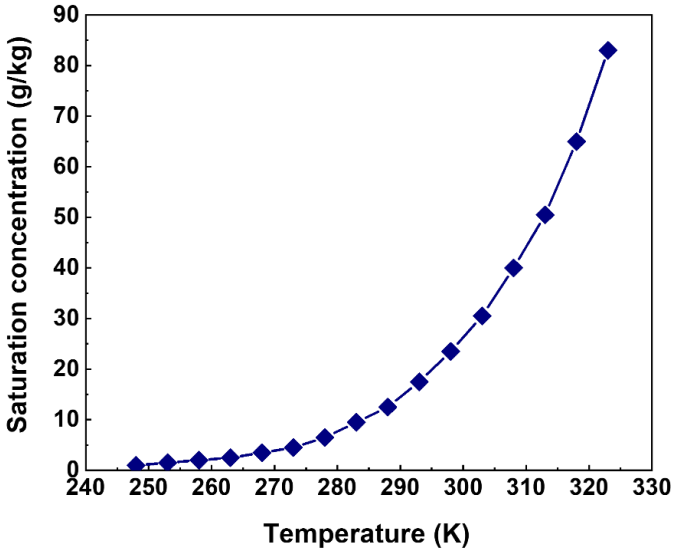


Figure 3.15. The saturation concentration of water vapour in air $x_s$ as a function of temperature [35].

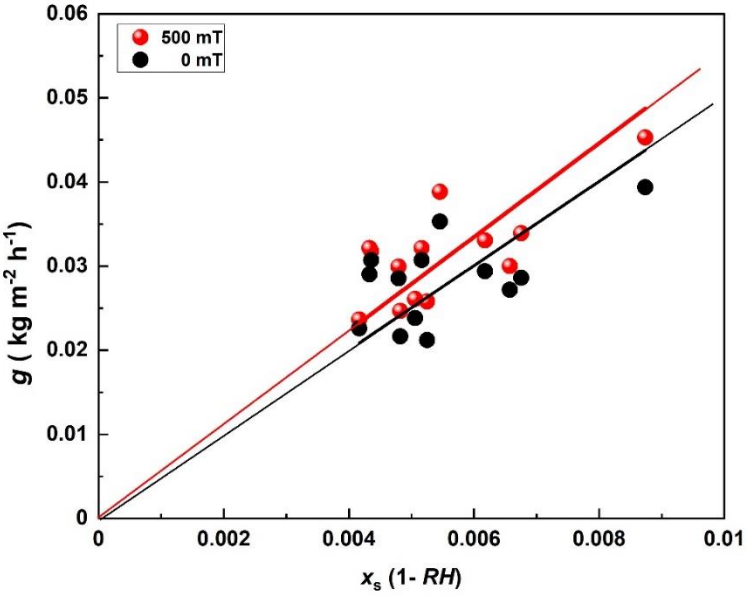


Figure 3.16. Evaporation rate of water from beakers containing 50 g of water was measured at temperatures in the range 20.8 – 23.0 ℃ and *RH* of 56 – 79 % with or without a magnetic field. The scatter in the data is attributed to uncontrolled surface convection and a strong dependence on relative humidity.

The relatively small, steady evaporation rates we find in the beakers after an initial transient are attributed to the build-up of vapour that has a ortho/para isomeric ratio close to that of the vapour escaping from the liquid, rather than the equilibrium 3:1 ratio that was there in the ambient air at the beginning. The time taken to evaporate a volume of fresh water vapour to replace that originally in the beaker airspace is about 20 minutes, so in the extended runs vapour evaporating from the liquid surface with an isomeric ratio $f_L{}^o$: $f_L{}^p$ is expected to have the same isomeric ratio as the vapour in the beaker $f_V{}^o$: $f_V{}^p$, except at the beginning of the extended runs. Here p and o denote the para and ortho isomers and L and V denote freshly-evaporated vapour and the ambient vapour near the interface in the airspace. $f$ is the fraction of each isomer and $f^o + f^p = 1$ in any vapour.

We now propose an explanation of our data that treats the two nuclear isomers of water vapour as independent gasses. The properties of the nuclear isomers of diatomic hydrogen gas $H_2$ are well known [38]. Para-hydrogen with $I = 0$ is the more stable of the two. The $I = 1$ ground state of ortho-hydrogen has a quantum of rotational angular momentum, and lies 15.1 meV (175 K) higher in energy. It is possible to separate almost pure para-hydrogen gas at low temperature, although at room temperature the equilibrium ortho/para ratio is close to 3:1, reflecting the three-fold nuclear spin degeneracy of the $I = 1$ triplet. Interconversion between the two isomers is extremely slow in the gas phase, and non-equilibrium concentrations may persist in hydrogen for weeks.

Likewise there are two isomers of water, ortho-water with $I = 1$ and para-water with $I = 0$ [39]. The ground state of ortho-water lies 35 K higher in energy. Relatively little is known about the difference in properties of the two isomers of liquid water. They were first identified by absorption onto charcoal surfaces, where unexpectedly long lifetimes of 26 and 55 minutes were reported [39,40], but these results were controversial [41]. Subsequently, Horke et al [42] produced pure beams of para- and ortho-water, and separated picolitre-scale volumes of each in a strong electric field. However, the separate molecular isomers will be much more stable in the gas phase, with little tendency to interconvert. The equilibrium 3:1 ratio will eventually be

established by collisions after a period of many days, depending on vapour pressure. For our purposes, we will regard them as independent gasses, each with its own vapour pressure. It is thought that the ortho/para ratio in liquid water and the solutions we investigated may be far from the equilibrium value due to hydrogen bond formation [39]. The ratio has been investigated by four-wave mixing experiments [43], [44], terahertz spectroscopy [45] [46], nuclear magnetic resonance [44] and electrochemical impedance spectroscopy [47]. The ortho/para ratio can be enriched in water that has undergone ultrasonic cavitation relative to its value in liquid water [44] where the value is thought to be close to 1:1[43]. There are important implications of the ortho/para ratio for hydrogen bonding and the structure of water, as well as biological [43], physiological and climatic consequences [48]. The para isomer, with no rotational angular momentum in the ground state, was reported to adhere preferentially to solid surfaces [42].

The saturation concentration of water vapour $x_s$ shown in Fig. 3.15, will be practically independent of the isomer involved but, when the two isomers behave as distinct gasses, the evaporation of each one is limited by its own partial pressure in the ambient air. The evaporation rate depends on the product of an escape probability related to the concentration of the isomer in the liquid, and a factor depending on the unsaturated vapour pressure of the escaping isomer in the ambient air in the beaker. If the ortho/para ratio for the molecules *escaping* from the water is $f_L$:(1-$f_L$) and $f_V$:(1-$f_V$) for the molecules in the vapour in the beaker, then we should consider a sum of the two independent fluxes of ortho and para vapour, which we do by introducing the dimensionless factor $\gamma$ in square brackets in equation 5.

$$g' = \Theta x_s (1 - RH)[f_L^{\,0}(1\text{-}f_V^{\,0}) + f_L^{\,p}(1\text{-}f_V^{\,p})] \qquad (5)$$

We consider two limits. One is the case when the water is evaporating into normal 3:1vapour from the atmosphere at the beginning of a run. The other is when the beaker is filled with vapour of the same isomeric composition as that released from the surface of the liquid itself. In the first case,

$$\gamma = 1 - f_L^0 f_V^0 - f_L^p f_V^p \quad (6)$$

Writing this in terms of the otho isomer, using $f_{L/V}^p = 1 - f_{L/V}^o$, and setting $f_V^o = 0.75$, we find the linear relation shown by the red line in Fig. 3.17.

$$\gamma = 0.75 - f_L^0 f_V^0 \quad (7)$$

In the second case $f_L^0 = f_V^0$, and Eq 6 reduces to

$$\gamma = 2 f_L^0 (1 - f_L^0), \quad (8)$$

shown by the green parabola in the same figure. The evaporation rates in the two cases are proportional to $\gamma$, read off the figure for a given value of $f_L^0$. When the initial evaporation rate is greater than it is in the steady state, as in the case in pure water, the isomeric composition of the vapour released $f_L^0$ must lie in zone $A_1$ or zone $A_2$. When the converse is true, as in 6 M urea solution, $f_L^0$ must lie in zone B. To progress further with our model, and reproduce numerical ratios of the red and green evaporation rates, we have to bring condensation into the picture[49,50]. Equation (3) describes the *net* rate, evaporation less condensation. Equation (4) describes the two-gas evaporation. To model condensation, we will simply assume a constant value c independent of $f_L^0$ and add -c to the right hand side of Eq 6 and Eq 7. The value of *c* is indicated by the horizontal dashed line in the figure, which is the baseline from which we measure the net evaporation rate For water, we can reproduce the values in Table 3 for values of $1.05 < c < 0.45$ in zone $A_1$ and $0.1<c<0.2$ in zone $A_2$. For Urea, the limits are much narrower $0.40 < c < 0.45$. If we further require that c and the equilibrium evaporation rate is similar in the two cases, we can narrow down the ranges of $f_L^0$ to $0.39\pm0.01$ in water and $0.60 \pm 0.05$ in 6M urea.

The urea molecule is hydrogen bonded to five surrounding water molecules in the solvation structure of urea. One of the water molecules shares two hydrogen bonds with the urea. Concentrated solutions of urea (6 M urea is 36 % urea by weight) poses a constraint to rotational dynamics of the water molecules in the solution [51], which might influence the equilibrium fraction of ortho-water, and the nature of the escaping molecules. Urea itself has a very low vapour pressure, and does not evaporate significantly at ambient temperature.

We emphasise that the ratios we measure are not necessarily the ratios present within the liquids. Water molecules are ejected in a process that involves the coordinated making and breaking of hydrogen bonds of at least three molecules at the interface to provide the 10 -12 $k_B T$ of energy needed for one molecule to break a hydrogen bond and escape [52]. The high energy of the escaping molecule, ~ 3000 K, may tend to thermalize the isomer ratio. It is unclear exactly what fraction of ortho water is present in the liquid, but in pure water it seems likely that $f_L^0 < 0.5$.

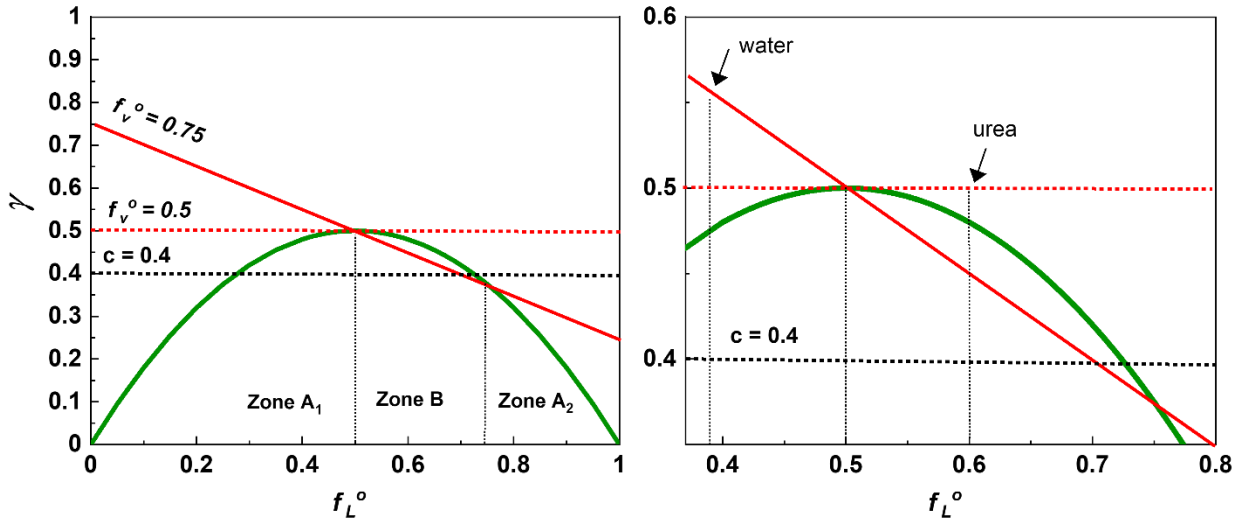


Figure 3.17: Normalized evaporation rates of water as a function of the ortho fraction $f_L^0$ present in the vapour escaping for the liquid for two cases. The red curve is for $f_V^0$ – 0.75, the natural 3:1 ratio in the atmosphere. The green curve is for $f_V^o = f_V^p$, when the evaporating liquid is surrounds by its own vapour. The isomeric ratios deduced from our data on pure water and 6M urea solution are marked (See text for details)

Finally, we consider two ways, illustrated in Fig. 3.18, whereby a magnetic field might modify $f_V^o$ at room temperature and thereby influence the evaporation rate. One possibility is via Larmor precession of the two hydrogen nuclei in a water molecule. Another is via Lorentz

stress on the electric dipole moment of water. Protons precess at a frequency of 43 MHz/T, or 22 MHz in our 500 mT field. The small field gradient ~ 3 $Tm^{-1}$ near the edge of the beaker means that the precession frequencies for the two protons separated by 0.27 nm differ by about 1 part in $10^{10}$. The time taken for their precession to dephase by $\pi/2$ is 7 s, during which time the molecule will have travelled 4.4 km at an average speed of 630 $ms^{-1}$ and undergone N = $4.4 \times 10^{10}$ collisions if the mean free path is $\lambda$ = 100 nm. In the 7s, the randomly-scattered molecule will have only drifted a distance of approximately $\sqrt{(N/3)}\ \lambda$ = or 1.2 cm away from the liquid surface, while remaining in the beaker. Collisions do not influence the Larmor precession, which is independent of the orientation of the protons relative to the magnetic field. If the effect of the Larmor spin flips is to equalize the populations of the two isomers in the vapour, and the composition of the vapour $f_V$ is the same as that of the molecules escaping from the water $f_L$ in the absence of a field, the evaporation rate will always be enhanced by the field, because the green curve always lies below the dashed red line plotted $f_V^0 = f_V^0 = 0.5$.

Lorentz stress arises because the water molecule has a dipole moment p = $6.2 \times 10^{-30}$ Cm, The force on the moving electronic charge will tend to reduce the 105° bond angle. The torque on the molecule p*B*v is equal to the rate of change of angular momentum, d*l*/dt. A quantum of angular momentum is transferred to the water molecule in a time $\hbar/pvB = 5.4 \times 10^{-8}$ s. However, in that time the molecule undergoes on average 2400 collisions. Unlike Larmor precession, which is independent of the direction of travel of the protons and their orentation relative to the field, these contributions add statically and ~ 20 s will be required to add or subtract from the quantized angular momentum of the molecule, The tendency however will be to increase the ortho population, and in this case it is possible to diminish the evaporation rate in the field (Fig. 10), provided the composition lies in zone B, as is the case for the urea solution. The Larmor precession cannot explain the different signs of the field effects on evaporaton, the Lorentz torque could.

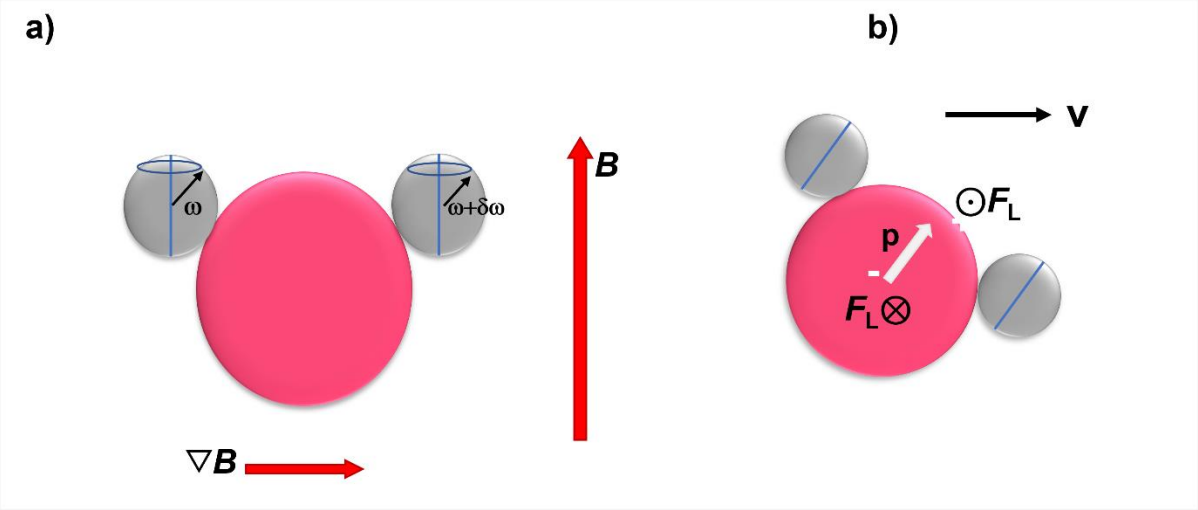


Figure 3.18. Modification of the angular momentum of a water molecule a) by dephasing of proton precession in a magnetic field gradient and b) by Lorentz torque due to motion of the charge dipole across the magnetic field

## 3.4.2 FTIR and Raman spectroscopy

The infrared absorption spectra of water magnetized for 2 hours are shown in Fig.3.19. The main absorption peaks of water, H-O-H bend and O-H stretch did not show any difference in magnetic field. Reference water 1 and 2 lie on top of magnetized water in Fig.3.19 a). A special feature has been observed at 2350 $cm^{-1}$ for magnetized water, shown in figure 3.19 a) marked in red. The zoomed version of the marked part of the spectrum is shown on the right panel in figure 3.19.

The experiment has been repeated several times to understand the appearance of the new special feature for magnetized water. The special feature appeared for both reference water and magnetized water given in figure 3.20 a). The FTIR spectra of water exposed to varied magnetic field exposure time showed the presence of this special feature as well. FTIR spectrum given in figure 3.20 b) and c) are the repetitions of the same experiment but the corresponding

appearance of the special feature is not the same. It can be concluded that the magnetic field does not have any effect on the main absorption bands of water. The appearance of the new feature may not be a consequence of magnetic field effect/memory due to the inconsistency in its appearance.

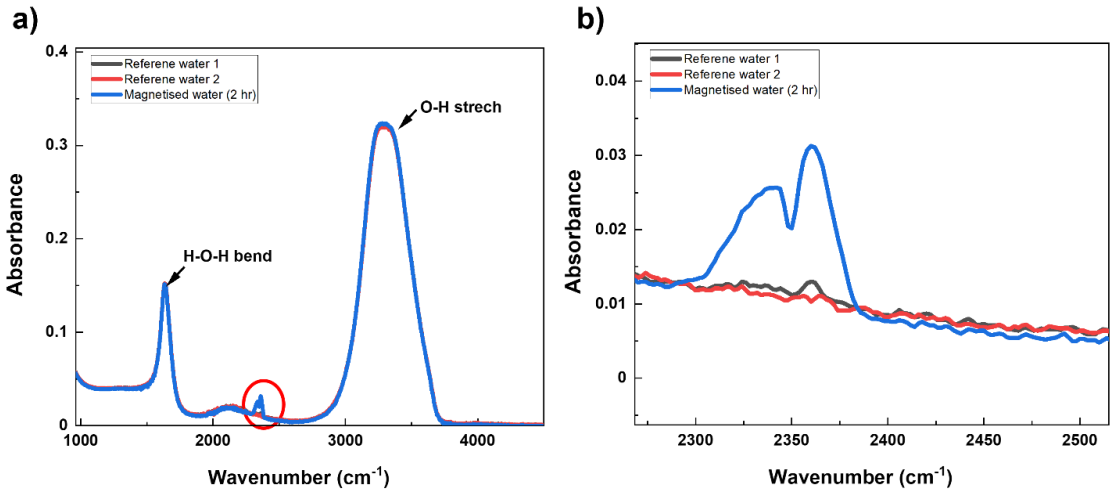


Figure 3. 19: FTIR spectrum of the magnetized water for 2 hours. Black and red are for the reference water and blue line is magnetized water. Red circle shows the appearance of a new feature for magnetized water. The zoomed picture of the red circled part of the spectrum is shown in panel b).

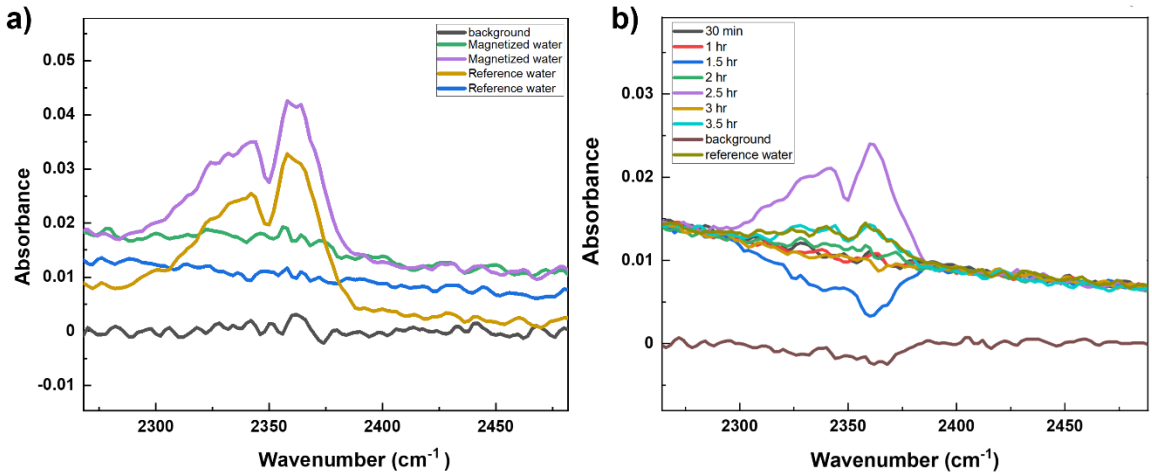

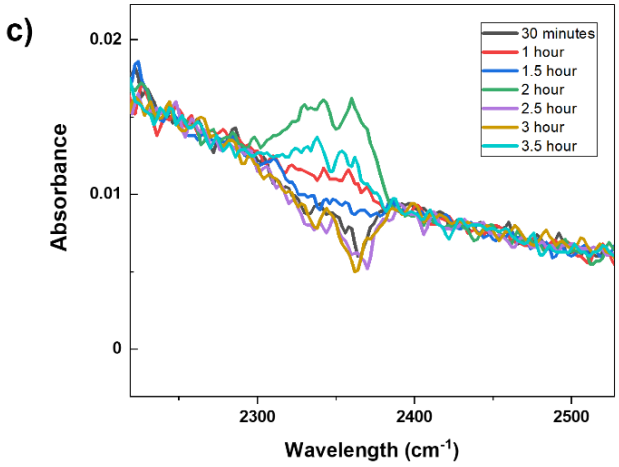


Figure 3. 20: FTIR spectrum of reference water and water exposed to the magnetic field (magnetized water). a), b) and c) are different repetitions

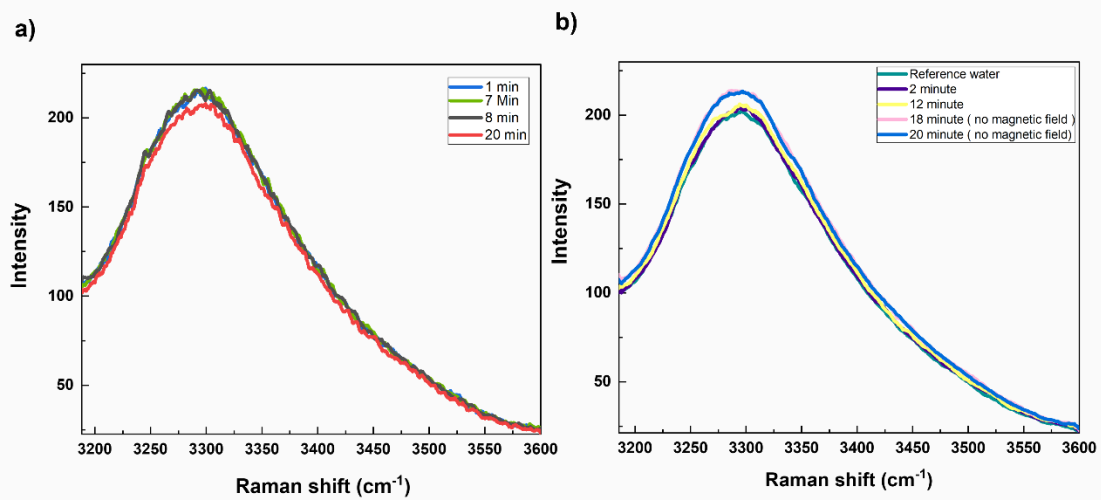


Figure 3. 21: Raman spectrum of reference of water and magnetized water a) time evolution of the Raman spectrum of magnetized water b) Spectra recorded having a cube magnet on the side of the water drop and from 18 minutes, the magnet has been removed.

The time evolution Raman spectra of magnetized water shown in Fig.3.21 a) did not show any difference with time. However the spectra recorded keeping a cube magnet on the side show a

small difference in the peak when the magnet is taken out after 18 minutes. The spectra show a small offset when the magnet is taken out and hence the difference in the peak might fall into the right place if the offset is corrected. Therefore, the Raman spectrum did not show any significant changes in magnetic field.

### 3.4.3 NMR

Time evolution of the chemical shift of water exposed to a B∇B magnetic field is shown in figure.3.22. The NMR spectrum has been captured every 30 seconds to get the time evolution of the chemical shift in the spectra. It shows a significant chemical shift of 0.4ppm between the first and second scan in 30 seconds.

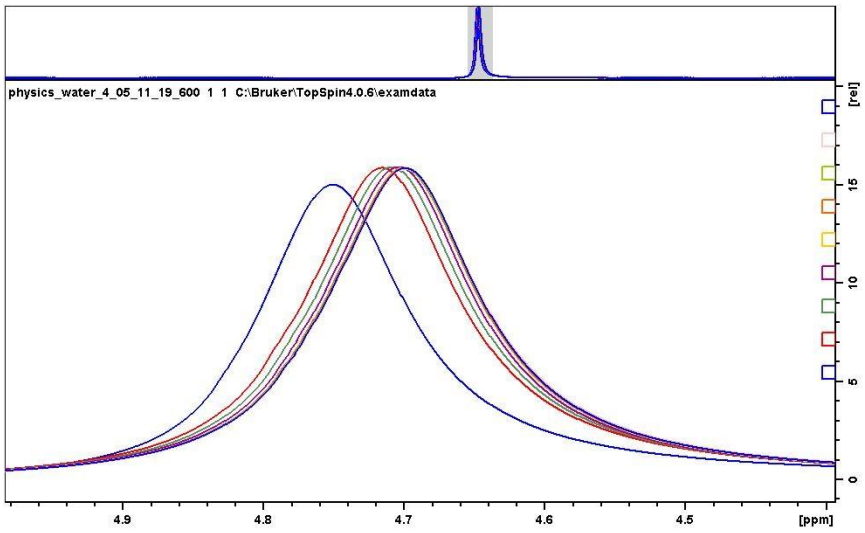


Figure 3. 22: chemical shift of magnetized water exposed to a B∇B field. Different lines are the chemical shift of the same magnetized sample recorded in every 30 seconds

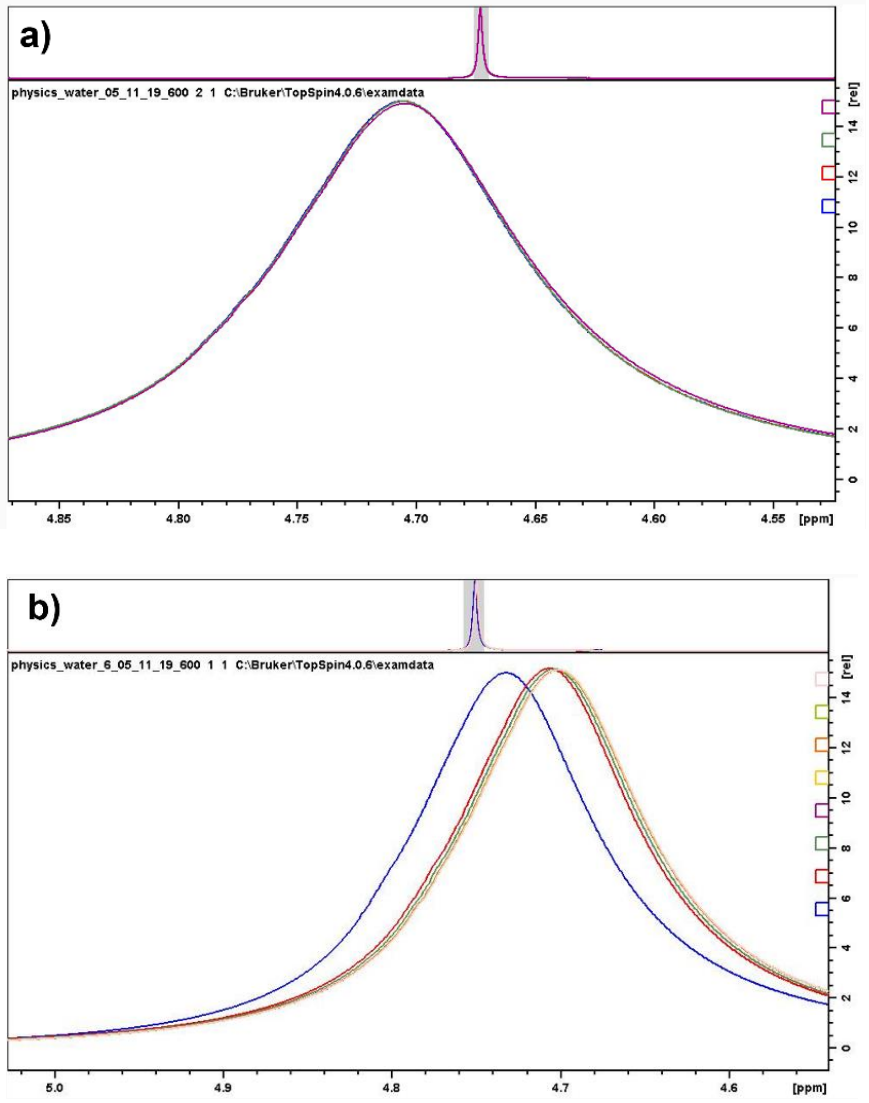


Figure 3. 23: Chemical shift of two samples of reference water. Different lines are the chemical shift of the same magnetized sample recorded in every 30 seconds.

Chemical shift of reference water showed different behaviours as shown in fig 3.23 a) and b). The possible reason for this effect could be the high magnetic field inside NMR. Therefore, it cannot be used to check the magnetic field effects on water. We have inconclusive and inconsistent data from NMR for several repeated experiments.

## 3.5 Conclusions

The rapid short-term decrease in evaporation rate of water and increase in the evaporation rate of urea solution are attributed to the replacement of water vapour of ambient air in the beaker with an equilibrium 3:1 ortho:para ratio by a vapour whose isomeric composition increasingly resembles the that of the vapour escaping from the liquid surface. A phenomenological model of evaporation of ortho and para water vapour that treats the two as independent gasses allows the water and the urea solution to be allocated to different zones of isomeric composition. Narrowing down the possible regions of composition by including condensation and assuming the same value $c \approx 0.45$ for both liquids leads to estimates of the ortho fraction $f_L^0$ in vapour freshly-evaporated from liquid of $0.39 \pm 0.1$ in water and $0.50 \pm 0.3$ in 6M urea. A slightly different acceptable choice of $c$ makes little difference to the numbers.

Our extensive studies in runs lasting up to 60 hours of evaporation of water exposed to a 500 mT magnetic field, with a no field control measured simultaneously side-by-side in the same environment show a consistent *increase* of approximately 12 % in evaporation rate in the magnetic field, under conditions where evaporation is not greatly enhanced by surface airflow. Fluctuations and scatter in the data are mostly ascribed to variations in ambient humidity, which has a strong influence on the evaporation rate. This confirms earlier reports [10,16,18,21,22,24] of an increase based on less rigorous methodology. For 6M urea the effect of the magnetic field is to produce a larger *decrease* of evaporation rate. To the best of our knowledge, this is a new finding. The field effects on the evaporation are attributed to the ability of the field to alter the ortho:para ratio in the water vapour on the beaker. Of the two mechanisms we consider, nuclear Larmor precession will always increase the rate, regardless of isomeric composition, contrary to observation. Lorentz stress will always increase ortho:para ratio, and produce the opposite signs of the field effects we observe in water and urea.

Our model is phenomenological and simplified, but it makes clear predictions that can be tested in further experiments, for example, sufficiently strong magnetic field gradients should always enhance the evaporation rate. It is worthwhile examining terahertz spectra of rotational transitions on freshly evaporated water vapour in an effort to quantify the isomeric ratio in water

vapour collected in confined spaces from different liquids, before and after magnetic treatment. Another experimental challenge is a controlled investigation on a timescale from minutes to hours of the remarkable claims of a magnetic memory in water and its possible relation to hydrogen bonding, and the isomeric ratio in liquid water.

# Bibliography

[1] D. Gebauer, A. Völkel, and H. Cölfen, Science **322**, 1819 (2008).

[2] E. M. Pouget, P. H. H. Bomans, J. A. C. M. Goos, P. M. Frederik, G. d. With, and N. A. J. M. Sommerdijk, Science **323**, 1455 (2009).

[3] R. Demichelis, P. Raiteri, J. D. Gale, D. Quigley, and D. Gebauer, Nature Communications **2**, 590 (2011).

[4] H. Du and E. Amstad, Angewandte Chemie International Edition **59**, 1798 (2020).

[5] J. M. D. Coey, Philosophical Magazine **92**, 3857 (2012).

[6] J. Azoulay, World Journal of Engineering **13**, 120 (2016).

[7] M. Colic and D. Morse, Colloids and Surfaces A: Physicochemical and Engineering Aspects **154**, 167 (1999).

[8] E. Chibowski and A. Szcześ, Chemosphere **203**, 54 (2018).

[9] Y. Fujimura and M. Iino, Journal of Physics: Conference Series **156**, 012028 (2009).

[10] E. Chibowski, A. Szcześ, and L. Hołysz, Colloids and Interfaces **2**, 68 (2018).

[11] M. Hayakawa, J. Vialetto, M. Anyfantakis, M. Takinoue, S. Rudiuk, M. Morel, and D. Baigl, RSC Advances **9**, 10030 (2019).

[12] E. J. L. Toledo, T. C. Ramalho, and Z. M. Magriotis, Journal of Molecular Structure **888**, 409 (2008).

[13] S. A. Ghauri and M. S. Ansari, Journal of Applied Physics **100**, 066101 (2006).

[14] T. I. Quickenden, D. M. Betts, B. Cole, and M. Noble, The Journal of Physical Chemistry **75**, 2830 (1971).

[15] T. Wu, Environmental Engineering Science **37**, 717 (2020).

[16] J. Nakagawa, N. Hirota, K. Kitazawa, and M. Shoda, Journal of Applied Physics **86**, 2923 (1999).

[17] J. A. Dueñas, C. Weiland, M. A. Núñez, and F. J. Ruiz-Rodriguez, Journal of Applied Physics **127**, 133907 (2020).

[18] Y.-Z. Guo *et al.*, International Journal of Molecular Sciences **13**, 16916 (2012).

[19] F. Lafta, N. Hassan, A. Jafar, and A. Hashim, international science and investigation journal **2** (2013).

[20] A. Seyfi, R. Afzalzadeh, and A. Hajnorouzi, Chemical Engineering and Processing - Process Intensification **120**, 195 (2017).

[21] H. B. Amor, A. Elaoud, N. B. Salah, and K. Elmoueddeb, Int. J. Adv. Ind. Eng. **5**, 119 (2017).

[22] F. Rashid, N. M. Hassan, J. A. Mashot, and A. Hashim, International Science and Investigation journal **2**, 61 (2013).

[23] H. Ben Amor, A. Elaoud, H. Ben Hassen, T. Ben Amor, N. Ben Salah, D. Stuerga, and K. Elmoueddeb, Arabian Journal for Science and Engineering (2021).

[24] L. Holysz, A. Szczes, and E. Chibowski, Journal of Colloid and Interface Science **316**, 996 (2007).

[25] A. Szcześ, E. Chibowski, L. Hołysz, and P. Rafalski, Chemical Engineering and Processing: Process Intensification **50**, 124 (2011).

[26] Y. Wang, H. Wei, and Z. Li, Results in Physics **8**, 262 (2018).

[27] J. A. Dueñas, C. Weiland, I. García-Selfa, and F. J. Ruíz-Rodríguez, Journal of Magnetism and Magnetic Materials **539**, 168377 (2021).

[28] Q.-w. Yang, H. Wei, and Z. Li, DESALINATION AND WATER TREATMENT **216**, 299 (2021).

[29] M. V. Carbonell, E. Martinez, and J. E. Díaz, Int. Agrophys. **16**, 171 (2002).

[30] J. M. D. Coey, (2009).

[31] S. J. Suresh and V. M. Naik, The Journal of Chemical Physics **113**, 9727 (2000).

[32] I. Vaskina, I. Roi, L. Plyatsuk, R. Vaskin, and O. Yakhnenko, Journal of Ecological Engineering **21**, 251 (2020).

[33] X. Pang and B. Deng, in *2009 International Conference on Applied Superconductivity and Electromagnetic Devices*2009), pp. 278.

[34] K. Higashitani, A. Kage, S. Katamura, K. Imai, and S. Hatade, Journal of Colloid and Interface Science **156**, 90 (1993).

[35] Evaporation from a water surface, https://www.engineeringtoolbox.com/evaporation-water-surface-d_690.html.

[36] K. Hisatake, M. Fukuda, J. Kimura, M. Maeda, and Y. Fukuda, Journal of Applied Physics **77**, 6664 (1995).

[37] K. Hisatake, S. Tanaka, and Y. Aizawa, Journal of Applied Physics **73**, 7395 (1993).

[38] A. Abragam, *The principles of nuclear magnetism*, pp. 589, Clarendon Press, Oxford, 1961.

[39] M Chaplin, Ortho and Para water, https://water.lsbu.ac.uk/water/ortho_para_water.html.

[40] V. I. Tikhonov and A. A. Volkov, Science **296**, 2363 (2002).

[41] H.-H. Limbach, G. Buntkowsky, J. Matthes, S. Gründemann, T. Pery, B. Walaszek, and B. Chaudret, ChemPhysChem **7**, 551 (2006).

[42] D. A. Horke, Y.-P. Chang, K. Długołęcki, and J. Küpper, Angewandte Chemie International Edition **53**, 11965 (2014).

[43] S. M. Pershin, Biophysics **58**, 723 (2013).

[44] S. Pershin and A. Bunkin, Laser Physics **19**, 1410 (2009).

[45] X. Xin, H. Altan, A. Saint, and D. Matten, Journal of Applied Physics **100**, 094905 (2006).

[46] X. Miao, J. Zhu, K. Zhao, H. Zhan, and W. Yue, Appl. Spectrosc. **72**, 1040 (2018).

[47] S. Kernbach, Journal of The Electrochemical Society **169**, 067504 (2022).

[48] S. M. Pershin, Atmospheric and Oceanic Optics **29**, 331 (2016).

[49] R. Mareka and J. Straubb, International Journal of Heat and Mass Transfer **44** (2001).

[50] V. Vlasov, Heat and Mass Transfer **55** (2019).

[51] Y. L. A. Rezus and H. J. Bakker, Proceedings of the National Academy of Sciences **103**, 18417 (2006).

[52] Y. Nagata, K. Usui, and M. Bonn, Physical Review Letters **115**, 236102 (2015).

# Chapter 4

# Evaporation of water in a microfluidic channel

## 4.1 Introduction

Microfluidics requires sample volumes in microlitres for sensing applications, especially for biomedical systems and chemical analysis. The dimension of the devices is in the micron range, which has many advantages such as minimal sample/reagent consumption, reduction of contamination risk, low cost per analysis, reduction of tedious operations, enhancement of sensitivity and reliability. Conventional macroscopic sample processing steps such as sampling, sensing and display can be minimized in a single microfluidic system. The microfluidic system is known as a lab-on-a-chip or micro-total analysis system (TAS). It functions as a laboratory inside a micron-sized chip.

Silicon was the common microfluidic substrate material in the beginning. However, after glass and polymer materials were introduced in the 2000s, microfluidic technology became an important research field. Glass and polymer-based substrate materials were cheaper than silicon and transparent. Commonly used materials are polymethylmethacrylate (PMMA), polystyrene (PS) and polydimethylsiloxane (PDMS). PDMS is the most commonly used material due to its biocompatibility, low cost, ease of fabrication and replication[1].

The equilibria prevailing in the miniaturized system are different than on the macroscale. Therefore, analyzing the dominant forces and new equilibria is important to have a better understanding of the system.  A scaling law expresses how a physical quantity varies with the

size of the system *l* while keeping other quantities such as temperature, pressure or time constant. We must consider volume forces such as inertia and gravity, and surface forces such as viscosity and surface tension[2].

As an example of a scaling law, the ratio of surface to volume force is

$$\frac{Surface\ force}{Volume\ force} = \frac{l^2}{l^3} = l^{-1} \rightarrow \infty_{l \rightarrow 0} \quad (1)$$

This indicates when scaling down, a surface force becomes predominant in contrast to a volume force in the macroscale. Table 1 below shows scaling laws for different quantities[2].

Table 1 Scaling laws with dimension *l* for different physical quantities

| Quantity | Scaling law |
|---|---|
| Intermolecular Van der Waals force | $l^{-7}$ |
| Van der Waals force density between interfaces | $l^{-3}$ |
| Time | $l^{0}$ |
| Capillary forces | $L$ |
| Distance | $L$ |
| Flow velocity | $L$ |
| Surface tension force | $l^{2}$ |
| Diffusion time | $l^{2}$ |
| Volume | $l^{3}$ |
| Mass | $l^{3}$ |
| Force of gravity | $l^{3}$ |
| Magnetic force with an external field | $l^{3}$ |
| Magnetic force without an external field | $l^{4}$ |

When two forces are present at a microscale, the force associated with the lower power of $l$ becomes dominant. For example, the effects of gravity ($l^3$) are negligible compared to capillary forces ($l$) in miniaturized systems. Furthermore, the magnetic field is not a dominant force in a microfluidic channel compared to capillary effects.

Evaporation-induced flow is prominent in microscale environments like droplets, menisci and thin films. The evaporation and interfacial flow of a meniscus has been a subject matter of many researchers. Experimental studies by Buffone et al. [3] and Dhavaleswarapu et al. [4] observed the presence of a circulating flow near the evaporating meniscus of ethanol and methanol. Buffone et al. [5] observed uneven evaporation across the meniscus. It is due to an evaporation induced temperature gradient, which leads to a surface tension gradient across the liquid-air interface. The non-uniform evaporation observed across the interface was more prominent at the edge than at the surface. The surface tension gradient flow near the interface has been monitored using particle image velocimetry (μPIV). Studies by Ward and Duan et al. [6-8] reported the formation of surface temperature gradients during the evaporation of a liquid with a free surface. The temperature gradients induce interfacial instabilities that lead to convection within the liquid.

The induced surface tension drives the liquid from the warmer region (centre of the meniscus) to the cold region (edge of the meniscus). The meniscus triple line region ( where vapour, liquid and solid phase meet) is an important region of interest since the evaporation and heat transfer is highest in this region, creating an evaporative cooling effect at the liquid-vapour phase boundary—this differential evaporation and temperature gradient causes the convection inside a liquid drop[9]. A gradient of temperature, electric field and the presence of foreign particles can produce surface tension stresses, resulting in interfacial flows[4]. According to a study by Hershey et al.[10], increased evaporation or condensation along the liquid interface produces local temperature gradients, which induce surface tension inequalities and generate liquid motion.

It is interesting to understand what influence a magnetic field may have on nano and microfluidic capillaries or channels since the human body and its body fluids are comprised mostly of water [11]. In this chapter, the evaporation of water in a microfluidic channel has been studied in the presence of a magnetic field. This experiment gives an idea of how a magnetic field could affect the solvent flow in a microfluidic channel and the physicochemical properties of the solvent, which are crucial parameters to be considered in different lab-on-a-chip applications.

Results from Chapter 3 showed a 12% increase in the evaporation rate of water in a magnetic field. Therefore, it is important to check if there is any magnetic field influence on water evaporation in a microfluidic channel, even though the magnetic force is not a dominant force. The experiments aimed to understand how a magnetic field could control and manipulate the properties of water in a microfluidic channel. The evaporation in a microfluidic channel can be calculated by monitoring the meniscus movement with time. Choosing the best microfluidic channel for the experiment is vital since the channel material plays a significant role in liquid flow. A microfluidic channel with channel walls of different wetting natures complicates the studies since wetting is different on different surfaces, creating a wetting non-uniformity.

## 4.2. Microfluidic systems

A microfluidic chip can be fabricated by assembling two or three different materials. Commonly used materials for chip fabrications are PDMS and PMMA. The nature of the microfluidic walls are of paramount importance since the abnormalities and imperfections on the channel walls may result in pinning of drop.

### 4.2.1 PMMA/PSA/PMMA

It is a sandwich-type microfluidic chip where a pressure-sensitive adhesive (PSA) is placed between two PMMA materials and the channel height is determined by the height of the adhesive. The channel dimensions were first made in CAD software and then transferred to a cutting plotter, GRAPHTEC, to cut the PSA layer of the microfluidic chip. The PMMA layers

were cut using a $CO_2$ laser (Universal Laser Systems). Pressure-sensitive adhesives are micron-sized double-sided adhesives and make sidewalls of the channel that are rough and non-uniform. Since our study is based on water evaporation in a microfluidic channel, rough, non-uniform and chemically inhomogeneous walls would yield complex, unreliable data.

### 4.2.2 PDMS/Glass

This system was fairly easy to fabricate from glass and PDMS layers. PDMS monomer and curing agent were mixed in a 10:1 ratio and poured above the channel mould after degassing. After curing at room temperature for 24 hours, it was peeled off from the mould. The PDMS was plasma treated for 15 minutes to make them hydrophilic for better adhesion to the coverslips. After the treatment, the PDMS layer was slowly pressed against the coverslip. The smooth channel walls made from glass and PDMS, make them ideal for the studies. The formation of unwanted bubble/ small bubble condensation during evaporation has been observed during the experiment. The possible cause of the bubble formation could be the high intrinsic gas solubility and permeable nature of PDMS. This system is not useful for our studies because of bubble formation, which might impede the evaporation process.

### 4.2.3 PMMA/PMMA

This microfluidic system was fabricated by thermolamination of three separately $CO_2$-laser cut PMMA layers. The schematic diagram of the fabricated microfluidic channel is shown in figure 4.1. The middle layer PMMA is cut using $CO_2$-laser to the required channel length and width and the thickness of the middle layer decides the height of the channel. The top and bottom layer PMMA sheets cover the middle layer PMMA making a 3D channel and therefore it is open only at the ends of the channel. The advantage of this method is the chemical homogeneity of the microfluidic channel walls.

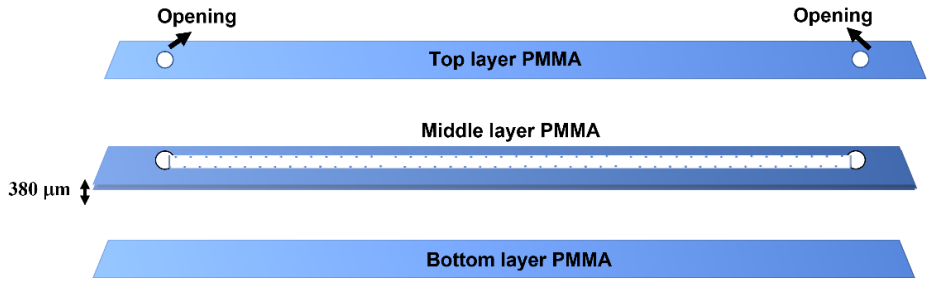


Figure 4. 1: Schematic diagram of a microfluidic channel. The $CO_2$ laser cut middle channel show small reference

All the above methods were used to figure out the best method and material for this study. The polymethylmethacrylate (PMMA) based microfluidic channel is the perfect choice due to its homogenous wetting.

## 4.3 Experimental methods

Two identical microfluidic channels of height 380 microns, one in a magnetic field and the other as a control without a magnetic field, were used in the experiment. The evaporation of both channels, one with and the other without a magnetic field, has been monitored simultaneously with two PCE800mm USB cameras. The channels were prewetted prior to the experiment. First, 0.6 – 0.7 microliters of water was placed on one side of the channel, and the other side was connected to a syringe pump.

A drop of millipore water is pumped through channel centre using the syringe pump, to wet the surface of the channel. Then a further 0.4 microliters of water was placed on one side of the channel and the water drop is moved to the centre of the prewetted channel using the syringe pump. The movement of the meniscus in each channel was then recorded using the camera. Two similar microfluidics channels have been used, one with the magnetic field and the other as a control. We have used one or two rectangular magnets, 50 x 20 x 10 mm made of Nd-Fe-B with a remanence of 1.26 T that produce a surface field of 300 mT that is applied field on one of the channels.

The whole setup was placed inside a perspex box, and the temperature (26 ℃) and humidity (42%) were controlled using a tempertaure and humidity controller throughout the experiment. The schematic experimental setup is shown in Fig. 4.2. The surface tension forces on the water drop are determined by the curvature of the meniscus which suggests that the direction of the magnetic field with respect to the meniscus might be important.

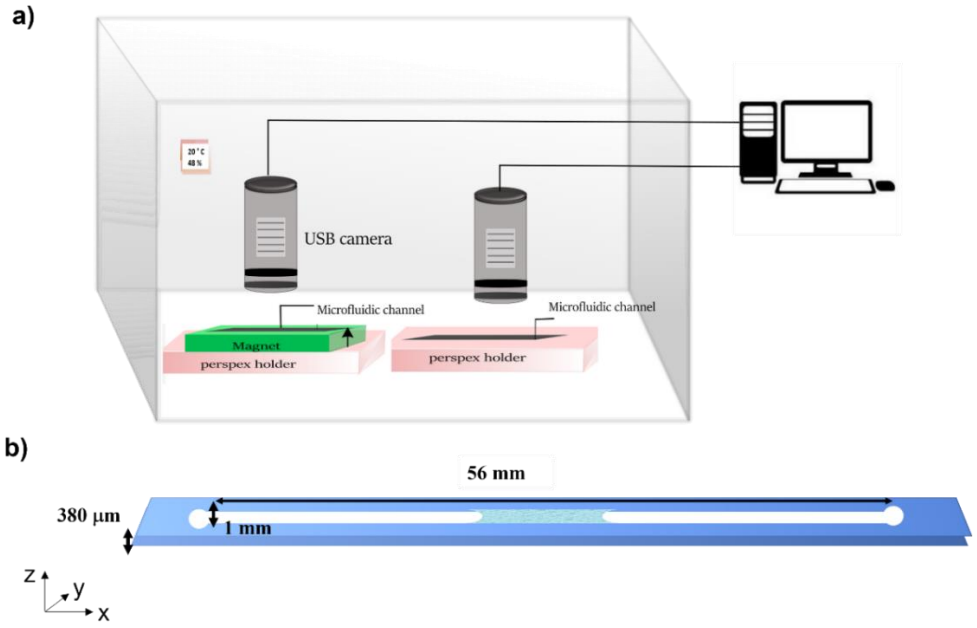


Figure 4. 2: a) Experimental setup for evaporation experiment where temperature and humidity are controlled. b) schematic of the dimension of a microfluidic channel with a water drop at the centre

We have used two custom-made magnetic assemblies to apply the magnetic field. In setup 1, the magnetic field is perpendicular to the chip, in the *z* direction and in setup 2, the magnetic field is perpendicular to the channel, in the *y* direction. The measured magnetic field profile of the magnetic field assemblies are shown in figure 4.3 and 4.4.

**Magnetic field $B_z$**: The rectangular magnet with a surface field of 300 mT is beneath the chip and the magnetic field is perpendicular to the chip, as shown in Fig.4.3.

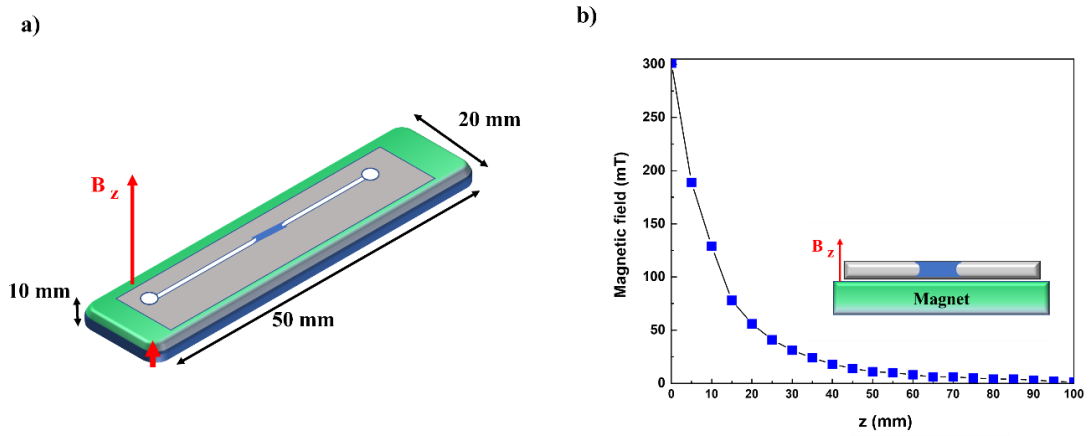


Figure 4. 3: a) Schematic diagram of a microfluidic channel in-plane magnetic field (water meniscus shown as blue) b) Magnetic field profile of the rectangular magnet.

**Magnetic field $B_y$**: The two rectangular magnets were placed in 3D printed holder separated by a distance of 27 mm, producing a field of 220 mT at the centre. The microfluidic channel is placed in the middle of this setup, where the magnetic field is parallel to the chip. The profile of the magnetic field is shown in figure 4.4.

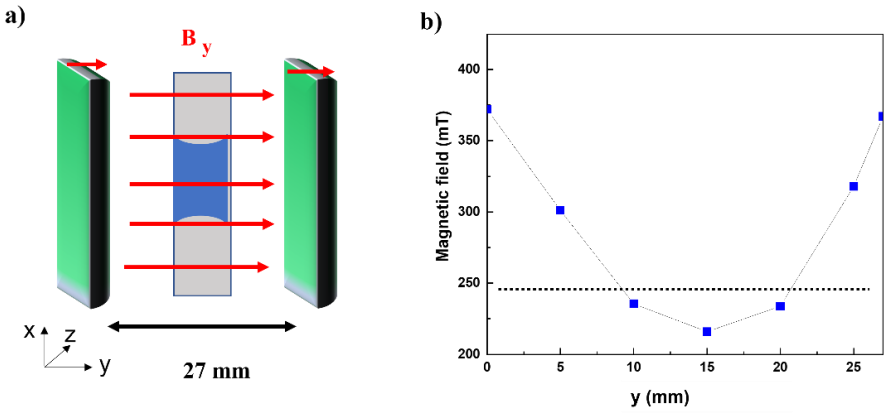


Figure 4. 4: a) The experimental setup of water meniscus in a magnetic field where the field is parallel to the meniscus b) magnetic field profile of the magnet setup and the microfluidic channel is placed at the middle where the water drop in the channel is in a 220 mT field

## 4.4 Results

The water drop with two menisci at the channel centre is the region of interest of our studies. The movement of the menisci was monitored in real-time, which directly relates to the evaporated volume of the water. Hence the evaporated volume of the short liquid thread or drop is characterized by two parameters, '*L*' the contact length of the meniscus with the wall and '*l*' the shortest distance between the centres of the two menisci, as shown in figure 4.5. The volume of the liquid thread can be calculated from *L* and *l* knowing the width *w* and the depth *d* of the channel.

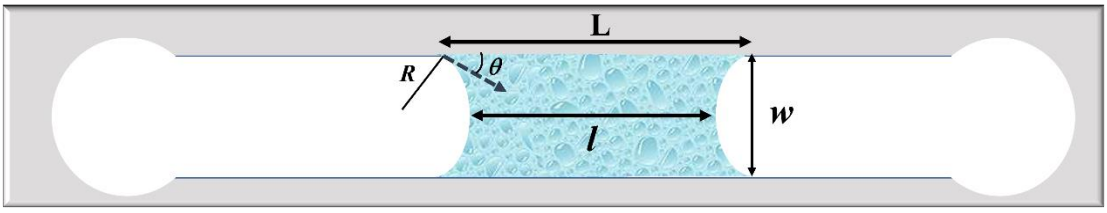


Figure 4. 5: Schematic of a microfluidic channel and water meniscus

The ratio L/*l* is useful to characterize the movement of the menisci since it is related to the force on the meniscus; as the radius of curvature *R* decreases, the contact angle θ decreases and the surface tension force per unit length γcosθ increases

The relation between R, *L*, *l* and the width *w* of the tube is deduced from the intersecting chords theorem.

$$R = \tfrac{1}{4} [\, w^2/(L - l) - (L - l)] \qquad (2)$$

If *d* is the depth of the channel, the area *A* of each meniscus is approximately

$$A \approx 2Rd \arcsin(w/2R) \qquad (3)$$

Since PMMA is hydrophobic, we assume the contact angle with the top and bottom sheets of PMMA that form the channel is close to 90°. The contact angle seen in Fig. 4.5 is only at the rough, laser-cut vertical edges.

The volume $V$ of the thread of water is approximately,

$$V \approx 1/3(Lwd) + 2/3(lwd). \quad (4)$$

For example, the volume of a drop with L = 2 mm, $l$ = 1.5 mm in the channel with width $w$ = 1 mm and $d$ = 0.38 mm is 0.63 μL. The ratio $L/l$ is a convenient parameter to use to describe the magnetic field effects on the evaporating water. Some examples of the real-time movement of the meniscus are shown in Fig. 4.6 and Fig 4.7 Any deformations or irregularities on the channel walls pin the movement of the menisci, increase their area, and increase the evaporation rate/

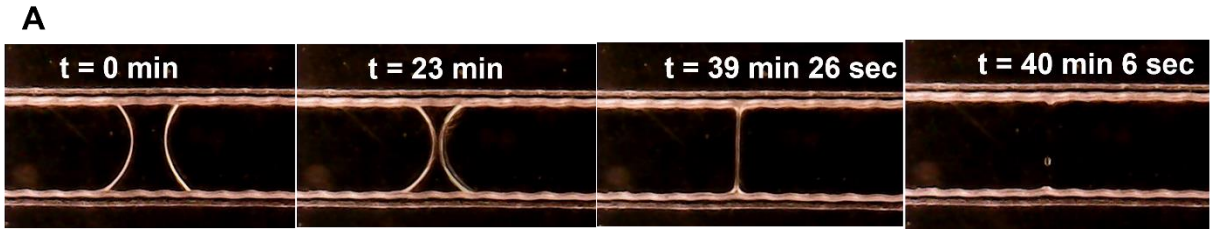


Figure 4. 6: Example A. Real-time evaporation of water samples in a microfluidic channel. Shrinking of the volume leads to a membrane across the channel, which breaks 30 seconds later. Note that the contact angle with the walls seen in the menisci is about 30°, but the contact angle with the flat upper and lower surfaces of the channel is close to 90°. In this experiment the initial volume was 0.12μL

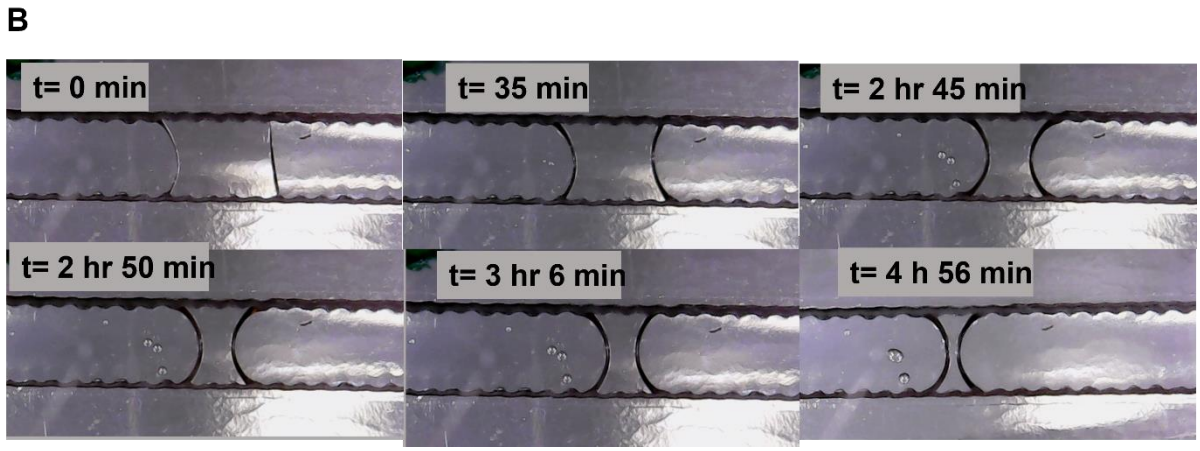

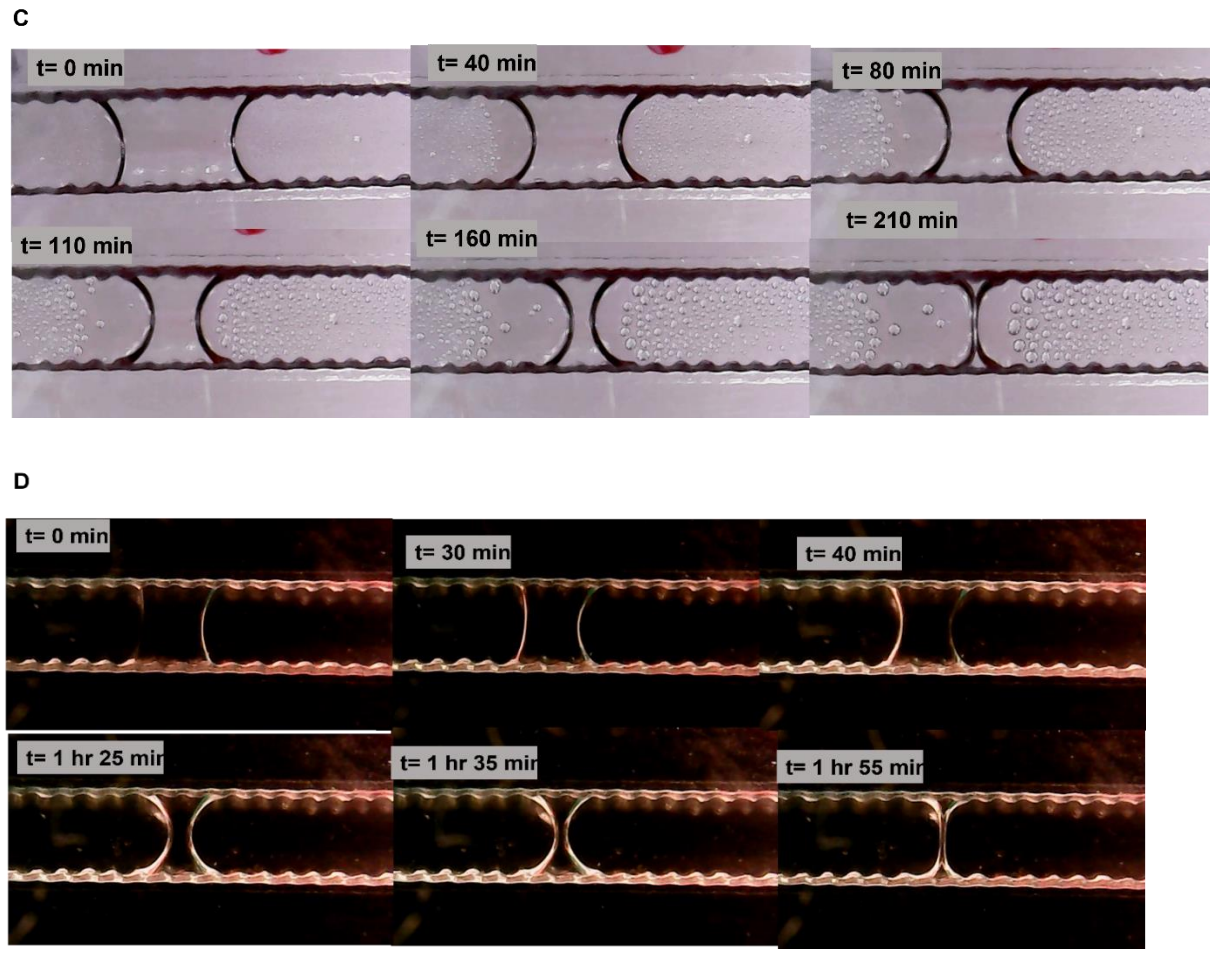


Figure 4. 7: More examples of real-time evaporation of water samples in a microfluidic channel. Shrinking the volume leads to a membrane across the channel, which ruptures 5 hours, 3 hour 30 minutes and 1 hour 55 minutes later for examples B, C, D respectively. Note that recondensed water droplets accumulate on the flat PMMA surfaces on both sides of the drop in experiments 1 and 2.

The pipetted volume of 0.4 μL is accurate to 0.1 μL, so the small sample volume is barely outside the sensitivity of the micropipette. In addition, the channel material, PMMA, is chemically hydrophobic, and the channel has to be pre-wetted using a syringe pump. This could change the final volume of the second drop that is placed in the middle of the channel and its

evaporation monitored. Therefore, normalized values of L and *l* have been plotted since the initial lengths in the experiments were slightly different.

Two microfluidic channels were used side by side during the experiment, one with a field and the other with a control. The top panel in Fig. 4.8 a) and b) depicts how *L* and *l* decay during the first evaporation experiment, and the bottom panel c) and d) during the second evaporation experiment. The fitted normalized plots of *L* and *l* in both experiments have different slopes

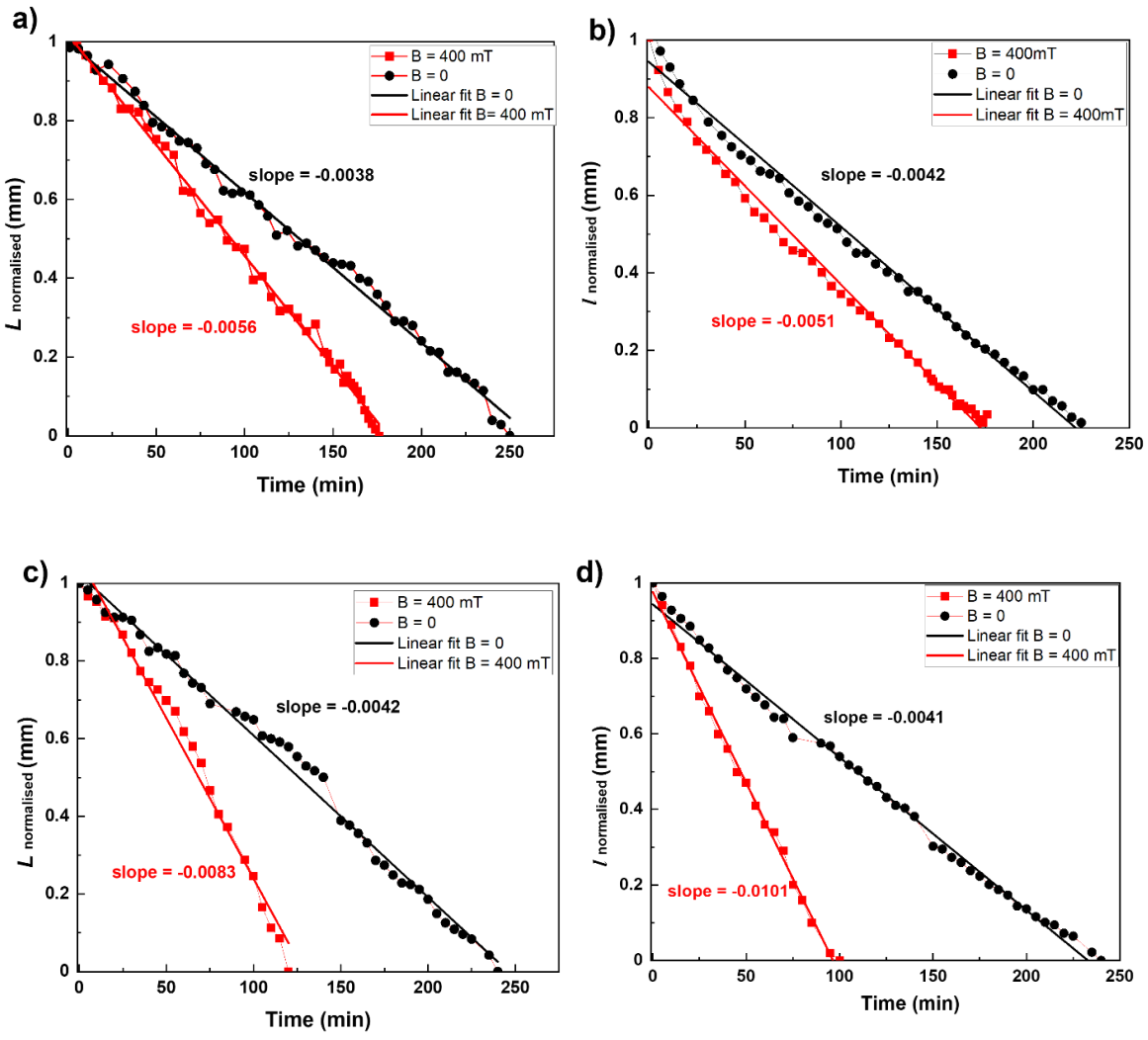


Figure 4. 8: a), b) shows normalised plots of *L* and *l* versus time in experiment 1 and c), d) in experiment 2 (red is for meniscus in a $B_z$ magnetic field and black is for control water)

In both cases the water takes about four hours to evaporate without a field. The evaporation rate is of a 0.4 mg (40 µL) drop is therefore approximately 0.13 $kgm^{-2}h^{-1}$ , or 3 – 4 times greaterthan for the beakers in Chapter 3.

Table 2 : Slope of normalized plot of *L* and *l* in a $B_z$ field

| **Experiment** | **Parameter** | **Slope (B = 0 mT)** $min^{-1}$ | **Slope ($B_z$ = 300 mT)** $min^{-1}$ |
|---|---|---|---|
| 1 (Fig 4.8a) | L | -0.0038 | -0.0056 |
| 1 (Fig 4.8b) | *l* | -0.0042 | -0.0051 |
| 2(Fig 4.8c) | L | -0.0042 | -0.0083 |
| 2(Fig 4.8d) | *l* | -0.0041 | -0.0101 |

The slopes of the normalized graphs of *L* and *l* is given in table 2. In both experiments. *L* and *l* decay faster for water in a magnetic field than in the control water. The magnetic field increases the evaporation rate by 34 % in experiment 1 and by 120 % in experiment 2. The water in the channel evaporates much faster in the presence of a magnetic field in most of the experiments. Further representative examples of the rate of volume change of the water drop exposed to a perpendicular or in-plane magnetic field compared to the zero-field control are shown in figure 4.9 and 4.10. Many repeated experiments showed a similar effect of magnetic field even though the total evaporation times were somewhat different.

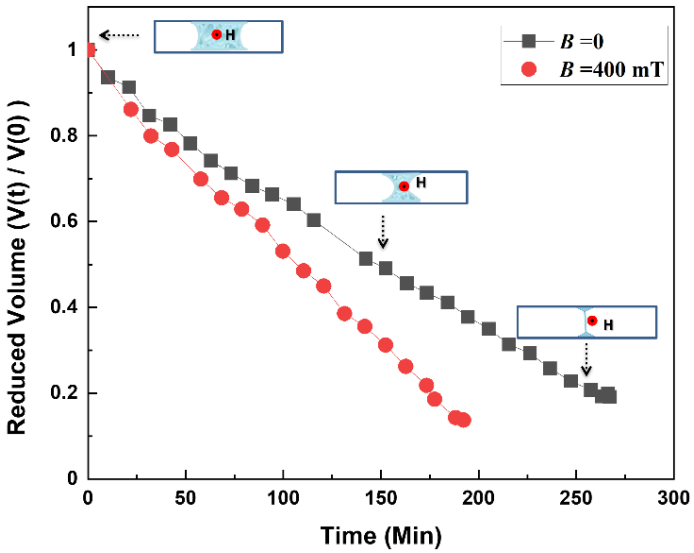


Figure 4. 9: Plot of reduced volume versus time for a 300 mT $B_z$ magnetic field and control water. The rate of evaporation is 49% greater in the field.

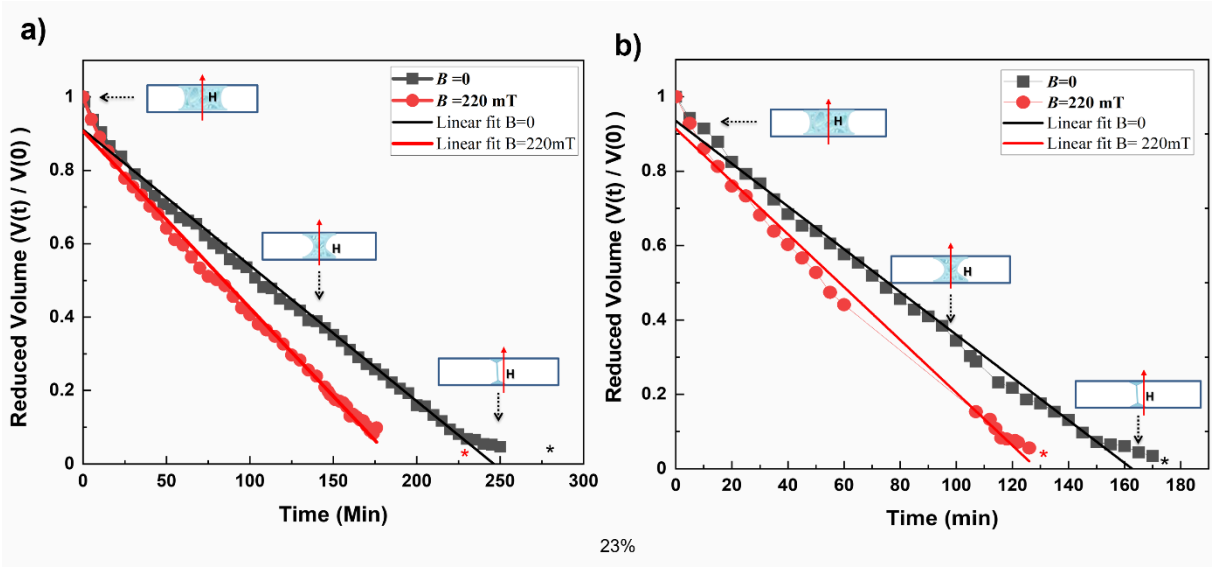


Figure 4. 10: Plots of two examples of reduced volume versus time with and without a 220 mT $B_y$ magnetic field . The evaporation in the field in 28% faster in a) and 23% faster in b)

The average evaporation rate from the slope of the reduced volume graph of Fig. 4.9 is 0.085 $kgm^{-2}h^{-1}$ for the control and 0.125 $kgm^{-2}h^{-1}$ in the 300 mT $B_z$ field.

Table 3 : Slope of a plot of normalized volume in a $B_y$ field

| **Experiment** | **Slope (B = 0 mT)** $min^{-1}$ | **Slope ($B_y$ = 220 mT)** $min^{-1}$ |
|---|---|---|
| 1 (Fig 4.10a) | -0.0037 | -0.048 |
| 2 (Fig 4.10b) | -0.0057 | -0.071 |

The slope of water evaporation in a $B_y$ field (Fig.4.10) is given in Table 3. The water drop exposed to the $B_y$ field again evaporates faster, as shown in Figs 4.9 a) and b), but the increase is less than that observed in the $B_z$ field (Figs 4.8 and 4.9). However, we do not know if the difference is due to the lower field, or the different field direction.

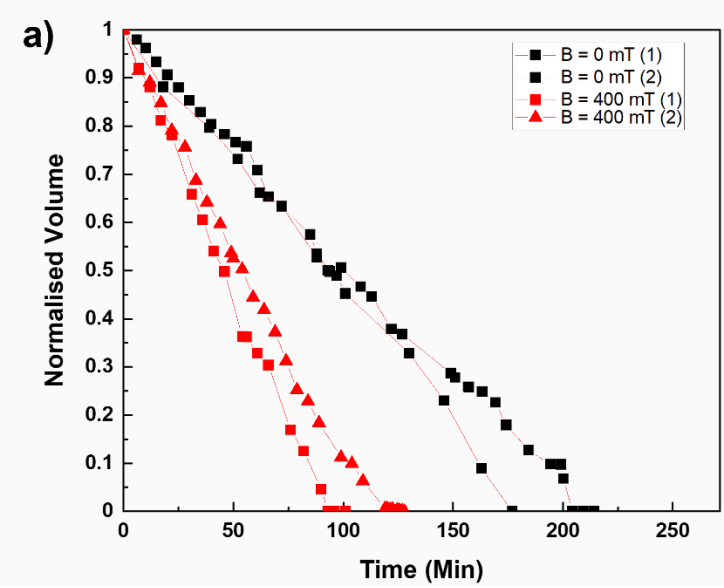


Figure 4. 11: a) shows the evaporation of water in the same microfluidic channel for repeated experiments. There is small reduction in the evaporation when many experiments are repeated in the same channel

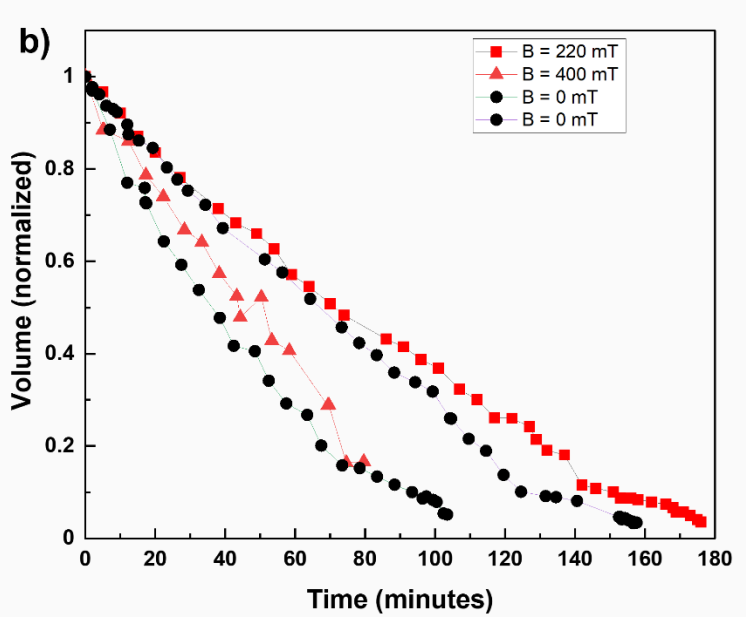


Figure 4. 12: (a) Plot of normalized volume of repeated experiments on the same day (same microfluidic channel) (b) Evaporation experiments of control water (in black) and water exposed to the magnetic field (in red) on different days.

Figure 4.12 shows evaporation experiments on different days for the $B_z$ field, the $B_y$ field and control (s). Evaporation of control water ($B$ = 0 mT) shows different behavior in two different experiments even though it was performed in the same channel. Evaporation of water in a magnetic field also decays differently and slightly slower than control water in this one case. The observed discrepancy for the increase in the evaporation rate of water in the magnetic field could be due to the change in the initial volume. Controlling the initial volume that reaches the centre of the channel is difficult because of the small sample volume and pre-wetting of the surfaces. Care has to be taken at this stage since any leftover liquid at the channel might contribute to the initial volume of the drop.

However, in all the other experiments, water in the presence of magnetic field evaporated faster than the control water, and sometimes much faster. Different repeats of the same

the experiment yielded somewhat different evaporation rates (Fig. 4.11a) even though they followed the same trend of greater evaporation under magnetic field.

## 4.5 Discussion

Based on these experimental on water evaporation in the microfluidic channel, there are two results to explain, particularly in relation to the findings in the last chapter.

i) The much greater evaporation rate in the microfluidic control channel than in the beaker control.

ii) The greater influence of magnetic field on the evaporation rate in the microfluidic channels.

Using the results presented in §4.4, we have ten datasets. The average evaporation rate from the control channel is $0.130 \pm 0.028$ $kgm^{-2}s^{-1}$. Among the results on evaporation from the beakers in Ch 3, we have five 60 h zero-field runs, for which the average evaporation rate is $0.0277 \pm 0.0051$ $kgm^{-2}s^{-1}$ (errors are one standard deviation). The average rate for the 16 hour runs is similar, 0.0266 $kgm^{-2}s^{-1}$The evaporation rate of water in the microfluidic channel is therefore *four times greater* than it is in the beaker.

We might have expected that a build-up of water vapour in the microchannel would increase relative humidity and reduce the evaporation rate. The opposite is true. The possible origin of this increased water evaporation rate in a microfluidic channel is the evaporation induced surface tension gradient[3,4,6-9] that appears at a meniscus in a capillary. At the beginning of most of the experiments, evaporation of both water menisci occurs at a similar rate. The non-uniform evaporation causes a temperature gradient along the water/air interface, and it is more intense around the triple junction edge than at the centre. As the experiment proceeds, $l$ (the distance between menisci) is decaying even when $L$ is stuck, indicating more evaporation around the edge of the meniscus and a higher temperature drop (e.g.Fig 4.8 c) and d)). This causes a higher surface tension gradient that drives more liquid from the centre across

the interface, creating an internal flow inside the liquid meniscus and enhancing its velocity, known as the Marangoni effect. A pictorial representation of the effect of evaporation-induced internal flow is given in figure 4.13.

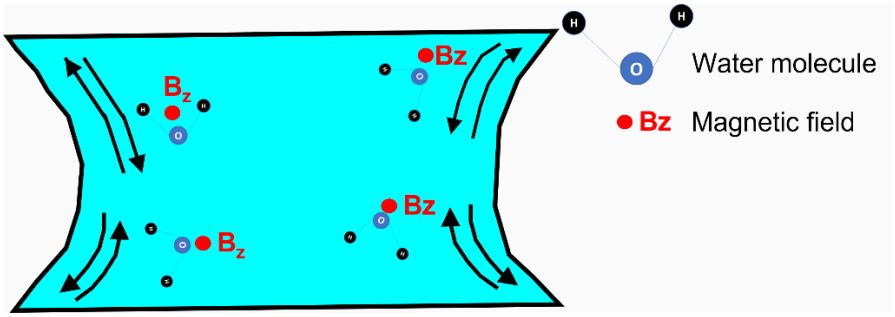


Figure 4. 13: Pictorial representation of the convective vortex flow due to non-uniform evaporation that is greatest at the meniscus. There is a temperature gradient and a corresponding surface tension gradient, The surface flow of liquid due to the evaporation-induced surface tension gradient.

The evaporation rate from a surface is strongly enhanced by convective flow,as described in chapter 3 shown by Eq 5

$$g = (25 + 17v)x_s(1 - RH) \qquad (5)$$

It is interesting to compare the measured evaporation rates $g$, with that expected from this formula. In the present case, where $T$ = 26℃ and $RH$ = 42 %, $x_s$ = 24g/kg the evaporation rate without convection ($v$ = 0) should be 0.0348 $kgm^{-2}h^{-1}$. The average measured value of 0.110 $kgm^{-2}s^{-1}$ suggests that $v \approx 3.2$ $ms^{-1}$. This seems impossible inside the microfluidic channel, but flow speeds of order a few tenths of a millimeter per second in the liquid meniscus (Fig. 4.11) are able to enhance the evaporation rate substantially[3].

The field enhancement of the evaporation rate in the microfluidic channel is much greater than it was in the beakers, where we suggested that the Lorentz torque on the evaporating water

molecules altered the ortho:para ratio. This mechanism should be active, but it is not able to explain effects as large as we observe in Figs 4.8 – 4.10. The field effect we found on the surface tension of water in Chapter 2 was very small (0.3%), which is expected to change the convection illustrated in Fig.4.11 only slightly. The Lorentz force on a charged particle

$$F_L = q(v \times B) \quad (6)$$

only applies when if the water molecules or other species carry a net charge *q*, but very few of them do a neutral pH. It is possible that the most energetic water molecules in the Maxwellian distribution the vapour phase might have sufficient energy to become ionized in collisions, but the consequences cannot be forseen at present.

## 4.6 Conclusion

There is a consistent trend for the evaporation rate of water to increase in a microfluidic channel, although there are small variations in the initial volume of the evaporating water drop in the microfluidic channel that explains the scatter in the evaporation rate based on a volume of 0.40 µL. The average observed evaporation rate of water in the microfluidic channel is three times greater than in the beakers, which is likely due to the much greater surface to volume ratio in the microfluidic channel that enhances the importance of changes at the surface (scaling law). Thermally induced flow with velocity of order 0.3 $mms^{-1}$ induced by the enhanced evaporation at the meniscus with temperature drop and a resulting surface tension gradient [3-7,9] is the likely reason behind this effect.

The explanation we proposed in Chapter 3 in terms of the ortho/para isomers of water vapour does not explain the large observed magnetic field effect on enhanced evaporation of water in a microfluidic channel where changes in the evaporation rate of 50 – 100 % are observed. The Lorentz force can only be invoked if there are charged species such as $H^+$ or $OH^-$ in the liquid or vapour phase. It could be a result of a field effect on the surface tension of water that influences the evaporation-induced internal flow caused by the surface tension gradient but we have found in Chapter 2 that the field effect on the surface tension of bulk water

is very small, ~ 0.3%. At present, we can only speculate that the field effect on surface tension is much enhanced when the dimensions are scaled down in the channel.

# Bibliography

[1] Y. Song, D. Cheng, and L. Zhao, *Microfluidics: Fundamental, Devices and Applications: Fundamentals and Applications* 2018).

[2] P. Tabeling, *Introduction to Microfluidics* (Oxford University Press, 2005).

[3] C. Buffone, K. Sefiane, and J. R. E. Christy, Physics of Fluids **17**, 052104 (2005).

[4] H. K. Dhavaleswarapu, P. Chamarthy, S. V. Garimella, and J. Y. Murthy, Physics of Fluids **19**, 082103 (2007).

[5] C. Buffone and K. Sefiane, Experimental Thermal and Fluid Science **29**, 65 (2004).

[6] F. Duan, V. K. Badam, F. Durst, and C. A. Ward, Physical Review E **72**, 056303 (2005).

[7] F. Duan and C. A. Ward, Physical Review E **72**, 056302 (2005).

[8] C. A. Ward and F. Duan, Physical Review E **69**, 056308 (2004).

[9] C. Buffone, C. Minetti, L. Boussemaere, M. Roudgar, and J. De Coninck, Experiments in Fluids **55**, 1833 (2014).

[10] A. V. Hershey, Physical Review **56**, 204 (1939).

[11] A. Fathi Azarbayjani and A. Jouyban, Bioimpacts **5**, 29 (2015).

# Chapter 5

# Magnetic water treatment*

## 5.1 Introduction

The research on magnetic field effects on water originated decades ago [1-11]. The magnetic field effect on calcium carbonate deposition received the most attention due to the claim that the magnetic field influences the carbonate nucleation, thus reducing the scaling of pipes, boilers, and heat exchangers, leading to a major waste of energy [12]. The scaling in the pipes is due to the *reduction* in solubility of $CaCO_3$ with temperature. The magnetic field could encourage the precipitation of calcium carbonate in the bulk solution rather than encrustation with solid limescale, and the precipitation rate could be altered by the nature of the foreign ions present in the solution [12]. There have been many magnetic devices, the so-called magnetic water conditioners available in the market that claim to prevent scaling. It has been argued by Coey et al. that, the liquid-like nanometer-scale pre-nucleation clusters can be influenced by magnetic field [13], changing the crystal structure of the calcium carbonate precipitate. Claims exist for magnetic field changes to the physical properties of water, such as evaporation rate and specific heat and boiling point [14]. The magnetic field has also been claimed to change the surface tension [15] and viscosity of water as well [16].

Calcium carbonate is one of the naturally abundant minerals that has many applications in water treatment, the food industry etc. Calcite, Aragonite, and Vaterite are three polymorphs of calcium carbonate. Calcite is the most stable polymorph, and Vaterite is the least stable among the three polymorphs at ambient conditions. Aragonite exists as rhombohedral needle-like structures at high temperatures and pressures. It is metastable and converts

slowly to Calcite. Considering the various crystal properties of the polymorphs, an in-depth understanding of factors that influence the precipitation of polymorphs is important.

Some research studies investigated the magnetic field effect on the size and morphology of the precipitated crystallites. They found preferential precipitation of Aragonite rather than Calcite. Calcite turns into hard scale, whereas the Aragonite precipitates easily and washes away. It thus has the least contribution to the hard scale formation.

According to classical nucleation theory, important features of the crystallite precipitate completely depend on the solution conditions during the initial stages of precipitation – nucleation. It depends on the local concentration of dissolved ions that forms tiny crystalline nuclei, which have the potential to grow into crystallite in supersaturated solution[17]. Gebauer et al. [18] challenged the classical theory of nucleation by proposing the concept of thermodynamically stable pre-nucleation clusters, DOLLOPs in undersaturated $CaCO_3$ solutions. Demechelis et al. [19]found that stable prenucleation of calcium carbonate is in the form of ionic polymers with a chain of cations and anions bonded by ionic interactions. The clusters, also known as DOLLOPs (dynamically ordered liquid-like oxyanion polymers), are structurally dynamic polymeric chains of calcium cations and associated counterions. They are only a few nanometers in size, have no formal phase-boundary, and their interactions with the liquid medium are characterized as solute-like. Coey et al.[20] proposed an explanation of the magnetic field effect on the precipitation of $CaCO_3$ as an effect of proton transport and the formation of new ionic bonds, which are quasi-stable for hours. A momentary passage through a non-uniform magnetic field modifies the nuclear singlet: triplet ratio of transient proton dimer structures in the prenucleation cluster.

Magnetic water treatment uses magnetic fields to reduce limescale formation from hard water sources. Many magnetic water treatment devices / water conditioners is available in the market for over 70 years. However, they have been treated with skepticism by the scientific community due to the lack of its mechanism of operation. Despite the availability of many water conditioners and their uses, there is no agreed explanation of its mechanism of operations.

In our study, we have used a commercially available magnetic conditioner to explore the magnetic field effects on scaling. Mineral waters of different hardness were circulated through a magnetic conditioner several times using a peristaltic pump. We observed that continuous water circulation generates nanobubbles, and the zeta potential becomes more negative with more circulations. In addition, a systematic change in the Aragonite-Calcite peak ratio was observed for both soft and hard waters.

In another set of experiments, nanobubbles were generated using ultrasound sonication to check the correlation between the surface charge of nanobubbles and the $CaCO_3$ precipitation. We studied the production of bulk nanobubbles, stability, factors that influences its formation and how the dissolved salts inhibit the production of nanobubbles. This study aims study the magnetic field effects on scaling and to ascertain the effect of dissolved $Ca^{2+}$ cations on nanobubble stability in water and quantitatively confirm the presence of DOLLOP's.

## 5.2 Ultrasonic water treatment

Ultrasound has been used to precipitat solid materials using its unique cavitation mechanism. It has additional advantages such as rapid cooling rate and accelerated reactions that can produce some materials that conventional methods cannot achieve[21].

Many researchers over many years have studied the precipitation of calcium carbonate using ultrasound. Wang et al. [22] found that reaction conditions such as agitation and concentration of the reactants affect the nature of the precipitated polymorph. Price and coworkers[21] found that the precipitation of polymorphs depends on the degree of saturation, pH, temperature and additives such as polymers and metal ions. They observed the formation of Calcite at lower temperatures and Aragonite at a higher temperature. Unconventional methods such as stirring always favoured the formation of Calcite[21]. Stability was estimated by monitoring the evolution of the zeta potential of sonicated samples over a number of days.

### 5.2.1 Nanobubble production: Acoustic cavitation

Bulk nanobubbles are gas-filled spherical bubbles with a diameter of less than 1000 nm [23]. Bulk nanobubbles, filled with gases such as air, oxygen, hydrogen, carbon dioxide or another gas can be prepared by a range of methods, including gas injection [24], gas/liquid mixing[25], repeated compression [26], sonication[27], acoustic [28]or hydrodynamic cavitation [29], and electrolysis [30]. Some of these methods initially create microbubbles, which either coalesce and float away or collapse to leave nanobubbles behind. Properties of the nanobubbles depend less on the fill gas than on the surrounding liquid[31]. Nanobubbles form readily in water but not in organic solvents[32]. Nevertheless, after initial doubts, the existence of bulk nanobubbles is now well established by local microfluidic resonant density measurements[33], molecular spectroscopy[25], cryogenic [34,35] or liquid electron microscopy [36]and particle tracking measurements[25,31].

Applying ultrasound to water produces bulk nanobubbles[27,32]. Acoustic cavitation by ultrasound is used to produce nanobubbles throughout this investigation. This preparation mode prompts a need to understand the local events induced by ultrasound, to resolve the interaction between nanobubbles and the operating variables. External energy must be provided to produce a nanobubble, but apart from just energy, there need to be some other means to create a nanobubble; for example, in ultrasound sonication, periodic compression and rarefaction create a shock wave that gets the gas trapped and surrounded by a water molecule or mechanical stirring. The more hydrophobic the gas, the more nanobubbles are produced [23]. The zeta potential of the nanobubble water is -20 mV to -40 mV, depending on the type of gas dissolved and the pH of the water.

Ultrasound radiation propagates through the water as pressure waves, generating periodic regions of compression and rarefaction. When shearing forces greater than Van der Waals intermolecular attraction are generated during compressive cycles, small cavities, known as cavitation nuclei, are produced. Volatile compounds (i.e. dissolved gases) rapidly diffuse into the nuclei, which coalesce or expand and contract each oscillatory period. These bubbles

are transient or stable, depending on the frequency of oscillation and the source of ultrasound. Stable bubbles oscillate weakly for a number of cycles, or collapse and reform with each cycle as shown in figure 5.1. Transient bubbles, typically born at lower frequencies by ultrasound probes, predominate in this experimental setup. Their lifetime of a few oscillations ends in high energy collapse, releasing shockwaves, microjets, radicals and metastable nanobubbles [37]. The characteristic population of bulk NBs produced by acoustic cavitation is related to irradiation's frequency and power.

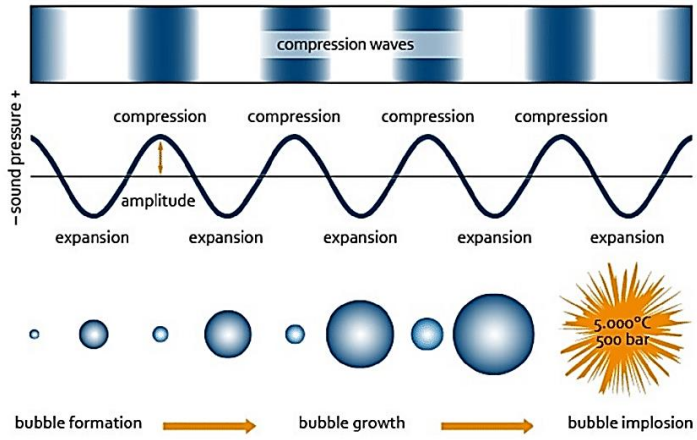


Figure 5. 1: Principle of ultrasound cavitation. The initiated bubbles grow due to evaporation and finally reach critical size (resonant) when it grows quickly and collapse violently[38]

The work by Kobayashi et al.[33] confirmed the physical presence of nanobubbles by the resonant mass method. A major dispute about nanobubble being confused with nanoparticles has been resolved by this method by observing a shift in the resonant frequency of a cantilever embedded in a microfluidic channel. The resonant frequency increases when a particle/entity of a small density than water passes through the microchannel. In contrast, the frequency decreases when a more denser particle/entity passes through it. The changes in frequency give the entity's mass, which makes it an accurate way to understand the entity's nature, particle or bubble.

Within the bulk of liquid, it is necessary to apply pressure to create a nanobubble as it requires energy to overcome the effects of surface tension. The surface tension or surface energy is the energy cost per unit area of producing a new interface. It gives information about how the strength of the intermolecular forces holds the molecules together. The stronger the intermolecular bonding in the material, greater the energy cost of producing a new surface and the higher the surface tension. Thus the pressure inside a bubble in a liquid is directly proportional to the surface tension and inversely proportional to the radius.

$$\Delta P = \frac{2\gamma}{R} \tag{5.1}$$

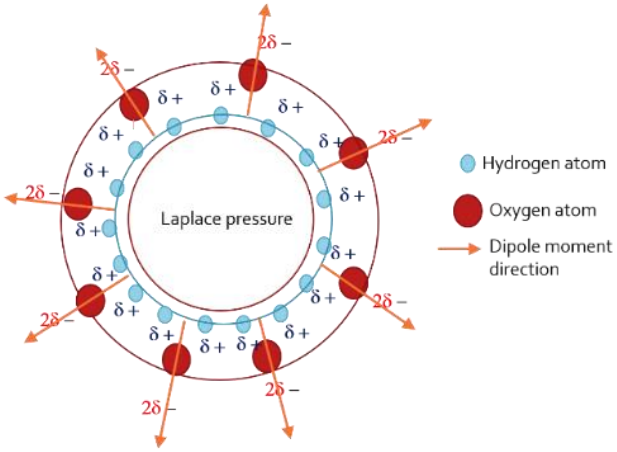


Figure 5. 2: Schematic representation of Laplace pressure inside a nanobubble[39]

where γ is the surface tension of the liquid and R is the radius of the nanobubble. The Laplace pressure inside a nanobubble of 100 nm radius is approximately 14 bar, which is really high. The solubility of a gas is directly related to the pressure, and thus smaller bubbles have higher gas solubility in the surrounding liquid due to the high Laplace pressure. The larger pressure favours the diffusion of gas out of the bubble. The curvature of the surface also creates a higher pressure differential across the surface[40]. Gas inside the bubble can be stable only if the surrounding liquid is supersaturated with gas against the external pressure.

A small perturbation can disturb the equilibrium and cause the bubble to grow and get removed from the solution through buoyancy or shrink[41]. The crucial question is how these nanobubbles are stable even under high Laplace pressure conditions. According to another hypothesis, to produce a stable nanobubble, there need to be enough ions formed outside the surface of the nanobubble to balance the Laplace pressure; otherwise, the gas inside the nanobubble dissolves immediately into the surrounding liquid within microseconds, according to Plesset and Epstein and Ljunggren et al. [42,43].

### 5.2.2 Characterization of nanobubbles; zeta-potential

Zeta potential is a characterization method to estimate the surface charge using the electrophoretic scattering method. A large positive or negative value of zeta potential indicates a stable nanosuspension through the repulsion of individual charged nano entities[44]. The magnitude of the zeta potential indicates the potential stability of the colloidal system. If all the particles in suspension have a large negative or positive zeta potential, they will tend to repel each other and there is no tendency to flocculate. However, if the particles have low zeta potential values, there is no force to prevent the particles from coming together and flocculating. The general dividing line between stable and unstable suspensions is generally taken at either +30mV or -30mV. Particles with zeta potentials more positive than +30mV or more negative than -30mV are normally considered stable.

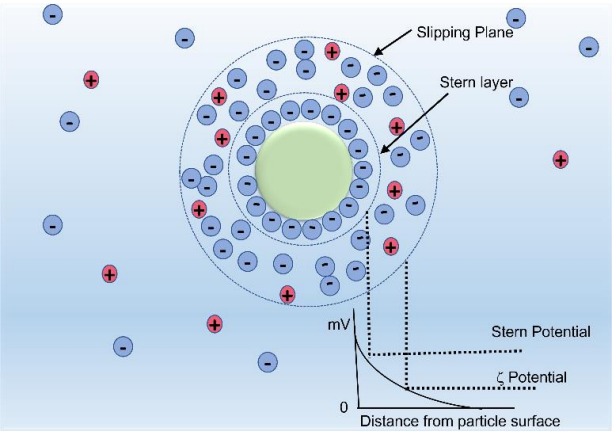


Figure 5. 3: Diagram of the electric potential and ion distribution as a function of distance from the surface of a charged body in dispersion, with the slipping plane, clearly marked [45]

The development of a net charge at the particle surface affects the distribution of ions in the surrounding interfacial region. The liquid layer surrounding the particle exists in two parts; an inner region called the Stern layer, where the ions are strongly bound and an outer, diffuse layer, a region where they are less firmly attached. Thus an electrical double layer exists around each particle. When a particle moves (e.g. due to gravity), ions within the boundary move with it, but any ions beyond the boundary do not travel with the particle. This boundary is called slipping plane. The potential that exists at this boundary is known as the Zeta potential as shown in Fig.5.3.

## 5.2.2 Stability of nanobubbles

The puzzling question about the longevity of bulk nanobubbles is still unresolved. There are a few proposed theories to explain the stability of bulk nanobubbles[25,28,46-49]. The two important aspects of the longevity of bulk nanobubbles are; the first one is the dominant Brownian motion and negligible buoyant force, which prevents the bubble from rising to the surface, and the second one is the stability against dissolution. The gas inside the bubble can move to the surrounding liquid and vice versa.

The Laplace pressure is higher inside the bubble than the surrounding liquid for smaller bubbles. Thus gas diffuses to the surrounding liquid to maintain the equilibrium. The loss of gas decreases the bubble size, resulting in higher Laplace pressure and thus high gas solubility. This leads to further loss of gas to the surrounding liquid. This positive feedback loop results in a sequent reduction of bubble size and the disappearance of small bubbles. If the liquid is supersaturated with the gas, the effect is opposite; gas diffuses into the bubble, increasing its size.

Thus far, there is no definitive explanation for the stability of nanobubbles in bulk. Yasui et al. proposed a dynamic equilibrium model due to a potential chemical gradient at the bubble surface, stemming from the permanent attraction of a partial hydrophobic skin, with minimum areal coverage of 50% of the gas molecules. There is no liquid flow at the surface and thus no net enthalpic or entropic change at equilibrium [50].

A widely accepted stabilizing mechanism is the existence of a negative surface charge at the gas-liquid interface, empirically identified by the zeta potential as shown in figure 5.2.

In aqueous solutions, the charge is thought to be derived from the preferential adsorption of hydroxyl anions, notionally supported by the increasing negativity of the zeta potential at alkaline pH. This is believed to be a consequence of the difference in hydration enthalpies of $OH^-$ and $H^+$ ions in bulk, or has alternatively been proposed as an attraction to the positively oriented water dipole at the interface [49]. Coulombic repulsion between the inner nanobubble surface and external anionic layer, illustrated in figure 5.2, works to counterbalance the eq.(5.1) with an external radial pressure

$$P = \frac{4\pi\zeta^2}{\varepsilon} \tag{5.2}$$

proportional to the square of surface charge density $\zeta$ , where ε is the dielectric function[51].

Nirmalkar et al.[28] studied the long term-stability of nanobubbles by observing the bubble diameter, bubble size distribution and its zeta potential over a period of time. The bubble size distribution retains its shape, but the number of bubbles decayed exponentially with

time, whereas the mean bubble diameter remains the same. The slow disappearance of nano-entities and constant bubble diameter led them to presume the surface charge is responsible for their stability [28]. However, the assumptions about nanobubble stability are still unproven. In summary, despite many years of studies to explain the stability of nanobubbles there is no accepted explanation yet.

## 5.3 Experimental methods

Different types of hardwaters have been used to understand how hardness or dissolved salts in water influence scaling; $CaCO_3$ polymorph precipitation and nanobubble formation. Millipore, mineral waters such as Volvic and Ballygowen, Evian, tap water, and Hillbrook (Dublin well water) with different hardness were used. Commercially available magnetic water conditioner which claims to prevent scaling uses tap water or well water in real-life situations. Thus using natural water sources such as well, tap water along with mineral water would give information about if there is any difference in precipitation of $CaCO_3$ when a magnetic field is present in these different sources of water. The hardness of water was measured at the Public Analytical Laboratory, Dublin. The hardness of $CaCO_3$ in mg/L increases in the order

**Millipore < Volvic < Tap Water < Hillbrook < Evian < Ballygowan**

Table 1: Table listing the relevant mineral composition in mg/L of the ultrasonically treated waters, with '-' indicating trace amounts, and 'x' indicating the data was unavailable. Conductivity is in mS/cm, with a standard error of ±0.01 mS/cm[52-55].

| Water | Millipore | Volvic | Tap | Hillbrook | Evian | Ballygowan |
|---|---|---|---|---|---|---|
| **pH** | 5.8 | 7.3 | 7.2 | 8.1 | 7.6 | 7.5 |
| **Conductivity** | >0.01 | 0.21 | 0.15 | 0.55 | 0.62 | 0.69 |
| **$CaCO_3$** | - | 61 | 59 | 350 | 290 | 317 |
| **Bicarbonate** | - | 74 | 36 | x | 360 | 400 |
| **Calcium** | - | 12 | 19.7 | 94.2 | 79 | 114 |
| **Magnesium** | - | 8.2 | 1.8 | 24 | 27 | 16 |
| **Sodium** | - | 12 | 7 | 18 | 6.9 | 15 |
| **Chloride** | - | 14 | 12.7 | 21 | 11 | 28 |
| **Potassium** | - | 6.3 | x | x | 1.1 | 3 |
| **Sulphate** | - | 8.5 | 23.48 | 65.84 | 13 | 15 |
| **Nitrate** | - | 10 | <6.64 | <6.64 | 0.91 | 9 |

### 5.3.1 Magnetic water treatment

The magnetic field effects on scaling and the dominant crystalline phase of the precipitate have been studied by a dynamic circulation of hard and soft waters, as shown in Fig.5.4. Two reservoirs were setup to produce a continuous flow of water and the circulation speed was controlled using a two-channel peristaltic pump. Two meters of tygon tubing were inserted into each channel of the pump, forming a closed-loop connected to 5 L reservoirs.

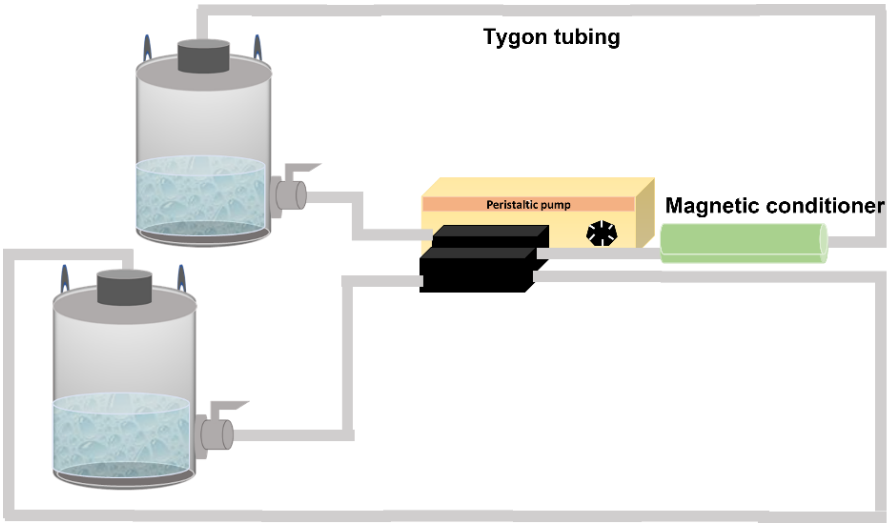


Figure 5. 4: Magnetic water treatment setup

A commercially available Ecocamel magnetic treatment device was attached to one channel while the other was used as control. The time taken for one passage was measured, and the experiments were repeated for 1, 10, 25 and 50 loops. Water is collected after each passage from both the channels and heated on a hotplate to collect the precipitate. The term ‘treated water’ has been used throughout his chapter for water passed through a magnetic treatment device (water conditioner). The properties of the circulated waters have been studied using zeta potential measurements, XRD and SEM. The magnetic field calibration of the magnetic treatment device is shown in Fig. 5.5

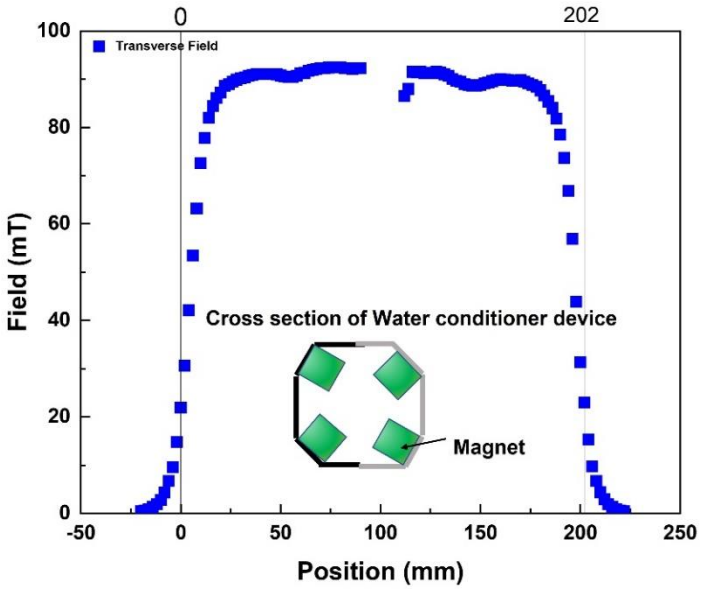


Figure 5. 5: Magnetic field calibration along the cross-section of the Ecocamel magnetic water conditioner

## 5.3.2 Ultrasound induced precipitation

The method of ultrasonic cavitation has been adopted to produce bulk nanobubbles and precipitate $CaCO_3$. Passing ultrasound through Millipore water generates nanobubbles through acoustic cavitation as explained in §5.2.1. Figure 5.6 shows the experimental apparatus. UP100H (100W, 30 kHz) from Hielscher Ultrasound technology with MS2 probe with a tip diameter of 2mm has been used to prepare the samples. Bulk nanobubbles have been produced in Millipore water of resistivity of 18.2 MΩ.cm and its lifetime has been monitored to understand its stability. A continuous 30 kHz ultrasound si§gnal was transmitted through a probe into the sample, and the temperature was monitored using a thermocouple throughout the experiment.

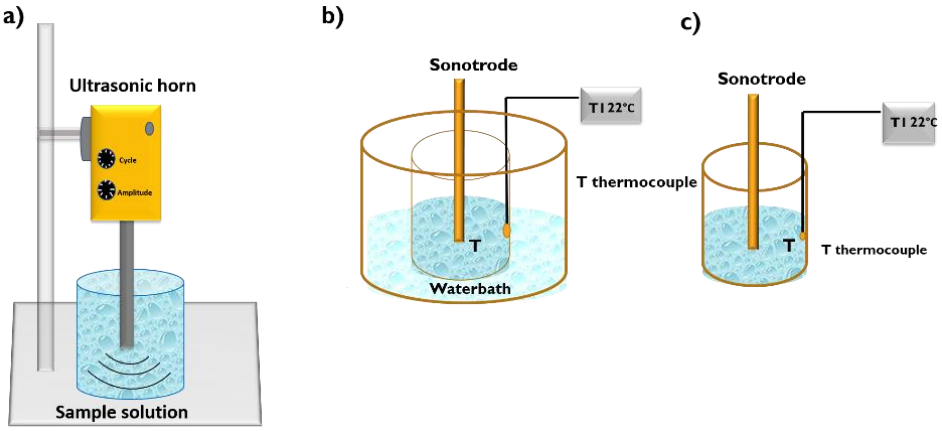


Figure 5. 6: a) Ultrasonic probe in sample solution; Experimental setup for the nanobubble production, b) Solution immersed in water bath c) without a water bath

The stability of a nanobubble population was quantified through triplicate 100-fold measurements of the zeta potential using the Malvern Zetasizer and DTS1070 cells. The stability was estimated by monitoring the evolution of the zeta potential of sonicated samples over several days. Conductivity and pH were monitored before and after all processes using a PC100 Cole Parmer handheld meter, calibrated fortnightly with a two-point system. For *in situ* conductivity measurements, the value measured by the Malvern Zetasizer was accepted. A Data Physics OCA Series measured the interfacial tension between air and both sonicated and unsonicated water samples given in §5.5.3. Dataphysics software uses the Young-Laplace fit to calculate the value of surface tension from the shape of the pendant droplet. The pendant droplet was dispensed at a rate of 1 μL/s from a Braun 1 mL disposable syringe with a tip diameter of 2.08 mm.

Two different vials with different diameters and initial volumes were selected for the sonication to understand how the sample volume affects the nanobubble formation since energy concentration varies with sample volume. 3 ml and 25 ml solutions were sonicated for 15 minutes and 40 minutes, respectively. The ultrasonication creates cavitation bubbles, and their

collapse creates high temperature and pressure inside the solution. Thus, monitoring the temperature is worthwhile while analyzing the stability of the nanobubbles.

A 15 mL vial of each mineral water sample was heated on a hotplate to understand the effect of heating during nanobubble formation and precipitation. Once a threshold of 50°C has reached the temperature is maintained between 50 - 60°C for 25 minutes followed by the the zeta potential, conductivity and pH measurements.

A water bath was constructed for temperature-controlled sonication, as shown in figure 5.6, with the small vial containing the sample within a large 600 mL beaker of cold water. Additionally, 3 mL samples of hardwater's were subjected to 25 min sonications reaching a higher temperature of 80°C. The precipitate was isolated by two methods: filtration and sedimentation. The precipitates were filtered using 0.2 μm pore papers immediately after sonication and then dried in an oven at 70 - 80°C. Sedimentation took several hours and up to a few days. The sedimented precipitate dried at either room temperature or between 70 - 80°C and the supernatant was collected by pipetting into a clean vial.

The sonicated samples were characterized by Zetasizer from Malvern Panalytical and the temperature during sonication was constantly monitored in real-time with a thermocouple as shown in Fig.5.6. This process was repeated for all six water samples listed in the order of increasing hardness to investigate the effect of dissolved salts and ionic concentration on nanobubble formation and stability.

Careful measurements of the mass of vials, water pre-sonication, supernatant and filter paper were taken at each juncture, enabling the normalized mass of the precipitate to be calculated. The pH and conductivity of the samples, pre- and post-sonication, were also monitored. Precipitates were harvested from evaporated hard water samples: at high temperatures and 80°C, as well as those isolated from sonicated samples and characterized by their respective XRD patterns.

## 5.4 Characterization methods

### 5.4.1 X- ray Diffraction (XRD)

X-ray diffraction (XRD) is a commonly used technique to study the crystal structure of materials prepared as thin films or powders. The basic mechanism of XRD is the elastic scattering of unpolarised X-ray radiation by the valence electrons. The model of X-ray diffraction is as was proposed by William H. Bragg and William L. Bragg and it is illustrated in figure 5.7. The incident radiation is reflected from semi-transparent atomic planes at an angle θ. The waves can interfere with each other. The condition for constructive interference is a phase shift of a multiple of 2π between two reflected waves. The scattered X-rays are detected at a large distance. The mathematical expression known as the Bragg Law is given by

$$n\lambda = 2d \sin(\theta) \qquad (5.3)$$

where n is a positive integer indicating diffraction order, λ is the wavelength of x-rays (e.g. Cu Kα is 1.540 Å), d is atomic lattice spacing and θ is the scattering angle. The crystal lattice gives a three-dimensional framework in space. The most general form of the crystal lattice is a parallelepiped, and its size and shape can be expressed with lengths of three axes, a, b, c and and angles between them α, β, γ. These six parameters are called ″lattice constants″,″unit cell parameters″or ″lattice parameters″. There are special relationships among the unit-cell parameters owing to the hsape and symmetry of the crystal lattice and the number of parameters also changes. An X-ray diffraction pattern is a series of peaks that correspond to constructive interference. Using equation 5.3, the out-of-plane lattice parameter (c) of the crystal unit cell can be calculated by taking the 2θ position of the (n00) peak. Further analysis of the peaks in the diffraction pattern can provide more information about the crystal structure of the material. Shifts in peak positions are related to the strain of the material, ratios of specific peak intensities

can be related to the chemical ordering out-of-plane in the crystal and FWHM of a peak can be related to the grain size τ by the Scherrer equation given by

$$\tau = \frac{K\lambda}{FWHM(2\theta)\cos(\theta_B)} \qquad (5.4)$$

where K is a shape factor (for thin films K = 0.9), l is the X-ray wavelength, FWHM (2θ) is the full width at half maximum of the peak at position 2θ and $\theta_B$ is the Bragg angle of the considered peak.

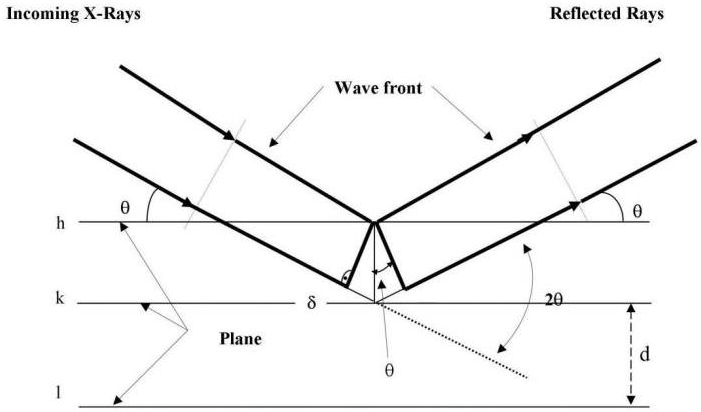


Figure 5. 7: Schematic diagram of Bragg diffraction Law. X-ray radiation incident at an angle θ is reflected from parallel atomic planes with spacing d.

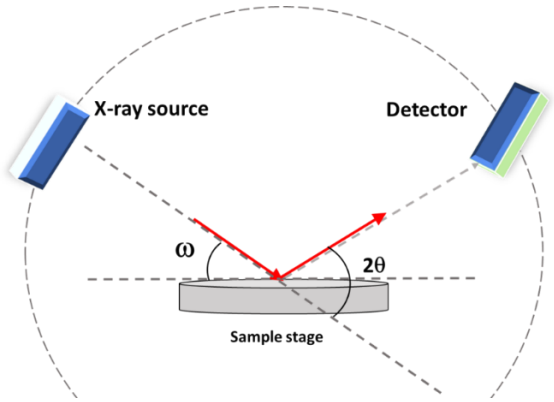


Figure 5. 8: Basic XRD measurement geometry: X-ray source, detector, and the sample stage.

A basic XRD measurement geometry is shown in figure 5.8. X-ray diffractometers consist of three basic components: an X-ray tube, a sample holder and an X-ray detector. X-rays are generated in a cathode ray tube by heating a filament to produce characteristic electrons. The characteristic X-rays are produced when electrons have sufficient energy to dislodge inner shell electrons of the target material. These X-rays are collimated and directed to the sample. The intensity of the reflected X-rays is recorded by a detector. A detector records and processes this X-ray signal and converts the signal to a count rate.

Our X-ray diffracted experiments were carried on the Philips Panalytical X'Pert Pro, which is equipped with multi-strip detectors to allow for the integration of each point along 2θ over the detector array for fast acquisition. The systems have a Cu-tube as the X-ray radiation source where the most intense emission line is Ka with wavelength l = 0:154056 nm. High quality diffraction patterns require fine powders, which are crushed from our bulk polycrystalline samples and then spread out and flatten on a glass slide.

### 5.4.2 Scanning Electron Microscopy (SEM)

An SEM is a type of electron microscope that uses an electron beam to scan the sample. The electrons that are backscattered, as well as the ones that are knocked off the near-surface region of the object, are detected and used to create high-resolution images. An electron source also referred to as an electron gun emits electrons that get accelerated by an applied voltage. Magnetic lenses converge the stream of electrons into a focused beam, which then hits the sample surface in a fine, precise spot. The electron beam then scans the surface of the specimen in a rectangular raster. Detectors collect the backscattered and secondary electrons. The corresponding signals are measured, and the values are mapped as variations in brightness on the image display.

The secondary electrons are more frequently used as read-out signal. They highlight the topography o the sample surface: bright areas represent edges while dark regions represent

recesses. As soon as microscopic information about the surface or near-surface region of a certain specimen is needed, SEM becomes a necessary tool. For that reason, the method finds applications in nearly every branch of science, technology and industry. The only clear challenge is that the viewed object should withstand the vacuum within the chamber and the bombardment by the electrons.

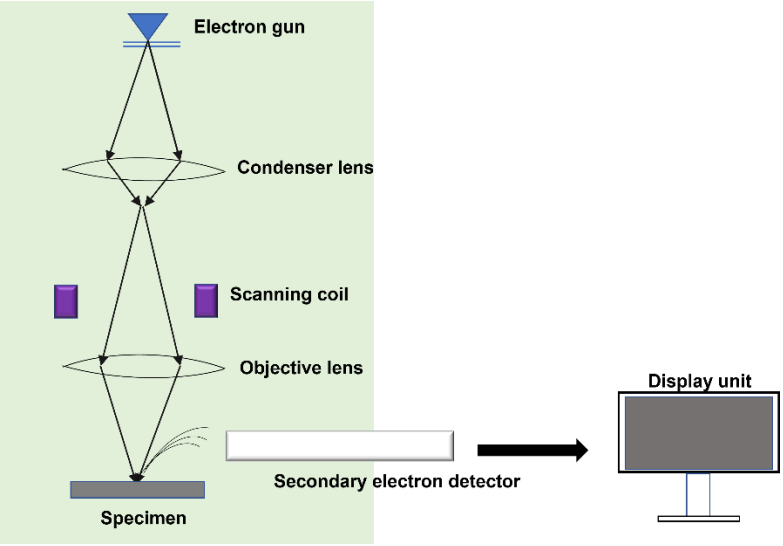


Figure 5. 9: SEM instrumentation

SEM images represent the morphology of a sample and can also reconstruct quasi-three-dimensional views of the sample surface. Therefore, the technique is basically used to obtain a high-resolution picture of surface features and allows conclusions about the distribution of different chemical elements within the sample. Modern SEMs can reach a resolving power better than one nanometer.

The SEM requires an electron optical system to produce an electron probe, a specimen stage to place the specimen, a secondary - electron detector to collect secondary electrons, an image display unit, and an operation system to perform various operations. Figure. 5.9 shows the basic construction of SEM. The electron optical system consists of an electron gun. a condenser lens and an objective lens to produce an electron probe. a scanning coil to scan the

electron probe, and other components. The electron optical system (inside of the microscope column) and a space surrounding the specimen are kept at vacuum.

### 5.4.3 Zetasizer

The MALVERN PANALYTICAL Zetasizer Nano series calculates the zeta potential using Henry equation from the measured electrophoretic Mobility. The electrophoretic mobility is obtained by performing an electrophoresis experiment on the sample and measuring the velocity of the particles. The velocity of a particle in an electric field is commonly referred to as its Electrophoretic mobility. With this knowledge, we can obtain the particle's zeta potential by applying the Henry equation. When an electric field is applied across an electrolyte, charged particles are attracted toward the electrode of opposite charge. Viscous forces acting on the particles tend to oppose this movement. When equilibrium is reached between these two opposing forces, the particles move with constant velocity. The particle's velocity depends on the following factors; the strength of the electric field or voltage gradient, the dielectric constant and viscosity of the medium, and the zeta potential.

The Henry equation is:

$$U_E = \frac{2\varepsilon\zeta f(k\,a)}{3\eta} \qquad 5.5$$

where: $\zeta$: Zeta potential. $U_E$ : Electrophoretic mobility. $\varepsilon$ : Dielectric constant. $\eta$ : Viscosity. $f$(Ka) : Henry's function. Two values are generally used as approximations for the f(Ka) determination - either 1.5 or 1.0. Electrophoretic determinations of zeta potential are most commonly made in aqueous media and moderate electrolyte concentration. f(Ka) in this case is 1.5, and is referred to as the Smoluchowski approximation. Therefore calculation of zeta potential from the mobility is straightforward for systems that fit the Smoluchowski model, i.e. particles larger than about 0.2 microns dispersed in electrolytes containing more than 10-3 molar salt. For small particles in low dielectric constant media f(Ka) becomes 1.0 and allows an equally simple calculation. This is referred to as the Huckel approximation. More

information about henrys function is given in Appendix B. The essence of a classical micro-electrophoresis system is a cell with electrodes on both ends to which a potential is applied. Particles move towards the electrode of opposite charge; their velocity is measured and expressed in unit field strength as their mobility**.**

## 5.4.3 Conductivity

The conductivity (σ) of a solution is measured by the reciprocal of the resistance between two electrodes, with an alternating voltage applied to circumvent electrolysis. It measures the flow of charge between the electrodes and is hence proportional to the concentration of free ions. Electrolyte concentration is typically related to conductivity by the quantity of total dissolved solids (TDS) such that

$$TDS\left[\frac{mg}{L}\right] = \beta\sigma\left[\frac{\mu S}{cm}\right] \tag{5.6}$$

for the units given. The proportionality constant known as the TDS conststant β, is empirically determined for a given solution as it depends on the nature of the electrolytic species, activity, valency, etc., and the ionic strength of the solution. A value of 0.65 is often appropriate for freshwater, but standard values range from 0.5 - 0.7[56]. More accurate values typically require a full analysis of the water in question to understand the correlation of the TDS value with the conductivity. The flow rate of ions in the solution has a marked dependence on its viscosity and the diffusion coefficient, which are temperature-dependent. For small changes in temperature, a linear approximation is used to extrapolate the specific conductance $\sigma_T$ at temperature T from the measured value at $T_0$

$$\frac{\sigma}{\sigma_T} = 1 + x\,(T_0 - T) \tag{5.7}$$

where x, temperature coefficient is usually 0.02°C $^{-1}$ [56]

## 5.5 Results and Discussion

### 5.5.1 Magnetic water treatment

#### X-ray diffraction (XRD)

The precipitates of Evian control and treated water after 1 and 10 passes have been analysed using XRD spectra given in Fig.5.10 a), b) and c), d) respectively. Figure a) and b) clearly distinguish the increase in [221] peak size for the treated sample. The Calcite peak [104] and the Halite peak [200] also disappeared after the treatment. This shows how the magnetic field prefers Aragonite even after one pass (10.2 seconds) through the magnetic treatment device. Calcite peak [104] of control Evian water after ten passes showed an increase even though it diminished for the treated water.

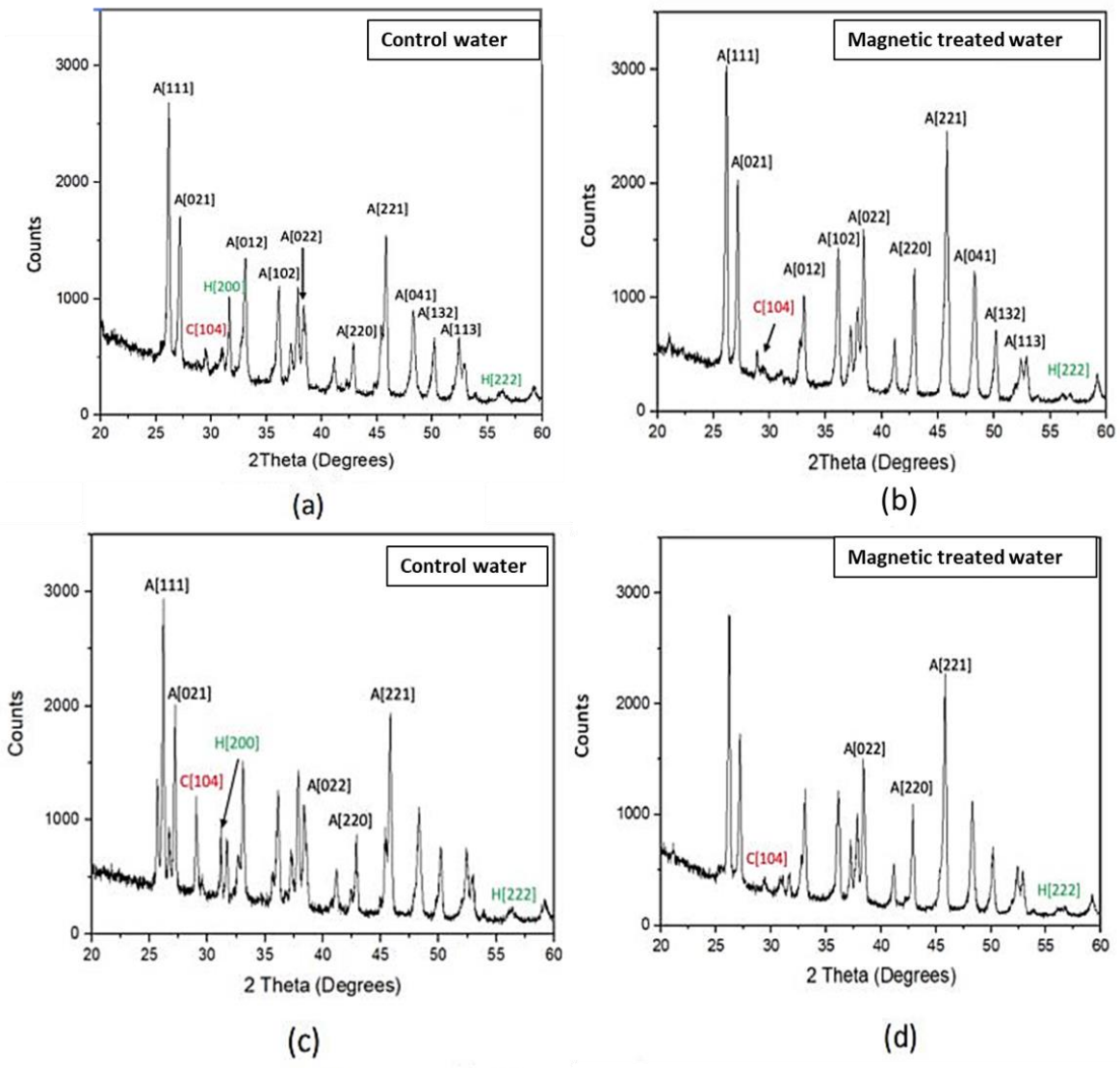


Figure 5. 10: XRD images of evian water a), b) control and treated water after 1 passes and c), d) control and treated water after 10 passes

XRD of Hillbrook control and treated water after 1 and 10 passes are shown in figure.5.11 a), b) and c),d) respectively. For Hillbrook control water, after 1 pass, the dominant phase was Calcite [104] peak . The intensity of [104] peak increased further for treated water and other Halite peaks shown in Fig.5.11 a) and b). There was a significant reduction in Calcite [104]

peak and Aragonite peak [111] is dominant after 10 passes. The intensity of Halite peak [200] increased for treated water in both the passes.

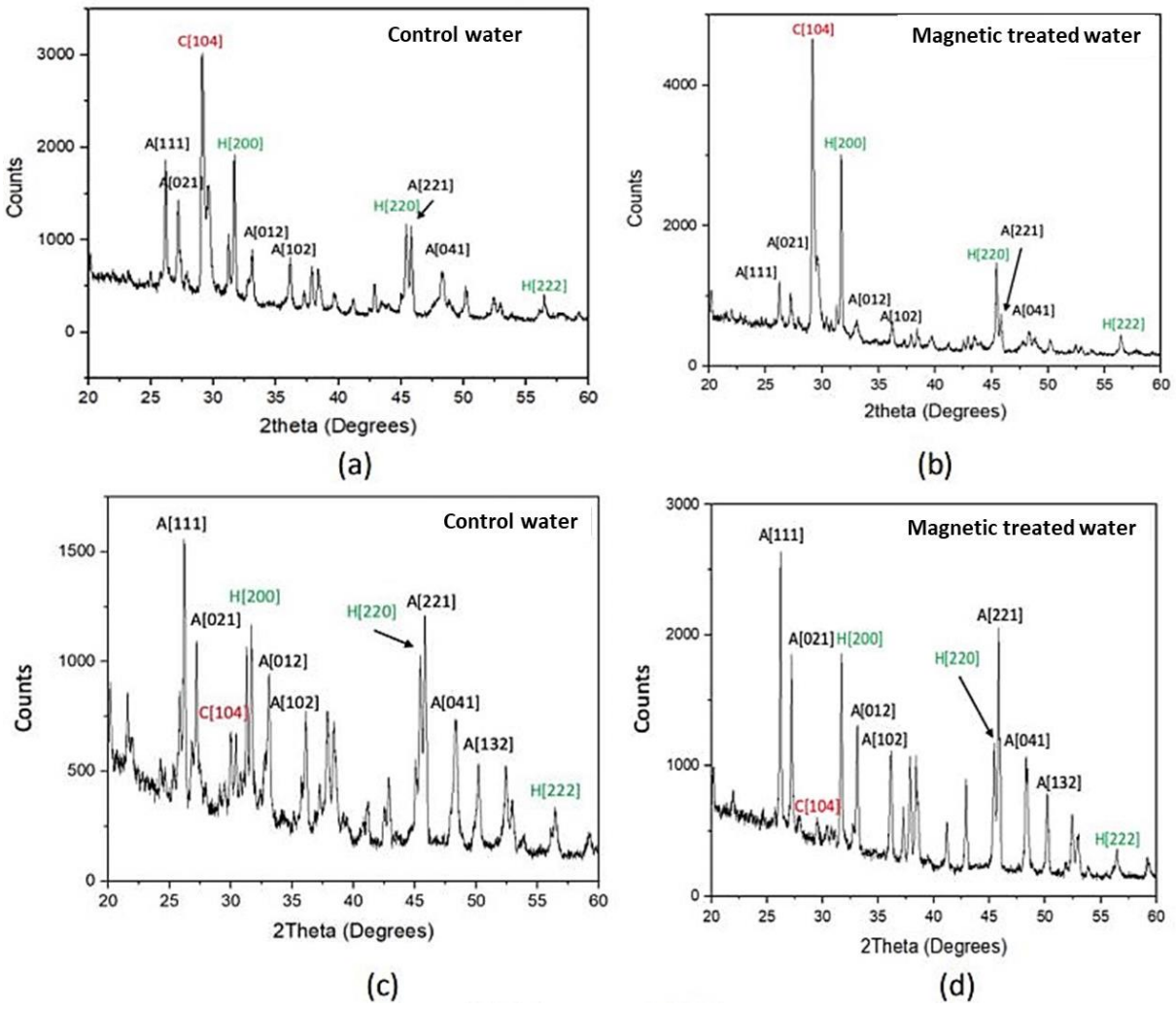


Figure 5. 11: XRD images of Hillbrook water a), b) control and treated water after 10 passes and c), d) control and treated water after 10 passes

For tap water, the dominant peak is Halite [200] which is significantly reduced after one pass, as shown in figure 5.12 a) and b). The Aragonite peaks are small in tap water in all the cases. There was a reduction of Aragonite peaks [111] and [102] peaks of treated water. The dominant phase is Halite [200] after 10 passes, contrary to 1 pass.

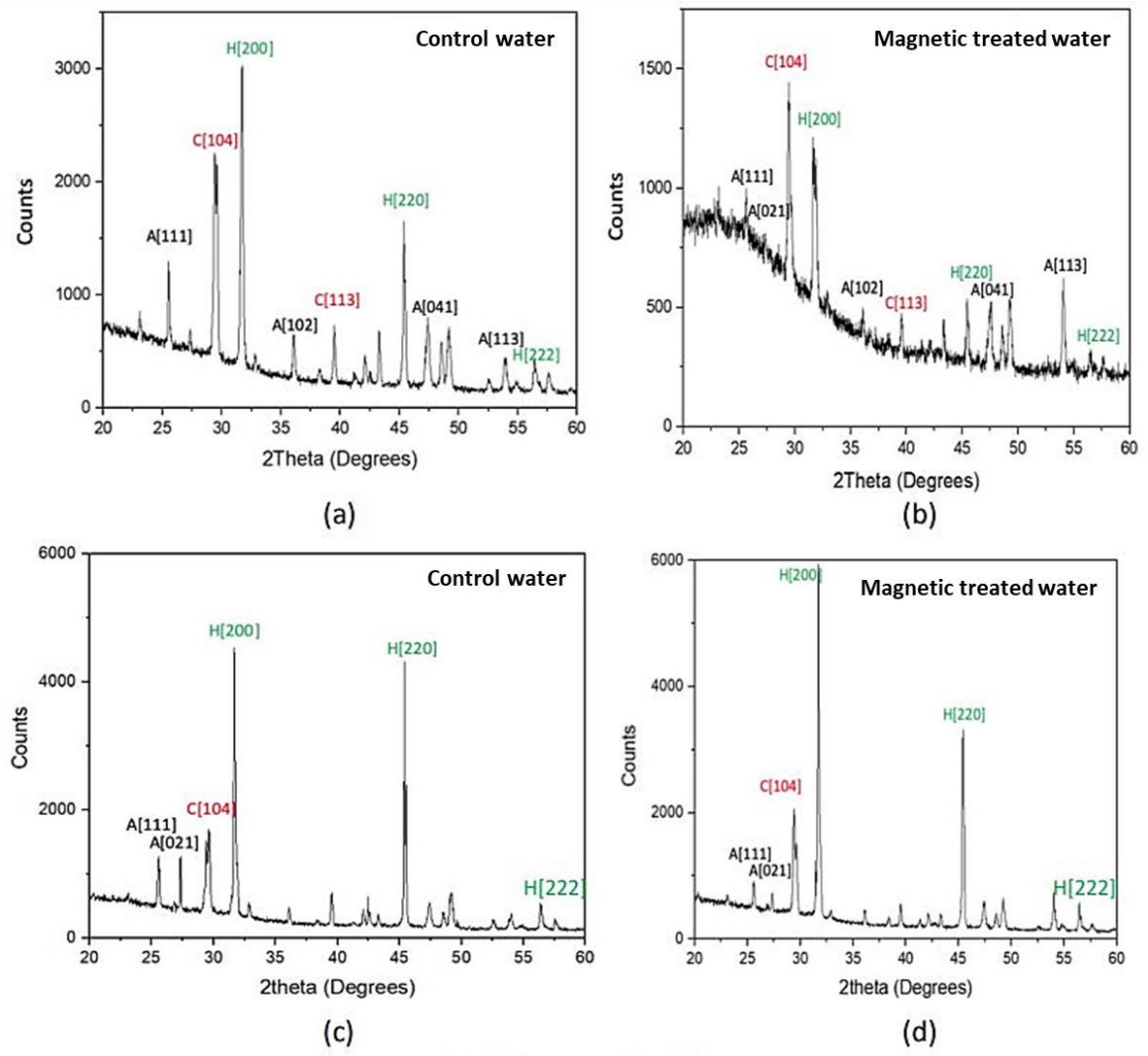


Figure 5. 12: XRD images of tap water a), b) control and treated water after 10 passes and c), d) control and treated water after 10 passes

For the soft water Volvic in Fig.5.13, the only Aragonite peak formed is [021]. The dominant phase of control water after 1 pass is Calcite [104] and almost all Calcite peaks are present. There are Halite peaks and Calcite peaks for both control and treated water after one pass. The Halite peak [200] becomes more dominant after treatment. The treated sample shows a clear reduction in all Calcite peaks, which implies the effectiveness of magnetic treatment in reducing the levels of Calcite in the precipitate.

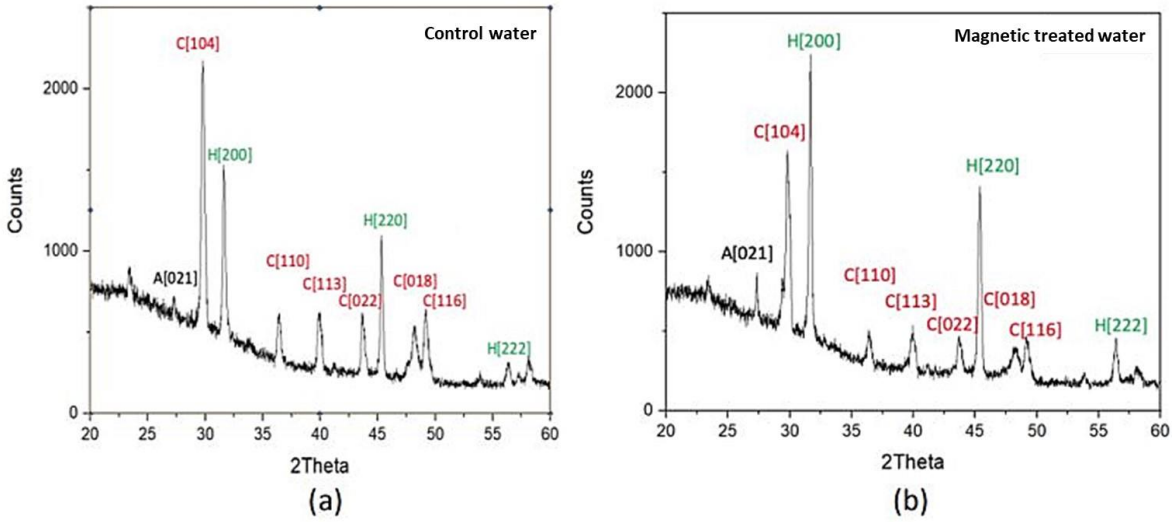


Figure 5. 13: XRD images of volvic water a) control b) treated water, after 1 pass

## Scanning Electron Microscopy

SEM images of hard water, Evian and soft water, tap water are shown in Fig.5.14, which gives information on hardness dependence on zeta potential in determining the crystalline phase of the precipitate. Fig 5.14 a) and b) shows a profound difference in the crystal size for control and treated hard water after 10 passes through the magnetic device. The long needle-shaped crystals are identified as Aragonite and the equiaxed crystals are Calcite. The needle-shaped Aragonite polymorph in figure 5.14b) indicates the magnetic field effect on preferential precipitation of Aragonite for hard waters, which XRD confirmed. Whereas, for soft water in Fig.5.14 c) and d), the precipitate is clumpier and contains more Calcite and Halite. The

crystallite size of the treated sample is larger than control water after 10 passes. It can be concluded that passing mineral water through the magnetic field affects the crystallite size of the precipitate and the type of polymorph precipitates depends on the hardness of the water.

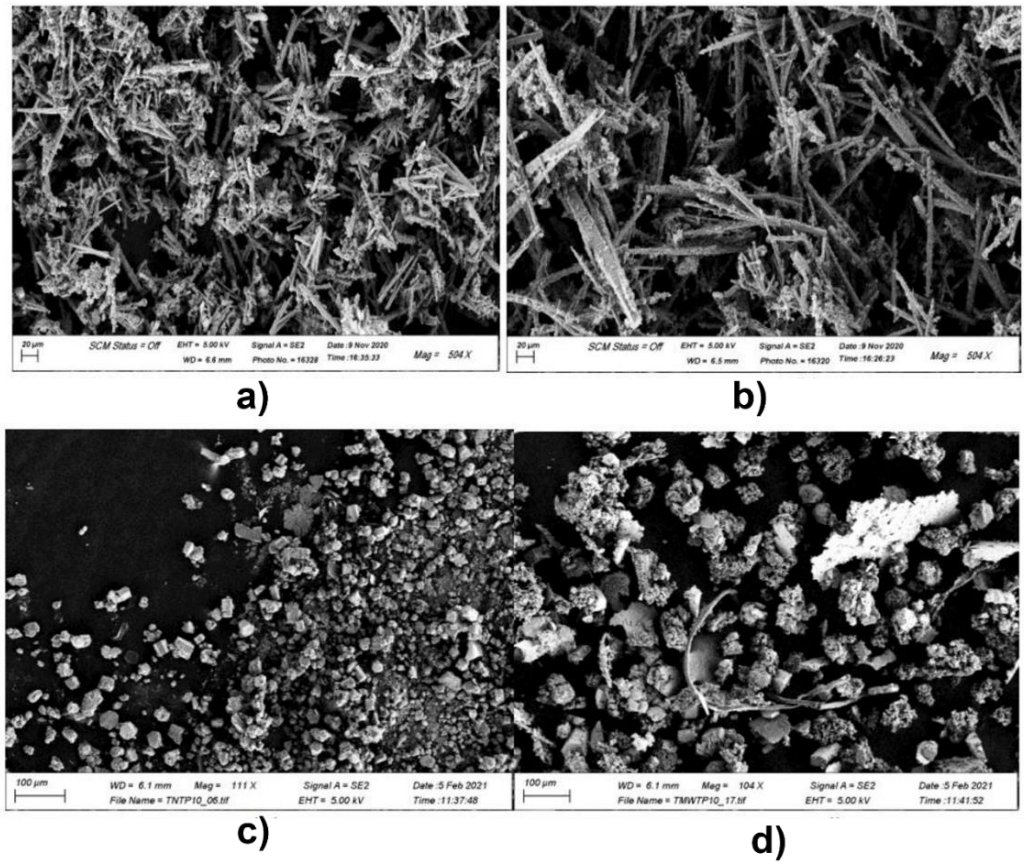


Figure 5. 14: SEM images of precipitates of Evian and tapwater after 10 passes. a) Evian control water b) Evian through magnetic treatment device (scale bar of 20 μm), c) tap control soft water d) tap through the magnetic treatment device (scale bar of 20 μm). The needle-shaped crystallites are Aragonite and the equiaxed crystallites are calcite.

It has been observed that the crystalline phase of the precipitate depends on the hardness of the water. Passing waters through a magnetic treatment device produces more Aragonite. It is confirmed that magnetic treatment retards Calcite production, thus reducing hard-scale formation.

## Zeta potential and conductivity

Circulation of mineral waters in a loop using a peristaltic pump produces nanobubbles characterized by the zeta potential measurements. The zeta potential becomes more negative with the number of passes, indicating the generation of nanobubbles after each pass. Following the previous observations, it is important to understand the generation of nanobubbles with the number of passes affects the phase of the crystalline precipitates. The highest value of zeta potential -32 mV was achieved after 50 passes for Volvic. The Zeta potential of the water passed through the magnetic treatment device and control have been monitored after 1, 10, 25 and 50 passes as shown in Fig.5.15. The hardest water used for magnetic water treatment was Evian, with a hardness of 290 mg/L.

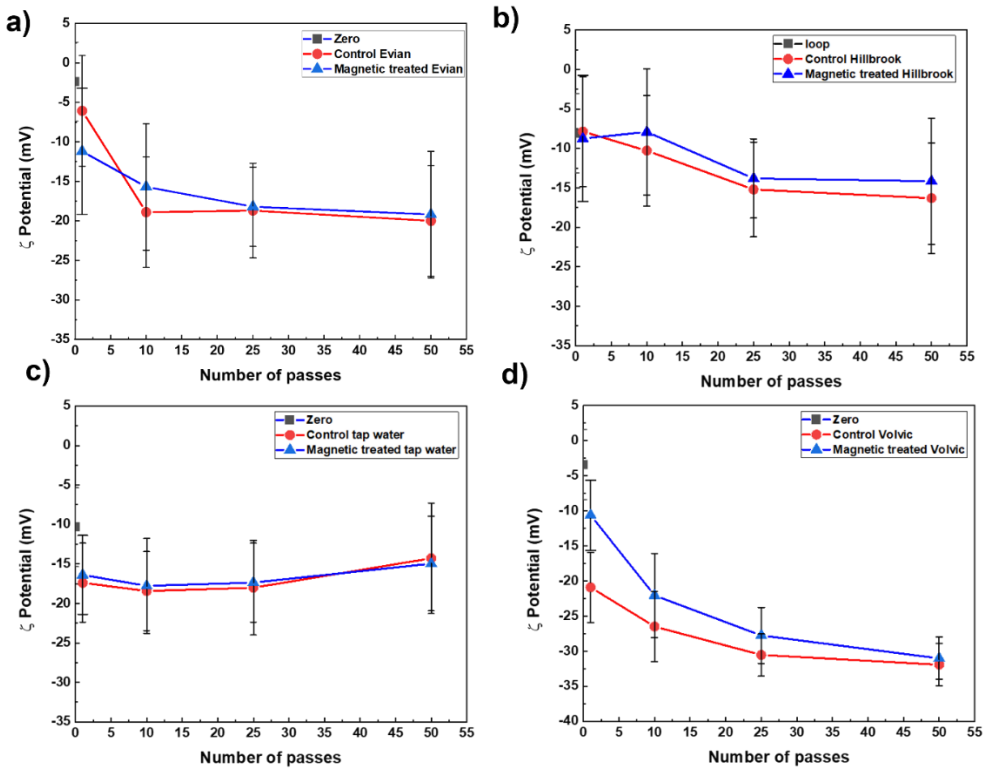


Figure 5. 15: Zeta potential after 1, 10, 25 and 50 passes of a) Evian b) Hillbrook well water, c) Tap water, d) Volvic. Zero (black) is the value of the zeta potential before passing waters through the peristaltic pump

The zeta potential value becomes largely negative even after one pass (except for Hillbrook). There is a definite indication that nanobubbles are somehow formed by pumping. Zeta potential drop of waters after passing through the treatment device in increasing order of hardness is, -20mV, -16mV, -7mV and -10mV, respectively.

The conductivity values of the mineral waters after 10 passes are shown in figure.5.16. The conductivity of the soft waters is much less than the conductivity of the hard waters.

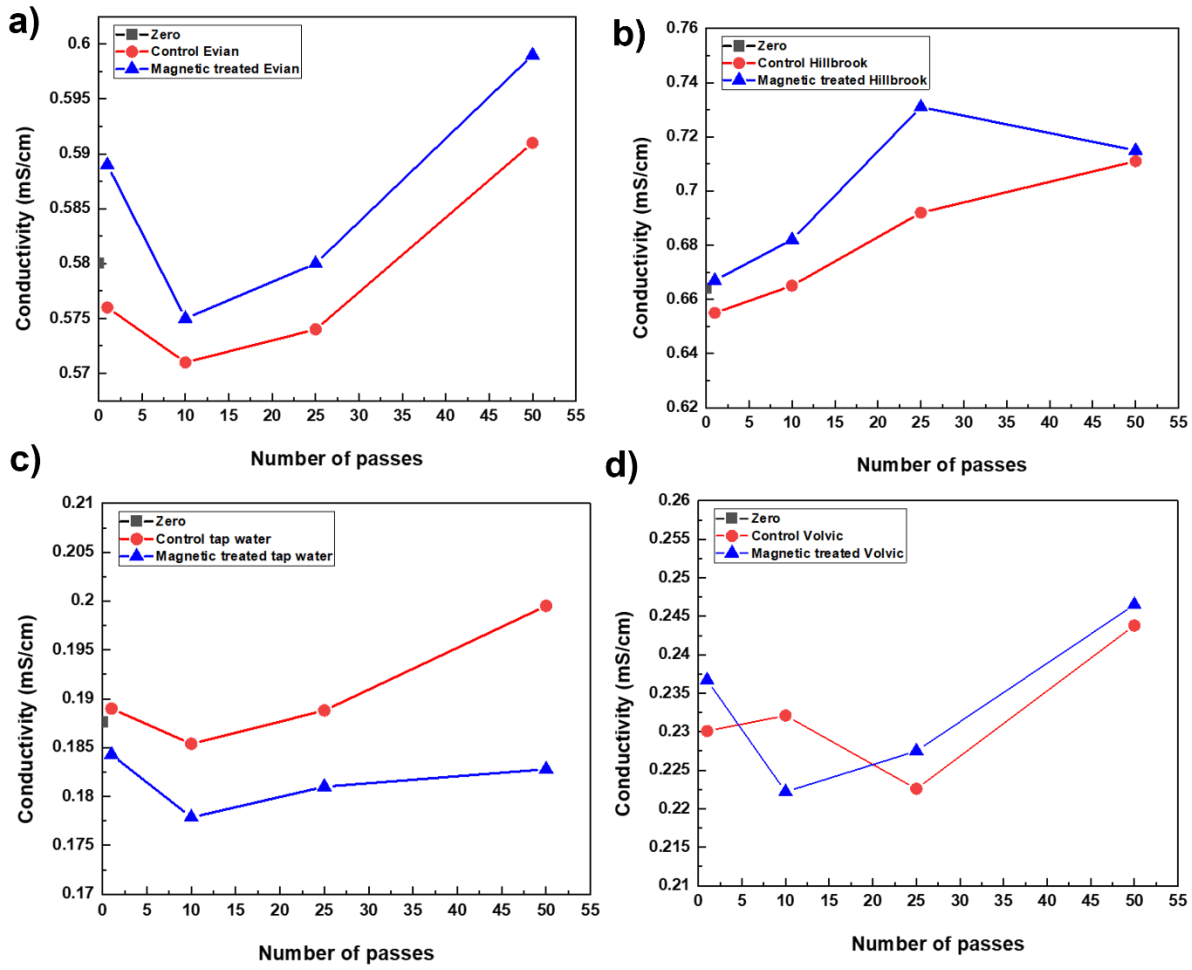


Figure 5. 16: Conductivity after1, 10, 25 and 50 passes of a) Evian b) Hilbrook well water, c) Tap water, d) Volvic. Zero (black) is the value of the zeta potential before passing waters through the peristaltic pump

The conductivity of treated hard waters, Evian and Hillbrook, were consistently higher than the control water, whereas it remained nearly the same for soft waters. The conductivity of all the control samples, irrespective of hardness, showed a higher value after 50 passes.

The precipitates of control water and treated water has been collected by heating the control and treated water after a number passes in the hotplate. The mass of the precipitates of the control water and the treated water after 1, 10, 25 and 50 passes of a) Hillbrook well water, b) tap water and c) volvic are shown in Fig. 5.17. The precipitate mass was higher for hard water than soft water and increased after 50 passes for both control and treated water.

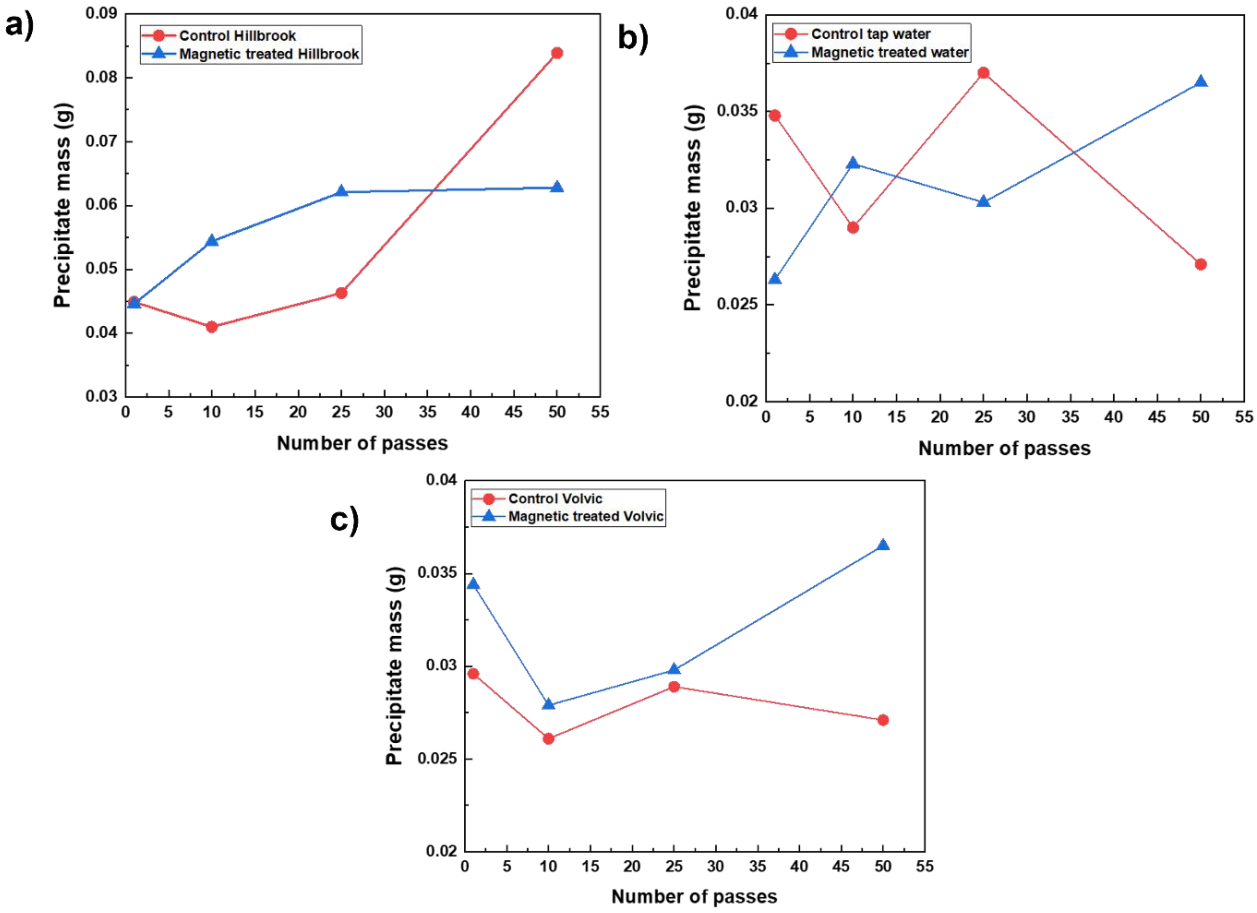


Figure 5. 17: Mass of the precipitate after 1, 10, 25 and 50 passes of a) Hillbrook well water b) Tap water, c) Volvic. Zero (black) is the value of the zeta potential before passing waters through the peristaltic pump

Ultrasound passing through water induces two types of processes depending on the hardness. One, ultrasound-induced nanobubbles in pure water and ultrasound-induced precipitation in mineral waters.

## 5.5.2 Ultrasonic Induced nanobubbles

The zeta potential measurements of the nanobubbles are shown in figure 5.18a. The zeta potential of Millipore water before sonication was -4 mV. The initial zeta potential of nanobubble water is -43mV. The nanobubbles formed were stable for over two days. The temperature increased to 70 ° C without a water bath during sonication, which is almost double that of a water bath. But for 15 ml solution, the temperature difference is 15 ° C. With a water bath, the temperature always remained at 35 degrees Celsius, as shown in figure 5.18b. The zeta potential of nanobubbles formed with a water bath showed the same zeta potential of -39mV. Nanobubbles formed in 25 ml water showed more stability than the 3 ml water since cavitation impact is inversely proportional to volume and temperature.

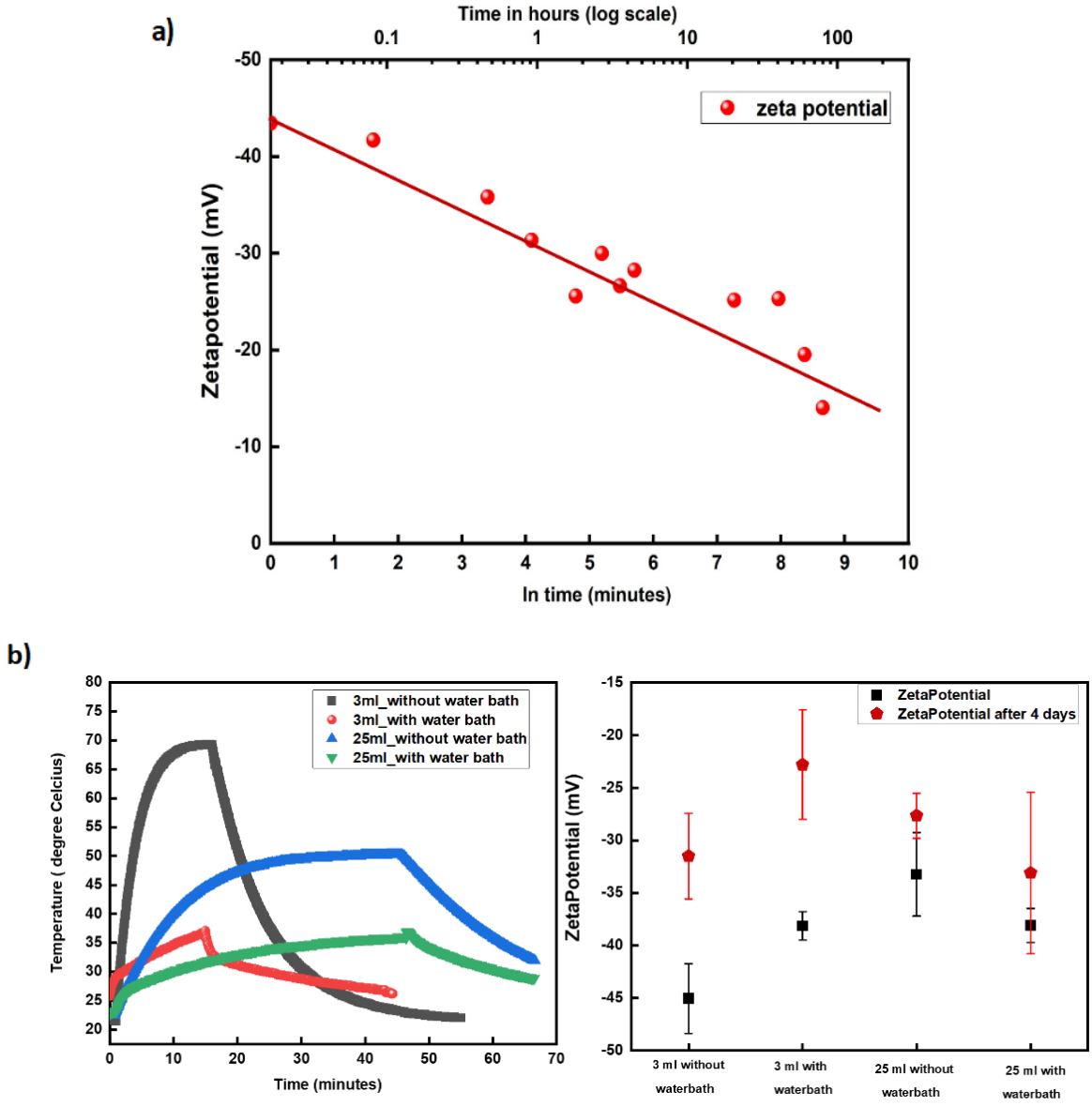


Figure 5. 18:a) zeta potential of nanobubbles with time, b) Temperature of the nanobubbles during the sonication and cooling process and it's corresponding zeta potential

The stability of nanobubbles in Millipore water was monitored by the decay of the ζ potential to its initial value over 5 days at an average rate of 0.31 mV/hour, shown in figure 5.18a. The high purity of Millipore deionized water permits the assumption that the ζ potential is a function of nanobubble formation alone. The decay in ζ potential likely stems from a combination of shrinking bubble radii and declining population[57]. The nanobubbles at neutral and alkaline pH are negatively charged by measurements of the zeta-potential (ζ = -20 to -40 mV) [28], but the pressure associated with the interface charge $P_q = -\varepsilon\varepsilon_0(\zeta/r^2)$ is much too small to compensate the Laplace pressure $P_L$.

### 5.5.3 Ultrasonic induced precipitation

The zeta potential of hard waters was quite different after sonication; the zeta potential showed more positive values with an increase in hardness which indicates that passing ultrasound to hard water/mineral water preferentially precipitates the dissolved salts compared to nanobubble formation. Millipore water with the lowest hardness showed the highest negative zetapotential and the hard water Evian shows the highest positive zeta potential as shown in figure 5.19 a). Hard waters turned into slightly milky after sonication. Thus the positive value of the zeta potential for hard waters could be attributed to the precipitation of dissolved salts during sonication. The zeta potential fell back to the initial values after 10 days.

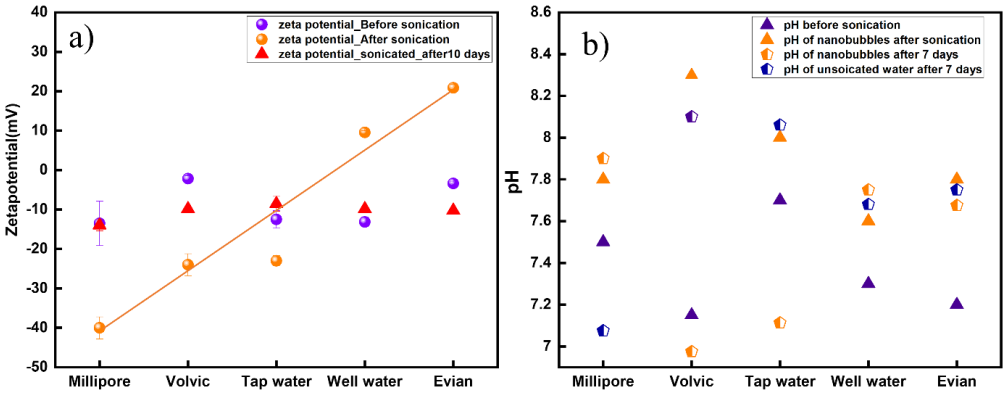


Figure 5. 19: The a) zeta potential and b) PH of various water before and after sonication. Orange line in a) shows the trend of zetapotential with hardness.

Irrespective of the hardness, the solution turned more basic after sonication. PH of the unsonicated water also turned basic after 7 days except for water, and the reason is unknown. The comparative effect of heat and a 25 minute exposure to ultrasound on conductivity for the different waters is illustrated in figure 5.20. These in situ measurements, also carried out for Millipore, corroborated with the reports by Yasuda et al.[23], that an equilibrium population of nanobubbles is established such that the ζ potential becomes approximately constant irrespective of irradiation time. This is shown in figure 5.21, as the ζ potential reaches -30 mV after 15 minutes and remains between -28 to -31 mV after that. Indeed, the temperature of the solution also reaches an equilibrium value and does not exceed 60°C throughout. All samples became more basic after exposure to ultrasound, most notably for softer waters: Millipore, Volvic and tap. A partial increase in pH can be attributed to the temperature-dependent solubility of $CO_2$ gas in Millipore. For harder waters - Hillbrook, Evian, Ballygowan, there was negligible change in the pH in the immediate aftermath of sonication. However, after the sedimentation of the precipitates, the supernatant solution of Evian and Ballygowan showed an increase in basicity compared to softer waters.

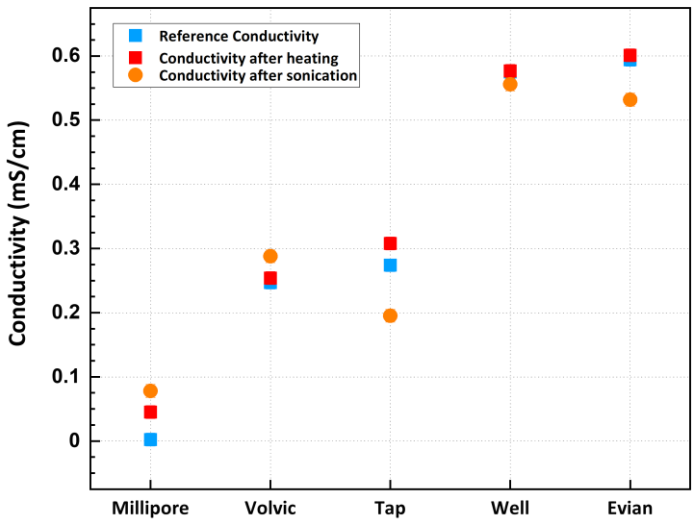


Figure 5. 20: Conductivity of various water samples in the order of increasing hardness

Controlled heating experiments were beneficial to differentiate the effects of ultrasound and heating. The pH increased for all waters post-sonication compared to heating which was almost negligible. Conductivity remained approximately constant for soft waters but decreased for hard waters post-sonication.

Zeta potential of sonicated soft waters, tap, Millipore, Volvic showed increasingly negative values, while hard waters were driven toward 0 and beyond, to increasingly positive values. Although the magnitude of change in ζ potential of tap water was negligible after sonicating, is aligned with the trending shift relating to water hardness and zeta potential.

Aside from Millipore, Volvic and tap water also indicated nanobubble formation evident from their ζ potential values. Hard mineral waters Evian and Ballygowan achieved positive ζ potentials in the range 18 - 25 mV. This measurement was associated with considerable precipitation. In-situ monitoring of ζ potential showed a clear switch to a positive value after ten minutes when the threshold temperature crossed 45°C depicted in figure 5.21.

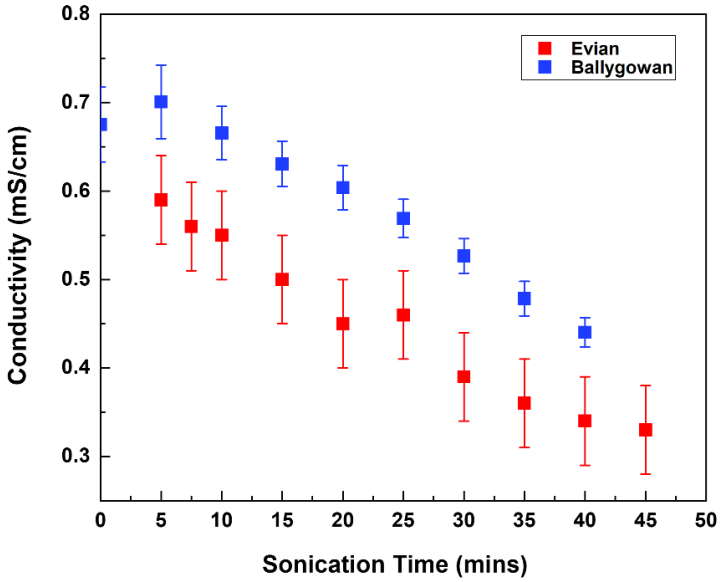

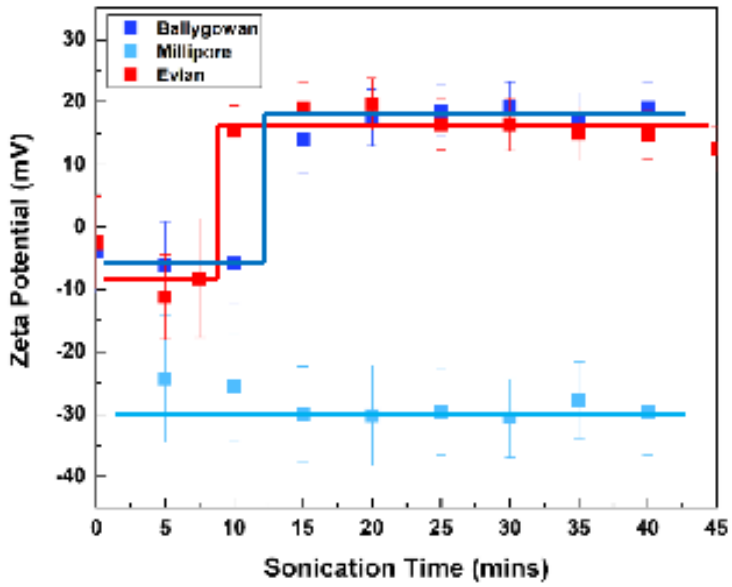


Figure 5. 21: Conductivity and zetapotential dependence of Evian and Ballygowan on sonication time.

This positive ζ potential indicated the presence of precipitates which are stable with time. The ζ potential decays from 18 mV to 9.6 mV over a period of 46 hours for Evian, and Ballygowan from 22 mV to 11 mV over a period of 73 hours, yielding average decay rates of -0.18 mv/hour and -0.13 mV/hour, respectively. Suspended precipitate induced by heating did not exhibit a positive ζ potential. Moreover, for temperature-controlled sonication of Ballygowan and Evian, maintaining the temperature below 40°C prevented the onset of precipitation and ζ potential remained positive.

Only Evian and Ballygowan exhibited a marked fall in conductivity post-sonication, while this change was negligible in other samples. This reflects the decrease in the concentration of mobile dissolved ions such as $Ca^{2+}$, as consumed in the precipitation of calcium carbonate. Although precipitation can occur via heating, temperatures approaching 80°C are required. The temperature during sonication remains below 60°C, insufficient to promote precipitation in the absence of ultrasound.

Precipitation was observed once the water's temperature reached a threshold temperature of 45°C, coinciding with the switch in ζ potential from negative to a positive value whereas the conductivity fell in approximately linearly fashion throughout as shown in figure 5.21. The slope of the decrease in conductivity was relatively consistent for both Evian and Ballygowan. For Evian, it decreased at -6.7 ±0.4 μS/cm $min^{-1}$ and for Ballygowan, -7.1± 0.5 μS/cm $min^{-1}$.

Measurements of the interfacial tension before and after sonicating, exhibited a very small decrease post-sonication when controlling for temperature. Untreated waters had a surface tension between 71.6 - 71.9 $mNm^{-1}$, as shown in Fig.5.22, agreeing with standard values for the air-water interface. No consistent changes were observed and were mostly confined within the experimental range of uncertainty. Millipore showed no discernible change, while Evian showed the only notable, if slight, decrease post-sonication. This cannot be attributed to the presence of NBs as Millipore did not exhibit any change and is more likely linked to the suspended precipitate.

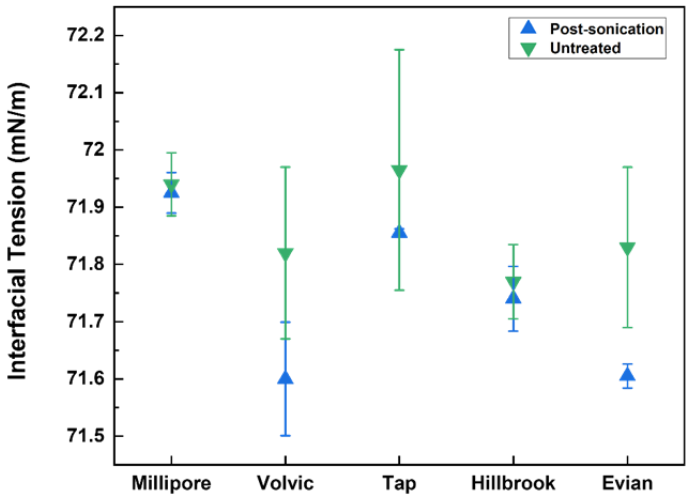


Figure 5. 22: Interfacial tension of various waters before and after sonication

Initial application of continuous wave ultrasound to 15 mL Ballygowan and Evian hard water samples for 40 mins resulted in significant precipitation and a drop in conductivity. One of the

primary effects of ultrasound is accelerating nucleation, which promotes the precipitation of small crystallites. Secondary sonication of the supernatant yields negligible $CaCO_3$ precipitate. There is some fraction of calcium in the unperturbed sample, which does not contribute to the initial conductivity after first sonication- a qualitative indication of the existence of $CaCO_3$ DOLLOPs (Dynamically ordered liquid-like oxyanion polymers). The sonicated supernatant showed a positive zeta potential in most of the cases. Even though the concentration of ions is depleted during the first sonication, secondary sonication showed an increase in conductivity.

As previously observed, the pH increased following a second sonication to a lesser degree. However, in contrast to previous results, there was an appreciable increase in the conductivity. This was also observed for some temperature-controlled sonications and could give information about the presence of DOLLOPs in Evian and non-classical crystallization pathways. It also suggests the formation of weakly associated ionic complexes after initial sonication, which are then dissociated by a secondary ultrasonic treatment.

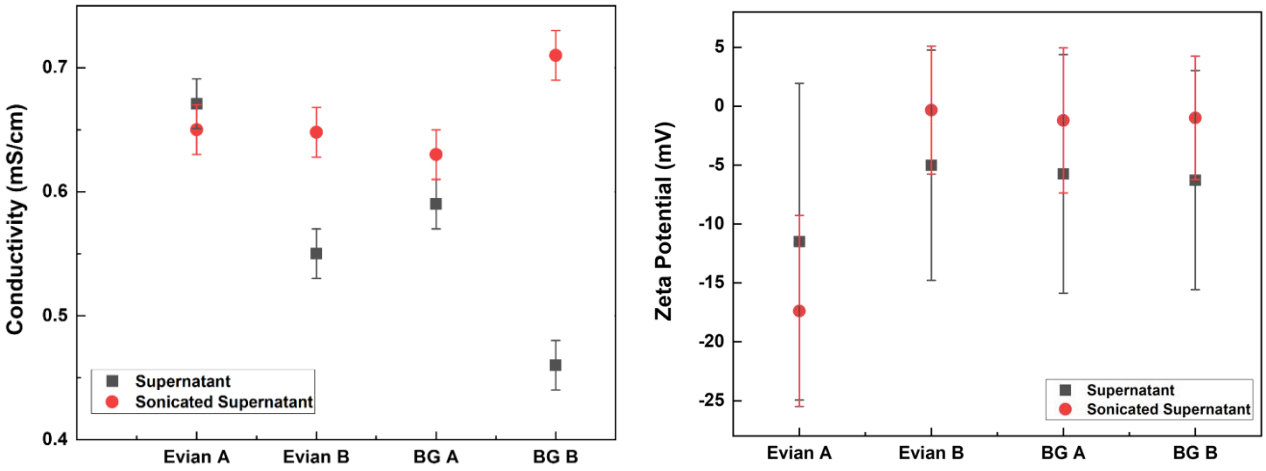


Figure 5. 23: conductivity and zeta potential of primary samples of Evian, Ballygowen and their supernatant solutions.

Sonication of the supernatant showed an increase in conductivity, resulting in a complex equilibrium between remaining $CaCO_3$ in amorphous, DOLLOP and precipitated salts and some possible redissolution of crystallized $CaCO_3$.

The change in concentration of solvated calcium cations could be gauged by the conductivity, and thus possible to quantify the fraction of calcium held in the charge-neutral DOLLOPs. Total Dissolved Salts (TDS) can be attributed to the removal of $CaCO_3$ in solution. Secondary sonication and the incurred increase in conductivity (and hence increase in TDS) with no visible precipitation inferred an even higher ceiling of $CaCO_3$ held in DOLLOPs.

The secondary ultrasonic treatment appears to destabilize weak ionic complexes formed in the solution after the initial sonication. In addition, the free calcium ions, once dissociated, can contribute to the conductivity of the solution. Water analysis on Evian included the initial TDS and conductivity, and so the proportionality constant β was calculated using eq.(5.6). For the linear approximation outlined in equation 5.6 with σ = 541±10μS/cm at 20 °C and TDS of 340±5mg/L

$$\sigma_{25} = {}^{601\mu S}/_{cm}. \quad \beta = 0.56 \pm 0.01 \tag{5.8}$$

Table 3: Table giving sample graphically estimated conversion factors for a given conductivity $\sigma \pm 10$ μS/cm—*SN* subscript indicating supernatant values, i.e. solution after extraction of the precipitate.

| Water | $\beta$ | $\sigma$ | TDS (mg/L) | $\sigma SN$ | $TDS_{SN}$ (mg/L) |
|---|---|---|---|---|---|
| Evian | 0.56 ± 0.01 | 604 | 340 | 218 | 122 ± 6 |
| Ballygowan | 0.55 ± 0.02 | 690 | 380 | 481 | 265 ± 11 |

An estimate of the concentration of $CaCO_3$ in DOLLOPs, with sample calculations shown in table (3). The expected precipitate mass was greater than the change in TDS in all tested

samples. This supports the DOLLOPs hypothesis, already indicated qualitatively by the increase in conductivity of the supernatant after a second sonication.

## X-ray diffraction

Precipitate extracted from a 25-minute standard temperature (60°C) and high temperature (80°C) sonication exhibited a mixture of Calcite and Aragonite phases for $CaCO_3$ as shown in figure. 5.24. The precipitate collected from the sediment of the sonicated sample and left to dry under air or in an 80°C oven. High-temperature evaporation of unsonicated Evian showed a strong Aragonite composition and a smaller fraction of NaCl Halite. Comparison of the relative intensities of Calcite [104] and Aragonite [221] characteristic peaks clearly identify Calcite as the dominant phase of the sonicated samples. It agrees with the work reported by Santos et al. [58] discussing that a sample evaporated at a higher temperature adheres to the preferential formation of Aragonite. An unidentified peak occurred at 40°, also appearing at a much higher relative intensity in the evaporated supernatant, not distinguishable in the untreated sample, which has smaller peaks in this region attributable to Aragonite.

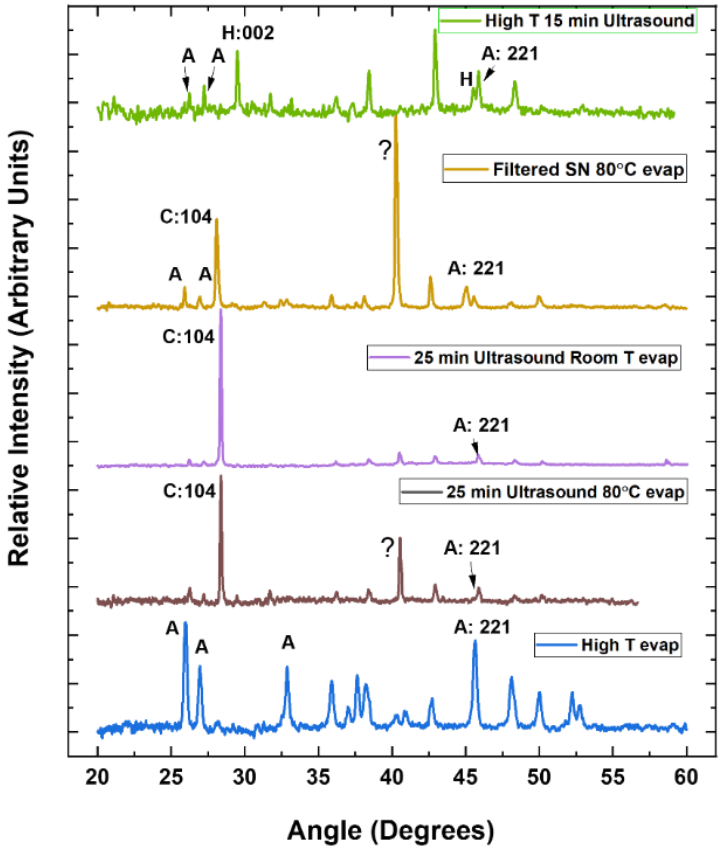


Figure 5. 24: XRD patterns of precipitate samples collected from Evian. Characteristic Calcite 104 peak at 29°and Aragonite 221 at 46°labelled. Halite 002 peak is at 32°. Significant peaks denote Calcite, Aragonite and Halite as C, A, H, respectively

Only a 3 mL volume of water was used to achieve a higher temperature during irradiation: hence the volume of precipitate extracted was proportionally lower. As a result, the intensity of the XRD pattern was limited and thus more difficult to index. However, low-intensity Halite (NaCl) peaks [002], [022] were observed as more heat was introduced to the system, coincident with the disappearance of the Calcite [104] peak, which typically forms more slowly at room temperature.

As for Evian, a high-temperature evaporation yielded a close to pure Aragonite pattern, and no Halite peaks were identifiable. A controlled evaporation at 80°C, replicating the evaporation

temperature of the sonicated sample, consistently showed a higher proportion of Calcite than the high-temperature evaporation and a reemergence of the Halite [002] peak. The ratio of Aragonite to Calcite was strongly variant however, highlighting the metastability of Aragonite and the sensitivity of the phase to ambient conditions as well as their effect on the evaporation rate.

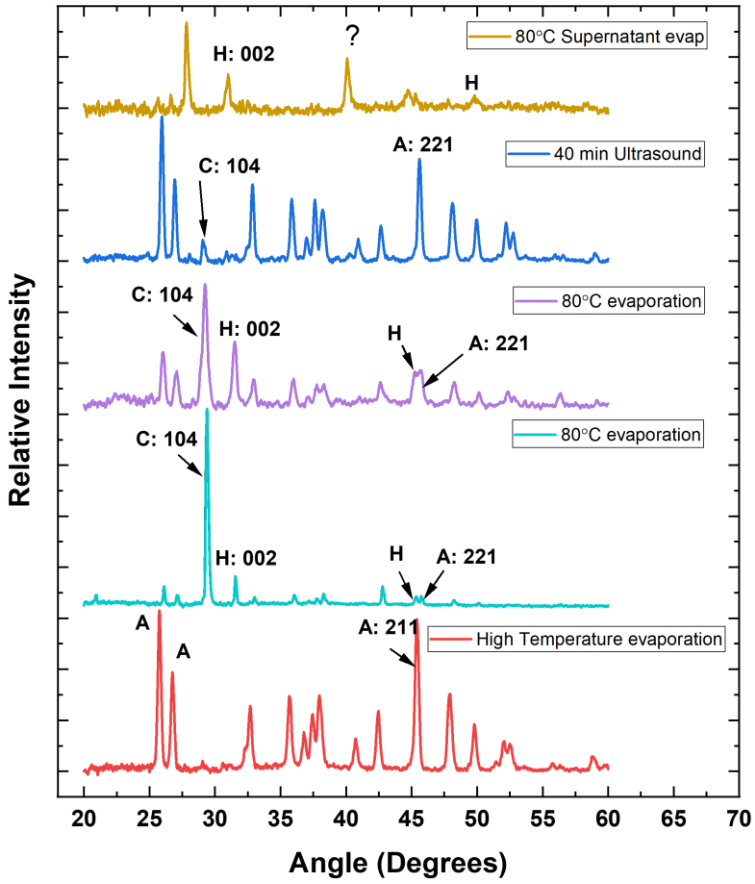


Figure 5. 25: XRD patterns of precipitate samples collected from Ballygowan. Characteristic Calcite 104 peak at 29°and Aragonite 221 at 46°labelled. Halite 002 peak is at 32°. Significant peaks denote Calcite, Aragonite and Halite as C, A, H, respectively

Calcium carbonate precipitation of Ballygowen mineral water during 40-minute ultrasound and evaporated at 80°C showed no Halite and a highly diminished Calcite [104] peak, otherwise

reproducing a strong Aragonite pattern. This result agrees with literature reporting preferential crystallization of Aragonite by higher temperature ultrasound[21]. As for Evian, evaporation of the supernatant, which was isolated by sedimentation, once again yielded an unidentified peak at 40°, as well as peaks Halite. This method of removing the precipitate appears more effective, as calcium carbonate peaks are not readily distinguishable.

## Scanning electron microscopy

SEM images in Fig.5.26 are of precipitate extracted from a high conductivity supernatant of Evian post-secondary irradiation. The precipitate was extracted using the same method as Ballygowan, outlined below. Aragonite is immediately identifiable by its well-defined rod-like structure, most of which are several micrometres long and with radii < 0.5 μm. Dispersed among the needles, there were a few examples of almost clump-like structures: a mixture of rhombohedral Calcite and some Halite.

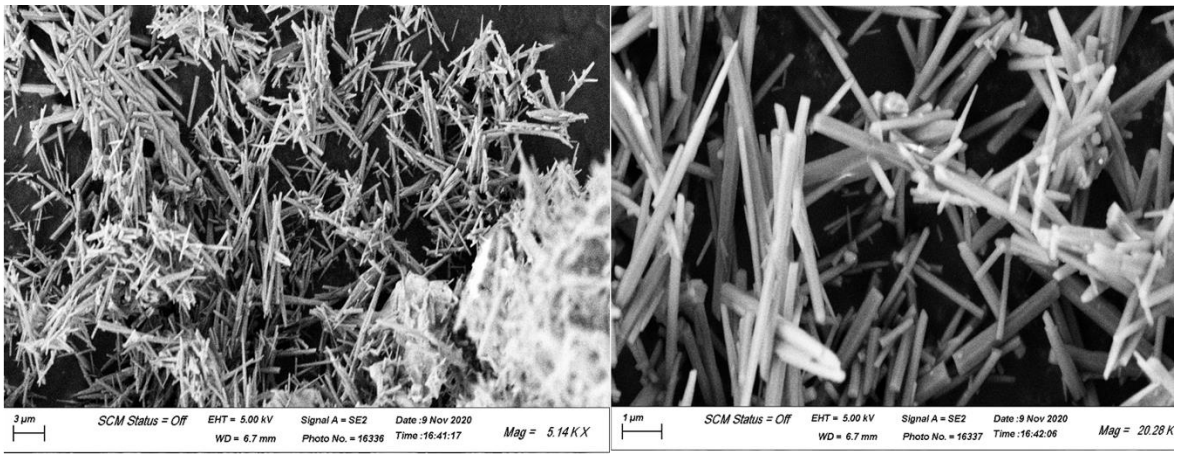


Figure 5. 26: SEM images of precipitate extracted from Evian after sonication. The needle-shaped crystallites in the figure show the presence of aragonite. The figure on the right panel is zoomed image with the scale bar 1μm

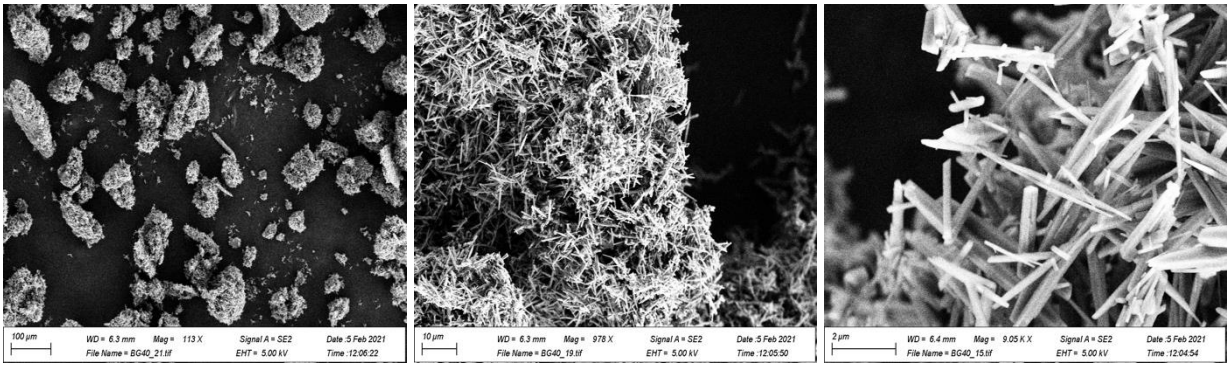


Figure 5. 27: SEM images of precipitate extracted from Ballygowan after sonication. The needle-shaped crystallites are aragonite.

The SEM images in figure 5.27 for the sonicated ballygowen showed clumps of Aragonite needles only were observed, with no evidence of Calcite nor any other mineral structure. The needles aggregated in distinctive clumps and once again were typically less than 10µms long, with a radius of approximately 0.5-1 µm. A more prolonged exposure to ultrasound in the case of Ballygowan resulted in a higher composition of Aragonite to Calcite than for Evian. The method of collecting a sample to be x-rayed for Evian likely resulted in a higher Calcite yield than anticipated due to a faster evaporation rate for the drops deposited on the slide, with Aragonite favoured for slower evaporation rates[20]. Aragonite formation is also favored in aqueous environments[58], such as the sedimented precipitate.

The SEM images of Evian precipitate exhibited a significant fraction of Aragonite, but this was after two 25 minute periods of sonication and was extracted by the same method as the Ballygowan samples. This agrees with literature reports of preferential sonochemical precipitation of Aragonite induced by relative to precipitation by heating to 80°C alone. This is reportedly a consequence of high local temperatures and pressures and an increase in nucleation rate statistically favouring Aragonite growth, with multiple crystallites providing a greater surface area to seed growth[58].

## 5.6 Conclusions

The aim of this chapter was to compare the effects of magnetic treatment and ultrasonic treatment of soft and hard water. The magnetic treatments with a simultaneous control, which were carried out using a two-channel peristaltic pump, established that even a single pass through the magnetic field was enough to change the ratio of the solid phases Calcite, Aragonite and Halite in the crystalline residue obtained by heating and evaporating hard water with a high proportion of dissolved $CaCO_3$, The result confirms that transient magnetic treatment does have an effect that lasts for hours on hard water. This is evidence for a non-classical nucleation process where colloidal nanoscale pre-nucleation clusters (DOLLOPS) already present in the solution are influenced by passing through the magnetic field[20].

We found that peristaltic pumping has an effect on the zeta potential, especially of the control water. The zeta-potential of the sonicated of soft water showed evidence for the presence of nanobubbles, which are stable for up to 100 hours, in accordance with previous literature on nanobubble water [25-27,29,48,59,60]. However, sonication of hard water leads to the precipitation of Calcite or Aragonite at much lower temperatures than in the absence of ultrasound.

By analyzing the ionic content (total dissolved solids) and comparing it to the mass of precipitated Calcite, it is possible to estimate how much Ca is bound in DOLLOPS, where it cannot contribute to the conductivity. In this way, we obtain a new estimate of about 30%.

The main conclusion is that both magnetic and ultrasonic treatments of hard water provide evidence for these pre-nucleation clusters. The accuracy of the estimate of the quantity of DOLLOPS present could be improved by using synthetic hard water with only $CaCO_3$ in solution, rather than the natural samples we chose to work with. A $Ca^{2+}$ specific probe to monitor the specific conductance of $Ca^{2+}$ cations only would reduce the uncertainty in correlating TDS changes to calcium carbonate alone. The other area where further investigation is required is to find out how the zeta potential of hard water can be influenced by peristaltic pumping, which is recognized as a very gentle method of creating a circulating

fluid flow. Dynamic light scattering measurements would reveal the size distribution of the nanobubble population, providing insight into the nature of the ζ potential decay, and the effect of hardness on mean bubble size. It may also give more information on the source of the positive ζ potential in sonicated hard mineral waters, and the interactions between the nanobubbles and the nucleation precursors.

# Bibliography

[1] A. Alabi, M. Chiesa, C. Garlisi, and G. Palmisano, Environmental Science: Water Research and Technology **1**, 408 (2015).

[2] C. T. Rodgers, Pure and Applied Chemistry **81**, 19 (2009).

[3] O. Zúñiga, J. A. Benavides, D. I. Ospina-Salazar, C. O. Jiménez, and M. A. Gutiérrez, Ingeniería y competitividad **18**, 217 (2016).

[4] R. Eliassen, R. T. Skrinde, and W. B. Davis, Journal (American Water Works Association) **50**, 1371 (1958).

[5] K. Higashitani, A. Kage, S. Katamura, K. Imai, and S. Hatade, Journal of Colloid and Interface Science **156**, 90 (1993).

[6] M. Iwasaka and S. Ueno, Journal of Applied Physics **83**, 6459 (1998).

[7] J. Nakagawa, N. Hirota, K. Kitazawa, and M. Shoda, Journal of Applied Physics **86**, 2923 (1999).

[8] I. Otsuka and S. Ozeki, The Journal of Physical Chemistry B **110**, 1509 (2006).

[9] T. I. Quickenden, D. M. Betts, B. Cole, and M. Noble, The Journal of Physical Chemistry **75**, 2830 (1971).

[10] S. Ueno and M. Iwasaka, Journal of Applied Physics **75**, 7177 (1994).

[11] K. X. Zhou, G. W. Lu, Q. C. Zhou, J. H. Song, S. T. Jiang, and H. R. Xia, Journal of Applied Physics **88**, 1802 (2000).

[12] F. Alimi, M. Tlili, M. Ben Amor, G. Maurin, and C. Gabrielli, Surface Engineering and Applied Electrochemistry **45**, 56 (2009).

[13] J. M. D. Coey, Philosophical Magazine **92**, 3857 (2012).

[14] Y. Wang, H. Wei, and Z. Li, Results in Physics **8**, 262 (2018).

[15] R. Cai, H. Yang, J. He, and W. Zhu, Journal of Molecular Structure **938**, 15 (2009).

[16] S. A. Ghauri and M. S. Ansari, Journal of Applied Physics **100**, 066101 (2006).

[17] F. C. Meldrum and R. P. Sear, Science **322**, 1802 (2008).

[18] D. Gebauer, A. Völkel, and H. Cölfen, Science **322**, 1819 (2008).

[19] R. Demichelis, P. Raiteri, J. D. Gale, D. Quigley, and D. Gebauer, Nature Communications **2**, 590 (2011).

[20] J. M. D. Coey and S. Cass, Journal of Magnetism and Magnetic Materials **209**, 71 (2000).

[21] G. J. Price, M. F. Mahon, J. Shannon, and C. Cooper, Crystal Growth & Design **11**, 39 (2011).

[22] L. Wang, I. Sondi, and E. Matijević, Journal of Colloid and Interface Science **218**, 545 (1999).

[23] K. Yasuda, H. Matsushima, and Y. Asakura, Chemical Engineering Science **195**, 455 (2019).

[24] K. Ebina, K. Shi, M. Hirao, J. Hashimoto, Y. Kawato, S. Kaneshiro, T. Morimoto, K. Koizumi, and H. Yoshikawa, PLOS ONE **8**, e65339 (2013).

[25] S. H. Oh and J.-M. Kim, Langmuir **33**, 3818 (2017).

[26] J. Jin, Z. Feng, F. Yang, and N. Gu, Langmuir **35**, 4238 (2019).

[27] K. Yasuda, H. Matsushima, and Y. Asankura, Chemical Engineering Science **195**, 455 (2019).

[28] N. Nirmalkar, A. W. Pacek, and M. Barigou, Langmuir **34**, 10964 (2018).

[29] E. D. Michailidi, G. Bomis, A. Varoutoglou, G. Z. Kyzas, G. Mitrikas, A. C. Mitropoulos, E. K. Efthimiadou, and E. P. Favvas, J Colloid Interface Sci **564**, 371 (2020).

[30] H. Ren, S. R. German, M. A. Edwards, Q. Chen, and H. S. White, The Journal of Physical Chemistry Letters **8**, 2450 (2017).

[31] J. Jin, R. Wang, J. Tang, L. Yang, Z. Feng, C. Xu, F. Yang, and N. Gu, Colloids and Surfaces A: Physicochemical and Engineering Aspects **589**, 124430 (2020).

[32] N. Nirmalkar, A. W. Pacek, and M. Barigou, Langmuir **35**, 2188 (2019).

[33] K. Hideaki, M. Shigeo, K. Masakazu, and F. Toshihiro, in *Proc.SPIE*2014).

[34] T. Uchida, S. Liu, M. Enari, S. Oshita, K. Yamazaki, and K. Gohara, Nanomaterials **6** (2016).

[35] T. Uchida, H. Nishikawa, N. Sakurai, M. Asano, and N. Noda, Nanomaterials (Basel) **8**, 152 (2018).

[36] K. Yasui, T. Tuziuti, and W. Kanematsu, Ultrason Sonochem **48**, 259 (2018).

[37] R. Prasad and S. V. Dalvi, Chemical Engineering Science **226**, 115911 (2020).

[38] Ö. Johansson, T. Pamidi, M. Khoshkhoo, and Å. Sandström, *Sustainable and energy efficient leaching of tungsten (W) by ultrasound controlled cavitation* 2017).

[39] M. R. Ghaani, P. G. Kusalik, and N. J. English, Science Advances **6**, eaaz0094 (2020).

[40] J. R. T. Seddon, D. Lohse, W. A. Ducker, and V. S. J. Craig, ChemPhysChem **13**, 2179 (2012).

[41] M. Alheshibri, J. Qian, M. Jehannin, and V. S. J. Craig, Langmuir **32**, 11086 (2016).

[42] P. S. Epstein and M. S. Plesset, The Journal of Chemical Physics **18**, 1505 (1950).

[43] S. Ljunggren and J. C. Eriksson, Colloids and Surfaces A: Physicochemical and Engineering Aspects, 151 (1997).

[44] S. Samimi, N. Maghsoudnia, R. B. Eftekhari, and F. Dorkoosh, in *Characterization and Biology of Nanomaterials for Drug Delivery*, edited by S. S. Mohapatra *et al.* (Elsevier, 2019), pp. 47.

[45] O. w. b. Larryisgood, Diagram of zeta potential and slipping planeV2 (2012).

[46] B. V. Boshenyatov, S. I. Kosharidze, and Y. K. Levin, Russian Physics Journal **61**, 1914 (2019).

[47] J. M. D. Coey, M. Möbius, A. J. Gillen, and S. Sen, Electrochemistry Communications **76**, 38 (2017).

[48] S. A. Hewage, J. Kewalramani, and J. N. Meegoda, Colloids and Surfaces A: Physicochemical and Engineering Aspects **609**, 125669 (2021).

[49] Q. Wang, H. Zhao, N. Qi, Y. Qin, X. Zhang, and Y. Li, Scientific Reports **9**, 1118 (2019).

[50] K. Yasui, T. Tuziuti, W. Kanematsu, and K. Kato, Langmuir **32**, 11101 (2016).

[51] A. Khaled Abdella Ahmed, C. Sun, L. Hua, Z. Zhang, Y. Zhang, T. Marhaba, and W. Zhang, Environmental Engineering Science **35**, 720 (2017).

[52] A. Flanagan, Report of the Public Analyst's Laboratory. Chemical Analysis of Hillbrook and CRANN Tap Water., Feb. 2020.

[53] Volvic Natural Spring Water: Annual Quality Report., URL: http:// volvic- na. com/ Volvic.pdf.

[54] Evian Natural Spring Water: Annual Quality Report, URL: <https://www.evian.com/en_us/wp-content/themes/evian/> assets/report_files/evian_Bottle_Water_Quality_Report_2020. pdf.

[55] https://www.ballygowan.ie/our-water-story/ (Accessed 08/12 2021).

[56] Website : quality/conductivity-salinity-tds/. Jan. 2019).

[57] F. Y. Ushikubo, T. Furukawa, R. Nakagawa, M. Enari, Y. Makino, Y. Kawagoe, T. Shiina, and S. Oshita, Colloids and Surfaces A: Physicochemical and Engineering Aspects **361**, 31 (2010).

[58] R. M. Santos, P. Ceulemans, and T. Van Gerven, Chemical Engineering Research & Design: Transactions of the Institution of Chemical Engineers Part A **90**, 715 (2012).

[59] V. S. J. Craig, Soft Matter **7**, 40 (2011).

[60] T. Leong, M. Ashokkumar, and S. Kentish, in *Handbook of Ultrasonics and Sonochemistry* (Springer Singapore, Singapore, 2016), pp. 69.

# Chapter 6

# Conclusion and Future Direction

## 6.1 Conclusion

The prospect of using a remote magnetic field to control and manipulate the liquid flow inside a microfluidic channel was the main motivation of this thesis. Exploration of how applying a magnetic field changes the physical properties of a liquid has been the main work in this thesis, and first steps are taken towards fabrication of a smart microfluidic channel that can transport liquid with the help of an external remote magnetic field. Magnetic field effects on water are controversial topics and have interested researchers due to their potential real-life applications. Many of the claims are still disputed or results are inconclusive.

We first studied the most controversial claim, that magnetic field changes on the surface tension of water. The shape of pendant droplets of water and aqueous solutions of paramagnetic ions is studied in uniform and non-uniform magnetic fields produced by configurations of small permanent magnets. The effect on water of a uniform field produced by permanent magnets is small (0.3%) and at the limit of statistical significance, $\Delta\gamma = 0.19 \pm 0.21$ mNm$^{-1}$. The apparent changes in surface tension of water and paramagnetic solutions observed in the presence of a vertical magnetic field gradient are related to a change of the shape of the drop in a non uniform field. Static measurements of the droplet shape are analysed in terms of an apparent surface tension $\gamma_{app}$ or an effective density $\rho_{eff}$. Magnetic field gradients of up to 80 T$^2$m$^{-1}$ lead to changes of effective density that are negative for diamagnetic solutions (buoyancy effect) and positive for paramagnetic solutions. We have eliminated these effects using a zero susceptibility method, where the magnetic body forces are absent, allowing any real magnetic field effect to

be isolated. The measurements on droplets of zero-susceptibility, compensated solutions of $Cu^{2+}$, $Mn^{2+}$ and $Dy^{3+}$ where droplet shape is unaffected by any magnetic body all show a small decrease in surface tension. Values for $DyCl_3$, $MnSO_4$, $CuSO_4$ , are -0.30 $mNm^{-1}$ ,-0.48 $mNm^{-1}$ ,-0.5 $mNm^{-1}$ in a non-uniform vertical field and -0.50 $mNm^{-1}$, -0.51 $mNm^{-1}$, -0.11 $mNm^{-1}$ in a uniform horizontal field field. The droplet profile of strongly-paramagnetic solutions such as 0.1 Dy M $DyCl_3$ show the effect of a non-uniform vertical field gradient. In future, the zero-susceptibility method should be extended to much larger fields, > 5 T,where the effect will be greater, and clearly outside the experimental uncertainly.

Magnetic field effects on increasing the evaporation rate of pure water and solutions of 1 M NaCl and 1.5 – 6 M urea has been investigated systematically for periods of up to 60 hours in a well-controlled experiment, simultaneously in the presence and absence of a 500 mT magnetic field. Although the evaporation rates fluctuate over the course of the runs, we find a systematic 12 ± 2 % enhancement of the evaporation rate of water and a systematic decrease of 23 ± 0.2 % for NaCl and 21 ± 6 % for 6 M urea. A new model proposed to explain results that treats the long-lived para and ortho isomers of water vapour as distinct gasses. The para:ortho ratio in vapour supplied from the liquid surface depends on the isomeric ratio in the liquid, which may differ from that in the ambient atmosphere. The ratio can be modified by a magnetic field. The mechanisms considered are dephasing of the Larmor precession of adjacent protons on a water molecule in small magnetic field gradient, which tends to equalize the populations and reduce the evaporation rate and Lorentz stress on the moving water charge dipole that may increase the proportion of ortho isomer and thereby increase the evaporation rate. The claim of a memory effect in water has been checked in 60 hour runs where no effect was observed, and in 6M urea where the decrease was much less than in the continuous presence of the field.

The experiments on evaporation of water in PMMA microfluidic channels showed greater magnetic field effects relative to the no-magnet control than were seen in the experiments on water in beakers. The PMMA is hydrophobic, and the water meniscus seen across the microfluidic channel is related to pinning at the vertical walls. The strongly-enhanced increase

in evaporation rate in the channel exposed to the 300 mT magnetic field is ~3 time more than what we observed in beakers. The trend of an increase in the evaporation rate of water remained for all the experiments even though the rates of evaporation were different. A proposed mechanism of this increase in evaporation in the microfluidic channel was related to evaporation induced flow of water from the centre to the edge of the meniscus. We do not yet have an explanation of the very large magnetic field enhancemnts sometimes observed, but they may be related to the ortho/para ratios, suggested in chapter 3.

The magnetic treatment of hard and soft water has been studied using a commercial magnetic water conditioner with permanent magnets in a continuous flow driven by a peristaltic pump. The effects of magnetic and ultrasonic treatment of soft and hard water have been studied. The magnetic treatments with a simultaneous control showed evidence that even a single pass through the magnetic field was enough to change the ratio of the solid phases Calcite, Aragonite and Halite in the crystalline residue obtained by heating and evaporating hard water. This shows evidence of a non-classical nucleation process where colloidal nanoscale pre-nucleation clusters (DOLLOPS) already present in the solution are influenced by passing water through the magnetic field. We also found that circulating water through a peristaltic pump generates nanobubbles which were inferred from the zeta potential.

The zeta-potential sonicated of soft water showed evidence for the presence of nanobubbles, which are stable for up to 100 hours. However, sonication of hard water leads to the precipitation of Calcite or Aragonite at much lower temperatures than in the absence of ultrasound. By analyzing the ionic content (total dissolved solids) and comparing it to the precipitate mass, it was possible to estimate how much Ca is bound in DOLLOPS, where it cannot contribute to the conductivity. Both magnetic and ultrasonic treatments of hard water provide evidence for these pre-nucleation clusters.

## 6.2 Future direction

We have carefully analysed the magnetic field effects on the physical properties of liquids. The final aim of the project was to fabricate a magneto-responsive structures that can directionally transport liquid in a microfluidic channel. This part of the work was limited by restricted laboratory access during COVID 19 pandemic. A preliminary study of the fabrication of magnetic particle loaded polymer structures were made by a 2-step replica moulding method. The magneto responsive pillars (cilia) are made by the photopolymerization of a magnetite particle loaded monomer cocktail.

The experimental details and preliminary results are given in §6.2

### 6.2.1 Experimental methods

The aim is to make bendable magneto-responsive structures using replica moulding from photopolymerized structures. The polymer microrodes are to be loaded with magnetic particles, such as high coercivity $Sm_2Fe_{17}N_x$ (particle size of 10 μm) and the movement is controlled using permanent magnets. The liquid droplet motion on these bendable magnetic structures will be analyzed using the Dataphysics OCA 25 analyser.

The experimental step consists of fabrication of the desired structures using 3D printing. The printed structures were used as a mould for the two-step replication of microstructures. In the first step, the printed microstructures are transferred to PDMS by replica moulding. The surface energy of the replicating materials needs to be suitably matched to allow for easy removal.

Replica moulding for the fabrication of photopolymerized structures can be very difficult for two reasons: 1) the structures need to be adhere sufficiently to the substrate 2) photocurable polymers, particularly acrylates, can have a detrimental effect of the curability of PDMS. The selection of appropriate substrates for the photopolymerization is crucial during replica moulding. The work plan includes appropriate selection of substrates for photopolymerization

and fabrication of magneto responsive smart structures for remote non-contact directed liquid transport of liquids.

The printed microstructure pillars were transferred to a PDMS matrix. Before pouring the PDMS monomer and curing agent, it is necessary to make sure that the surface energies of mould and PDMS match and any mismatch would pose a problem during peeling. Hence, the following stages were followed before pouring the PDMS monomer.

1. **Clean the mould** - Printed mould is soaked in ethanol for 2 days to remove the remanent acrylates

2. **Silanize the mould** - Mould is kept inside a desiccator along with a 100 μL of Trichloro perfluorooctyl silane on a glass slide and left for 3 hours until all the silane is evaporated from the glass slide

3. Place the silanized hole mould inside the desiccator under vacuum for 10-15 minutes

4. Poure PDMS (10:1) above the structures and keep inside the desiccator under vacuum for 3 hours.

5. Place on hotplate at 100 ° C for 30 minutes

Polymerized PDMS holes peeled out of the mould and the silanized mould can be reused for future experiments.

Making a stable suspension of the magnetic particles in a monomer cocktail is extremely important during the photopolymerization step. A stable suspension of magnetic monomer cocktails have been produced with 7.6 wt.% micron-sized particles of $Fe_3O_4$. The monomer cocktail contains polyethylene glycol diacrylate and a water-soluble photo initiator. The monomer cocktails were synthesized in Prof. Larisa Florea and Dr. Colm Delaney's laboratory in the School of Chemistry, Trinity College Dublin

The magnetic particle loaded polymer cocktail is sonicated for five minutes to redisperse the sedimented particles and poured over the PDMS holes. PDMS holes were kept in vacuum for 15 minutes to remove air trapped in the micron sized holes. After filling the holes with the suspension, it is placed under an intense light for the photopolymerization.

### 6.2.1 First Results and Conclusion

A printed mould with micropillars of diameter 100 microns and height 500 microns has been used for replica-moulding in PDMS as shown in Fig.6.3. The substrate is 20 ×25 cm, and the pillars are 500 μm apart. A preliminary fabrication of magnetite particle loaded structures are shown in Fig.6.3 b)

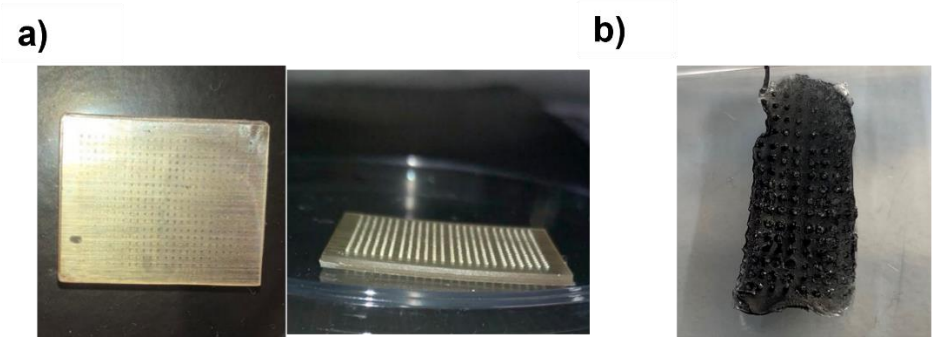


Figure 6. 1: a) images of 2D printed micropillars b) Image of the fabricated magnetite loaded pillars

The photopolymerization of the magnetic particle loaded polymer pillars was not perfect as it did not polymerize the suspension completely. The next step of the experiments includes the UV polymerization of the magnetic loaded particles, which is another method of polymerization.

A mould with micropillars was printed and transferred to a PDMS matrix to make a negative mould. A magnetite-loaded photosensitive monomer cocktail was poured above the PDMS holes but the pillars were not completely polymerized during the curing process. Hence, the UV curing method has to be tested to check if curing is complete. The shape and size of the microstructures needs to optimized. After improving the method of fabrication and the shape of the microstructures, different hard and soft magnetic materials have to be mixed with the monomer cocktails to maximize the magnetic field response. There is a compromise between the concentration of opaque or optically-reflecting magnetic particles and the ability to use photosensitive monomers.

In future, UV polymerization of the monomer cocktail loaded with the magnetic particles should be improved. After finding a suitable method of curing, the shape and size of the cilia will have to be optimized for maximum magnetic field response. The loading process of high coercivity $Sm_2Fe_{17}N_x$ powder also has to be optimized.

# Appendix A

Table 4 : Values of relative humidity, temperature and net evaporation rate of water with and without magnetic field

| Run number | Time (hr) | Evaporation rate ($kgm^{-2}h^{-1}$) B = 500 mT | Evaporation rate ($kgm^{-2}h^{-1}$) B = 0 mT | Ratio | Relative Humidity (%) | Temperature (°C) |
|---|---|---|---|---|---|---|
| 1 | 16 | 0.0258 | 0.0212 | 1.216 | 72.4 | 21.7 |
| 2 | 16 | 0.0318 | 0.0307 | 1.035 | 78.0 | 22.4 |
| 3 | 16 | 0.0237 | 0.0226 | 1.047 | 78.6 | 22.1 |
| 4 | 16 | 0.0321 | 0.0290 | 1.108 | 78.4 | 22.5 |
| 5 | 16 | 0.0321 | 0.0307 | 1.047 | 74.6 | 22.8 |
| 6 | 16 | 0.0339 | 0.0286 | 1.185 | 63.6 | 21.3 |
| 7 | 16 | 0.0300 | 0.0272 | 1.104 | 63.9 | 21.0 |
| 8 | 16 | 0.0388 | 0.0353 | 1.100 | 69.6 | 20.8 |
| | | | | | | |
| 9 | 16 | 0.0254 | 0.0194 | 1.309 | 65.8 | 20.4 |
| 10 | 16 | 0.0540 | 0.0452 | 1.195 | 66.0 | 19.9 |
| | | | | | | |
| 11 | 16 | 0.0335 | 0.0321 | 1.044 | 68.4 | 21.5 |
| 12 | 16 | 0.0353 | 0.0325 | 1.087 | 67.3 | 21.2 |
| 13 | 16 | 0.0410 | 0.0378 | 1.084 | 71.1 | 23.1 |
| 14 | 16 | 0.0247 | 0.0219 | 1.129 | 77.1 | 22.2 |
| 15 | 16 | 0.0212 | 0.0191 | 1.111 | 80.7 | 22.4 |
| 16 | 16 | 0.0240 | 0.0230 | 1.046 | 81.0 | 22.9 |
| 17 | 16 | 0.0272 | 0.0247 | 1.100 | 78.1 | 22.4 |
| | | | | | | |
| 18 | 16 | 0.0222 | 0.0194 | 1.145 | 77.1 | 22.3 |
| 19 | 16 | 0.0247 | 0.0240 | 1.029 | 71.1 | 21.8 |
| 20 | 16 | 0.0293 | 0.0265 | 1.107 | 74.8 | 23.3 |
| 21 | 16 | 0.0240 | 0.0205 | 1.172 | 78.8 | 22.6 |
| 22 | 16 | 0.0222 | 0.0208 | 1.068 | 76.4 | 22.6 |
| 23 | 16 | 0.0318 | 0.0233 | 1.364 | 76.4 | 22.5 |

| | | | | | | |
|---|---|---|---|---|---|---|
| 24 | 60 | 0.0299 | 0.0285 | 1.050 | 76.0 | 22.5 |
| 25 | 60 | 0.0453 | 0.0394 | 1.151 | 56.0 | 22.4 |
| 26 | 60 | 0.0247 | 0.0217 | 1.139 | 76.0 | 22.6 |
| 27 | 60 | 0.0331 | 0.0294 | 1.125 | 66.9 | 21.4 |
| 28 | 60 | 0.0261 | 0.0238 | 1.095 | 75.7 | 23.2 |
| | | | | | | |
| 29 | 16 | 0.0543 | 0.0512 | 1.061 | 61.8 | 22.9 |
| 30 | 16 | 0.0483 | 0.0459 | 1.052 | 70.9 | 21.2 |
| 31 | 16 | 0.0391 | 0.0377 | 1.037 | 67.0 | 21.4 |
| 32 | 16 | 0.0370 | 0.0338 | 1.095 | 78.1 | 22.9 |
| | | | | | | |
| 33 | 16 | 0.0406 | 0.0349 | 1.163 | 75.3 | 23.1 |
| 34 | 16 | 0.0451 | 0.0402 | 1.122 | 70.7 | 23.8 |
| 35 | 16 | 0.0353 | 0.0296 | 1.193 | 79.3 | 23.5 |
| 36 | 16 | 0.0427 | 0.0377 | 1.133 | 78.3 | 25.6 |
| | | | | | | |
| **Average** | | 0.0331 | 0.0297 | 1.118 | 72.8 | 22.3 |
| **Standard deviation** | | 0.0088 | 0.0081 | 0.074 | 6.01 | 1.04 |

Table 5 : Values of relative humidity, temperature and net evaporation rate of 6M urea solution with and without magnetic field

| Run number | Time (hr) | Evaporation rate ($kgm^{-2}h^{-1}$) B = 500 mT | Evaporation rate ($kgm^{-2}h^{-1}$) B = 0 mT | Ratio | Relative Humidity (%) | Temperature (°C) |
|---|---|---|---|---|---|---|
| 1 | 16 | 0.0314 | 0.0399 | 0.788 | 50.5 | 22.8 |
| 2 | 16 | 0.0307 | 0.0427 | 0.719 | 46.3 | 21.7 |
| 3 | 16 | 0.0392 | 0.0452 | 0.867 | 48.0 | 21.6 |
| 4 | 16 | 0.0307 | 0.0410 | 0.750 | 51.0 | 21.7 |
| | | | | | | |
| **Average** | | 0.0330 | 0.0422 | 0.781 | 49.0 | 22.0 |
| **Standard deviation** | | 0.0041 | 0.0023 | 0.064 | 2.2 | 0.6 |

Table 6 : Values of relative humidity, temperature and net initial and steady evaporation rates of water and 6M urea solution

| Run | Time (hr) | Liquid | Intial evaporation rate ($kgm^{-2}h^{-1}$) | Steady evaporation rate ($kgm^{-2}h^{-1}$) | Relative Humidity (%) | Temperature (°C) |
|---|---|---|---|---|---|---|
| 1 | 1 | water | 0.185 | 0.0621 | 54.5 | 25.0 |
| 2 | 1 | Water | 0.167 | 0.0876 | 54.5 | 25.0 |
| 3 | 1 | Water | 0.154 | 0.0734 | 55.0 | 25.0 |
| 4 | 1 | Water | 0.131 | 0.0702 | 55.0 | 25.0 |
| 5 | 1 | Water | 0.119 | 0.0720 | 57.5 | 24.5 |
| 6 | 1 | Water | 0.104 | 0.0705 | 57.5 | 24.5 |
| 7 | 1 | Water | 0.107 | 0.0620 | 62.0 | 24.5 |
| 8 | 1 | Water | 0.107 | 0.0523 | 62.0 | 24.5 |
| | | | | | | |
| 9 | 2 | water | 0.136 | 0.0452 | 60.0 | 24 |
| | | | | | | |
| **Average** | | | 0.134 | 0.0662 | 57.6 | 24.7 |
| **Standard deviation** | | | | | 3.1 | 0.4 |
| | | | | | | |
| 10 | 1 | 6M Urea | 0.0107 | 0.0427 | 73.0 | 24.2 |
| 11 | 1 | 6M Urea | 0.0141 | 0.0270 | 73.0 | 24.2 |
| 12 | 1 | 6M Urea | 0.0062 | 0.0257 | 68.5 | 23.5 |
| 13 | 1 | 6M Urea | 0.0085 | 0.0242 | 68.5 | 23.5 |
| | | | | | | |
| 14 | 2 | 6M Urea | 0.0166 | 0.0310 | 60.0 | 24.0 |
| | | | | | | |
| **Average** | | | 0.011 | 0.0301 | 68.6 | 23.9 |
| **Standard deviation** | | | 0.004 | 0.0070 | 5.3 | 0.4 |

# Appendix B

The charged particles move under the action of the electric field force, and at the same time, the liquid viscous force acting on the particles prevents the particles from moving; the counter ions in the electric double layer on the surface of the particles move in the opposite direction of the electric field force, resulting in an electrophoretic retardation force; The center of the ion atmosphere lags behind the center of the particle, and the resulting relaxation effect further prevents the movement of the particle . When these 4 forces are in equilibrium, the particles move at a constant speed in the liquid. However, the influence of electrophoretic retardation force and relaxation effect on the thickness of the electric double layer is difficult to accurately determine, which also leads to the inability to determine the Henry function accurately.

Henry [5] gave the piecewise expression of Henry's function according to the condition that the particle deforms the electric field

$$f(ka) = 1 + \frac{(ka)^2}{16} - \frac{5(ka)^3}{48} - \frac{(ka)^4}{96} + \frac{(ka)^5}{96} - \left(\frac{(ka)^4}{8} - \frac{(ka)^6}{96}\right) \exp(ka)En(ka),\ ka<1$$

$$En(ka) = (ka)^{n-1} \int_{ka}^{\infty} \frac{\exp(-t)}{t^n}\, dt = a^{n-1} \int_{a}^{\infty} \frac{\exp(-ka)}{a^n}\, da$$

When $ka \to 0$, $f(ka) = 1$, that is, the Hückel approximation, at this time $\mu = 2\varepsilon_r\varepsilon_0\zeta/3\eta$.

$$f(ka) = \frac{3}{2} - \frac{9}{2\,ka} + \frac{75}{2} - \frac{330}{2\,ka^2} + \cdots \quad ka>1$$

when $ka \to \infty$ Time, f(ka)=1.5, that is, the Smoluchowski approximation, at this time $\mu=\varepsilon_r\varepsilon_0\zeta/\eta$.

In general, the measured particle $ka \gg 1$, so the Smoluchowski approximation is usually used; when the particle radius and concentration are very small, it will appear $ka \ll 1$, so the Hückel approximation is less used, but it is suitable for the measurement of particle Zeta potential in non-polar solution.